The interplay between magnetism and electronic structure in topological materials

Qianni Jiang

A dissertation
submitted in partial fulfillment of the
requirements for the degree of

Doctor of Philosophy

University of Washington

2023

Reading Committee:

Jiun-Haw Chu, Chair

Xiaodong Xu

Mark Rudner

Program Authorized to Offer Degree:
Physics

University of Washington

Abstract

The interplay between magnetism and electronic structure in topological materials

Qianni Jiang

Chair of the Supervisory Committee:
Jiun-Haw Chu
Department of Physics

Over the past 40 years, topological materials have emerged as a fascinating new class of phases of matter, characterized by their robust fundamental properties that remain invariant under smooth changes of material parameters, capturing widespread interest and driving extensive research in the field. The more recent realization of magnetic topological materials has unlocked new research directions, as these materials display a remarkable interplay between magnetic order and topological electronic properties. This connection leads to various exotic phenomena and emergent quantum states, such as the quantum anomalous Hall effect, axion insulators, and magnetic Weyl semimetals. Moreover, these materials provide opportunities to study topological phase transitions with easily tunable magnetic fields, facilitating a deeper understanding of the underlying physics and paving the way for the exploration of novel phenomena rooted in unique topological properties.

In the intrinsic antiferromagnetic topological insulator $MnBi_2Te_4$, various topological phases across different dimensions and types of magnetism provide a unique platform for studying the interplay between band topology and magnetic order. The ground state of bulk $MnBi_2Te_4$ is an antiferromagnetic topological insulator protected by the combined half-layer lattice translation and time-reversal symmetry ($S = \tau_{1/2}\mathcal{T}$). In the thin film limit, both quantum anomalous Hall insulator states and axion insulator states have been reported in odd and even septuple layers, respectively. In the bulk field-induced ferromagnetic state, $MnBi_2Te_4$ has been predicted to be an ideal type-II Weyl semimetal with a single pair of

Weyl nodes. Moreover, due to the intertwined electronic structures and magnetic orders, it is possible to tune the type-II Weyl semimetal to a type-I Weyl semimetal across a Lifshitz transition by altering the magnetic field angle. Furthermore, the highly tunable properties of $MnBi_{2-x}Sb_xTe_4$ make it an adaptable platform for investigating other topological phases through Lifshitz transitions under external fields such as strain and pressure.

In this thesis, I investigate the electronic structures and their interplay with magnetism in the magnetic topological material $MnBi_{2-x}Sb_xTe_4$, identifying distinct Lifshitz transitions. We first use quantum oscillations as a probe to study the electronic structure of $MnBi_{2-x}Sb_xTe_4$ in the field-induced ferromagnetic state, where Sb substitution effectively tunes the chemical potential. We then identify the field-induced ferromagnetic $MnBi_{2-x}Sb_xTe_4$ as an ideal type-II Weyl semimetal with a single pair of Weyl nodes near the Fermi energy. By employing a combination of quantum oscillations and high-field Hall measurements, we demonstrate that the evolution of Fermi surfaces can only be explained by the band structure of an ideal type-II Weyl semimetal. Additionally, We observe a strong dependence of the anomalous Hall conductivity on doping near the charge neutrality point, displaying a singular, heartbeat-like behavior as the Fermi level is tuned across the Weyl nodes. This unique behavior is in agreement with the theoretical predictions for a type-II WSM. Furthermore, we utilize the external magnetic field angle as a tuning knob and observe evidence of an in-situ controlled Lifshitz transition from a type-II Weyl semimetal to a type-I Weyl semimetal as the magnetic field angle rotates from the crystal c-axis to the a-b plane. Finally, we investigate the effect of hydrostatic pressure on the electronic structures and magnetic properties of FM-z $MnBi_{2-x}Sb_xTe_4$, revealing extreme sensitivity and possible creation of a new pair of Weyl nodes in response to external pressure.

Our work deepens the understanding of Weyl semimetals through a comprehensive study of an ideal Weyl semimetal, highlighting $MnBi_{2-x}Sb_xTe_4$ as an exceptional platform for further investigations into Weyl physics. Additionally, our findings pave the way for future research on magnetic topological materials and external-field-controlled Lifshitz transitions, foreshadowing exciting developments in the field of topological materials.

TABLE OF CONTENTS

LIST OF FIGURES

ACKNOWLEDGMENTS

My journey to and through the PhD program has been an enjoyable and fulfilling experience, filled with both joys and challenges. The countless hours spent in the Chu lab and national labs hold a special place in my heart as cherished lifelong memories. The obstacles I faced, particularly during the unprecedented challenges posed by the pandemic, have contributed to my personal growth and development. I am immensely grateful for the support and guidance I received from numerous individuals who have played a significant role in shaping my scientific and personal journey. Without their help and encouragement, this path would not have been as enriching and rewarding as it has been. To all those who have supported me along the way, I extend my deepest gratitude.

First and foremost, I would like to deeply thank my advisor, Jiun-Haw Chu. He has been a role model of mine, both scientifically and personally. Being jiun-haw's student is probably one of the luckiest things during my PhD. He has provided me with invaluable support during the past six years, both scientifically and otherwise. I deeply admire his attitude toward science, his exceptional taste in physics, and numerous other admirable qualities he possesses. He has guided me into the fascinating world of condensed matter physics, equipping me with essential tools and knowledge for my research journey. As I embark on the next stages of my career, I hope to make the best use of the gifts he has bestowed upon me.

I would also like to express my deep gratitude to the members of my committee, Xiaodong Xu, Daniel Gamelin, Mark Rudner, and Jason Detwiler. Their expertise, guidance, and valuable insights have been instrumental in shaping my research and overall academic experience. Their thoughtful feedback and constructive suggestions have greatly contributed to the quality of my work. I am also thankful to the other professors at Univeristy of Washington, including Prof. Di Xiao, David Cobben, Ting Cao, Kai-mei Fu, Ann Nelson, Matt

Yankowitz, Anton Andreev, and Scott Dunham. Their lectures, discussions, and intellectual contributions have been invaluable in broadening my knowledge and stimulating my scientific curiosity. Throughout my PhD journey, I have been closely collaborating with the Xu lab. I am deeply grateful to Xiaodong Xu for his continuous encouragement and unwavering support. I have always admired his great passion for research and his profound wisdom. His guidance has been pivotal in shaping my scientific growth and inspiring me to pursue excellence.

I would also like to express my heartfelt appreciation to all my dear lab mates, who have been my constant companions throughout the past six years: Josh Mutch, Shua Sanchez, Paul Malinowski, Zhong Lin, Yue Shi, Zhaoyu Liu, Elliott Rosenberg, Jonathan DeStefano, Xuetao Ma, Chaowei Hu, Joss Aryes-Sims, Sarah Edwards, Sanae Tominaga, Tiema Qian, Dan Sokratov, Aaron Wang, Winnie Wang, and Ilham Zaky Wilson. Together, we have formed a friendly, supportive, and enjoyable "Chu Lab" community. I want to extend my special thanks to Paul, Josh, Shua, Zhong, and Yue. I joined the lab in the summer of 2017, less than a year after its establishment. Working with Josh, Shua, and Paul in the early days of the lab is one of my most cherished memories. They provided me with invaluable support and guidance when I first joined. Paul and I spent countless hours together in the lab and at national high magnetic field labs, conducting experiments, discussing data and papers, and sometimes just chatting about life. I always found our conversations to be incredibly insightful, and Paul's intelligence, warmth, and wisdom have left a lasting impression on me. Zhong joined the lab during my second year of graduate school and brought with him an exceptional work ethic. We spent numerous days and nights exploring various types of quantum materials together. I am deeply grateful to him for always walking or riding home with me, even late at night. His dedication and hard work have been truly inspiring. Yue holds a special place as my first female colleague during graduate school. Her thoughtfulness and caring nature have made my experience in graduate school much warmer and more vibrant. I am grateful for the support and friendship she has offered throughout our time together. To all my lab mates, thank you for creating a positive and

collaborative environment. The shared experiences, camaraderie, and scientific discussions we have had have greatly enriched my PhD journey.

I would also like to extend my gratitude to my colleagues at UW who have played a significant role in my academic journey and provided invaluable support and knowledge in the field of physics. I would like to thank Zaiyao Fei, Harold Cai, Minhao He, Tiancheng Song, Bevin Huang, Kyle Hwangbo, Qi Zhang, Jiaqi Cai, Xi Wang, Yingqi Wang, Jiayi Zhu, Yinong Zhang, Dmitry Ovchinnikov, Yuzhou Zhao from Xu lab; Paul Nguyen from Cobden lab; Lihua Wu from Yang lab, and Chong Wang from Di's group. Working with these colleagues has been a great privilege and a source of inspiration. Their willingness to help and collaborate has fostered a nurturing and cooperative environment within the condensed matter physics community at UW. I have gained invaluable insights and knowledge through our discussions, experiments, and shared experiences. I am grateful for their contributions, both intellectually and as supportive friends.

My greatest gratitude will also be dedicated to my collaborators: Johanna Palmstrom, John Singleton, David Graf, and Shalinee Chikara at the National High Magnetic Field Labs; Morten Christensen and Professor Rafael Fernandes at the University of Minnesota; Professor Ming Yi at Rice University; and Jiaqiang Yan at Oak Ridge National Lab. Collaborating with these exceptional researchers has been an incredible opportunity and a source of immense learning and growth. I am truly grateful for the chance to work with them and for their valuable contributions to our joint projects. The trips to the NHMFL at Los Alamos and Tallahassee hold a special place in my heart as some of the most precious experiences during my PhD. These visits provided me with the opportunity to access state-of-the-art facilities and collaborate with exceptional research scientists. Working alongside such talented and supportive collaborators has been an absolute pleasure. I am grateful for their guidance, expertise, and friendship throughout our collaborations.

I would also like to thank my dear friends, Qi Zeng, Yi Zhou, Yue Shi, Jiawen Li, and my cat Toffee, for their support and companionship throughout the ups and downs during my PhD journey. Thank you for being pillars of support in my life. I am grateful for the

laughter, the encouragement, and the memories we have shared.

Lastly, I want to convey my deepest gratitude to my parents, whose unwavering support and love have been the foundation of my journey. Despite being physically far apart, they have always been there for me, providing endless encouragement and support. It has been four years since I last saw them due to the pandemic, and I long for the opportunity to reunite and spend precious time together in the future. Their presence and guidance have been instrumental in shaping who I am today, and I am eternally grateful for their unwavering belief in me. I am also incredibly fortunate to have found my partner, Minhao, who has been a constant source of love and positivity in my life. His unwavering support and uplifting presence have been a guiding light, always bringing comfort and joy during challenging times. To my parents and Minhao, thank you for being my pillars of strength. Your love, support, and understanding have been the driving force of mine.

This journey has been nothing short of beautiful, thanks to each and every one of you.

DEDICATION

to my parents

Chapter 1
INTRODUCTION

The chapter offers a comprehensive overview of the two fundamental building blocks of magnetic topological materials: magnetism and topological band theory. To provide a solid understanding of topological band theory, the key concept of Berry phase is introduced, along with distinct topological phases including integer quantum Hall insulators, topological insulators (TI), quantum anomalous Hall insulators, axion insulators, Dirac and Weyl semimetals, and their associated topological properties. The focus then narrows to Weyl semimetals, with a brief introduction to their characteristic features, such as the anomalous Hall effect, chiral anomaly, and Fermi arcs. Finally, the topological phase diagram of $MnBi_2Te_4$ is discussed, providing essential background knowledge about the topological aspect of the material system. This chapter serves as a foundation for subsequent chapters, which delve into the properties and behavior of the intrinsic magnetic topological material $MnBi_{2-x}Sb_xTe_4$ and the interplay between its electronic structure and magnetism in greater detail.

1.1 Overview of magnetism

Magnetism in a solid arises from the behavior of charged particles, particularly electrons, and their interaction with one another through their spin and motion, which creates magnetic fields and gives rise to attractive or repulsive forces between particles. In the presence of periodic potentials in three-dimensional crystalline materials, magnetic moments interact with each other and the environments via various exchange mechanisms. In special cases, long-range magnetic orders, such as ferromagnetic (FM), antiferromagnetic (AFM) and ferrimagnetic ordering, can form.

To understand the ordered magnetic states, we start with the trivial paramagnetic case assuming independent moments with no interaction with each other and the environment

except for the external magnetic field. The partition function is given by:

$$Z = \sum_{m_J=-J}^{J} exp(m_J g_J \mu_B / k_B T) \tag{1.1}$$

where J is the total angular momentum quantum number, g_J is the Lande g factor, and $\mu_B = \frac{e\hbar}{2m_e}$ is the Bohr magneton. The magnetization M can be derived:

$$M = n g_J \mu_B < m_J >= n k_B T \frac{\partial ln Z}{\partial B} \tag{1.2}$$

After summing over the geometric progression in the partition function, we get:

$$M = M_s B_J(y) \tag{1.3}$$

where $M_s = n g_J \mu_B J$ is the saturation magnetization, and $B_J(y)$ is the Brillouin function with $y = g_J \mu_B J B / k_B T$ as a unitless parameter that describes the strength of the external magnetic field compared to the thermal excitations. The Brillouin function as illustrated in Fig. 1.1(d) is given by:

$$B_J(y) = \frac{2J+1}{2J} coth(\frac{2J+1}{2J} y) - \frac{1}{2J} coth(\frac{y}{2J}) \tag{1.4}$$

For $y << 1$, $B_J(y)$ reduces to:

$$B_J(y) = \frac{(J+1)y}{3J} + O(y^3) \tag{1.5}$$

Therefore, under a low magnetic field, the susceptibility of a paramagnetic phase is approximated by:

$$\chi = \frac{M}{H} \approx \frac{\mu_0 M}{B} = \frac{n \mu_0 \mu_{eff}^2}{3 k_B T} \propto \frac{1}{T} \tag{1.6}$$

where $\mu_{eff} = g_J \mu_B \sqrt{J(J+1)}$ and $g_J = \frac{3}{2} + \frac{S(S+1) - L(L+1)}{2J(J+1)}$. This short derivation demonstrates that in the paramagnetic phase, the magnetic susceptibility follows Curie's law $\chi \propto \frac{1}{T}$ (Fig. 1.1(a)). As the external magnetic field increases, the magnetization progressively rises from zero to a state of saturated magnetization, where all magnetic moments align parallel to the applied field.

However, as many materials in nature display, even in the absence of an external magnetic field, spontaneous magnetization can form. This is because in solids, the magnetic

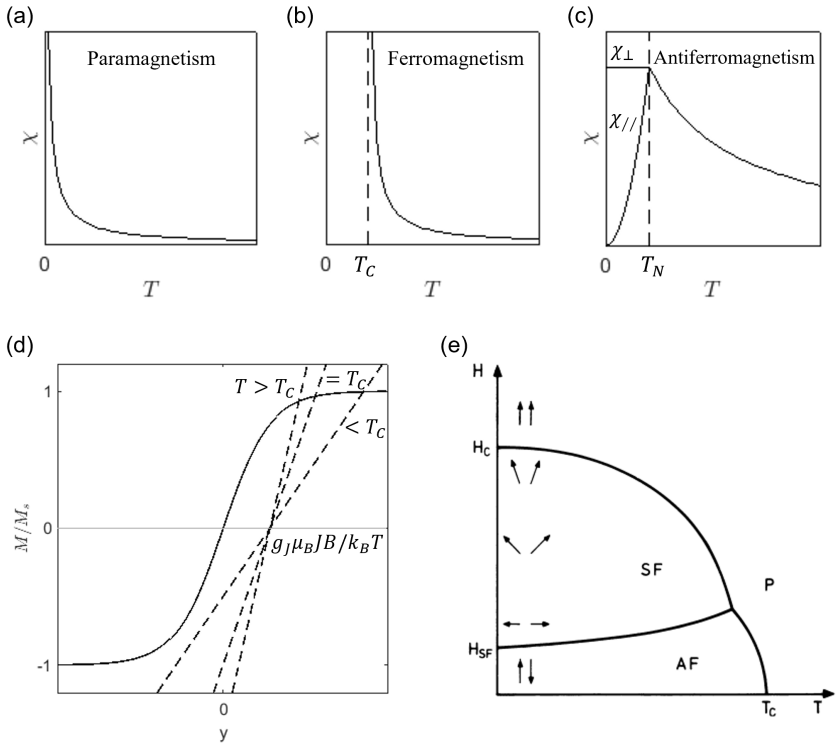

Figure 1.1: **Schematic of magnetic orders** (a)-(c) magnetic susceptibility of (a) paramagnetism, (b) ferromagnetism, (c) antiferromagnetism. (d) Brillouin function and the graphical solution to the Weiss model of a ferromagnet (e) phase diagram of a spin-flop transition. From [1].

moments are not isolated. Instead, they interact with each other and the crystal environment. Various exchange interactions can play a role in determining the magnetic order, such as the direct exchange where the magnetic moments on adjacent magnetic ions directly interact with each other, the superexchange mediated by adjacent non-magnetic ions, RKKY interaction mediated by conduction electrons, and the double exchange where magnetic ions with mixed valencies interact with each other. Regardless of the detailed mechanism, we can use a simple Heisenberg Hamiltonian to generally describe the exchange interactions between neighboring moments:

$$\hat{\mathcal{H}} = -\sum_{ij} J_{ij}\mathbf{S_i}\cdot\mathbf{S_j} + g\mu_B\sum_j \mathbf{S_j}\cdot\mathbf{B} \tag{1.7}$$

where the first term is the Heisenberg exchange energy, and the second term is the Zeeman energy. Noticeably, here we simplify the Hamiltonian by assuming $L = 0$ and $J = S$, where L is the orbital angular momentum quantum number and S is the spin quantum number. This assumption is generally valid for 3d transition metal ions for their orbital moment is mostly quenched. When the exchange constant J_{ij} is positive, spins tend to align in parallel with each other, whereas when J_{ij} is negative, spins align opposite to each other to save energy. We first consider the FM case with $J > 0$.

Based on Eq. 1.7, we can define an effective molecular field on the ith site:

$$\mathbf{B}_{mf} = -\frac{2}{g\mu_B}\sum_j J_{ij}\mathbf{S_j} \tag{1.8}$$

The exchange interaction in the Hamiltonian (Eq. 1.7) can be seen as an effective molecular field $\mathbf{B}_{mf}$ generated by the adjacent spins. Thus, the Hamiltonian can be rewritten as:

$$\hat{\mathcal{H}} = g\mu_B\sum_i \mathbf{S_i}\cdot(\mathbf{B}+\mathbf{B}_{mf}) \tag{1.9}$$

This is identical to the Zeeman energy of the paramagnetic case except for the external magnetic field $\mathbf{B}$ is now replaced by $\mathbf{B}+\mathbf{B}_{mf}$. Assuming $\mathbf{B}_{mf} = \lambda\mathbf{M}$, The magnetization is given by the Brillouin function:

$$\frac{M}{M_s} = B_J(y) \tag{1.10}$$

where

$$y = \frac{g_J\mu_B J(B+\lambda M)}{k_B T} \tag{1.11}$$

Eq. 1.11 can be seen as a linear function of M(y) with an x-axis intercept at $\frac{g_J\mu_B JB}{k_B T}$ and a slope that is dependent on T. Its intersection with the Brillouin function $B_J(y)$ is the solution to the magnetization. As Fig. 1.1(d) illustrates, in the absence of the external field ($B = 0$), the magnetization is zero when $T > T_C$ and finite when $T < T_C$ with T_C equal to:

$$T_C = \frac{g_J\mu_B(J+1)\lambda M_s}{3k_B} = \frac{n\lambda\mu_{eff}^2}{3k_B} \tag{1.12}$$

Furthermore, if one applies a small magnetic field above T_C, the magnetization can be solved by making the small y approximation on the Brillouin function as Eq. 1.5 writes.

$$\frac{M}{M_s} \approx \frac{g_J\mu_B(J+1)}{3k_B}(\frac{B+\lambda M}{T}) \approx \frac{T_C}{\lambda M_s}(\frac{B+\lambda M}{T}) \tag{1.13}$$

The magnetic susceptibility can be then derived as:

$$\chi = \lim_{B \to 0} \frac{\mu_0 M}{B} \propto \frac{1}{T - T_C} \tag{1.14}$$

which is known as the Curie-Weiss law (Fig. 1.1(b)).

When the exchange interaction between magnetic moments is antiferromagnetic ($J < 0$), neighboring magnetic moments tend to align antiparallel to each other, resulting in the formation of two sublattices with ferromagnetically aligned moments. The magnetization M on each sublattice can be calculated using the same method as for the FM case, except for

$$\chi = \lim_{B \to 0} \frac{\mu_0 M}{B} \propto \frac{1}{T + T_N} \tag{1.15}$$

where the T_C is replaced by $-T_N$ in the Curie-Weiss Law (Fig. 1.1(c)). Depending on the different kinds of crystal lattices, there are multiple ways to arrange an equal number of magnetic moments with opposite orientations, which are further categorized as different types of AFM orders.

In certain scenarios, the magnetic moments present on different sublattices within a material may not entirely cancel each other out, resulting in a residual magnetization referred to as ferrimagnetism. This phenomenon arises when the magnetic moments on the sublattices have unequal magnitudes or when they align in opposite directions but possess differing densities. As each sublattice can possess a distinct crystallographic environment, the spontaneous magnetization can significantly vary between sublattices. Consequently, the magnetic susceptibility of a ferrimagnetic state may not conform to the Curie-Weiss law. Instead, the magnetic susceptibility in a ferrimagnetic material can exhibit intricate temperature dependence due to the distinct contributions from the two sublattices to the net magnetization.

So far, we have assumed that the solids are isotropic, meaning that the energy required to align the spins in the x-direction is equivalent to aligning them in the y- or z-direction. However, in real materials, this isotropy is often absent. Consequently, an additional term for single ion anisotropy can be introduced to account for the preference of the magnetic moments to align along specific crystalline directions due to the influence of the crystal field.

$$\hat{\mathcal{H}}_{SI} = -D\sum_{i} S_{i,z}^{2} \tag{1.16}$$

This anisotropy term represents the energy difference associated with deviations from the preferred alignment direction and contributes to the overall magnetic behavior of the material. The system lowers its energy by aligning its moments along the z-axis.

A special case can happen for a weak anisotropic antiferromagnet ($D < z|J|$). By applying an external magnetic field along the easy axis, the system undergoes a spin-flop transition as Fig. 1.1(e) illustrates. Taking the layered antiferromagnet $MnBi_2Te_4$ as an example, we can represent its model Hamiltonian as follows:

$$\hat{\mathcal{H}} = -\sum_{<ij>||} J_{ij}\mathbf{S_i}\cdot\mathbf{S_j} - J_c\sum_{<ij>\perp}\mathbf{S_i}\cdot\mathbf{S_j} - D\sum_{i} S_{i,z}^{2} + g\mu_B\sum_{j}\mathbf{S_j}\cdot\mathbf{B} \tag{1.17}$$

where J_{ij} represents the intralayer exchange coupling, J_c represents the interlayer exchange coupling, and D is the single-ion anisotropy. In bulk $MnBi_2Te_4$, the intralayer coupling is ferromagnetic ($J_{ij} > 0$), and the interlayer coupling is antiferromagnetic ($J_c < 0$). As an external magnetic field is applied along the c-axis, the system undergoes an AFM to canted AFM transition at the spin-flop field H_{c1}, followed by a canted AFM to FM transition at the saturation field H_{c2}. At the spin-flop field H_{c1}, the energy of the AFM state under the external field and the energy of the canted AFM state should be equal. This gives the spin flop transition as a function of the interlayer exchange coupling J_c and the single ion anisotropic term D:

$$g\mu_B H_{c1} = 2SD\sqrt{z|J_c|/D - 1} \tag{1.18}$$

where $g \approx 2$, $S \approx 5/2$ and the number of nearest neighbors z is equal to 6. Similarly, the saturation field H_{c2} is given by:

$$g\mu_B H_{c2} = 2SD(z|J_c|/D - 1) \tag{1.19}$$

In the case of strong anisotropy ($D > z|J|$), the magnetic moments within the material will undergo a direct flipping process to align with the external magnetic field, leading to a spin-flip transition.

1.2 Overview of topological band theory

Conventional band theory has been highly successful in describing the electronic properties of a wide range of solids. This theory is based on the translational symmetry of the crystal, which allows electronic states to be classified in terms of their crystal momentum k within a periodic Brillouin zone. The Bloch states, which are eigenstates of the Bloch Hamiltonian and are defined within a single unit cell of the crystal, give rise to energy bands that collectively form the band structure of a material. These energy bands play a crucial role in determining various electronic and optical properties of solids, such as electrical conductivity, optical absorption, and magnetic behavior.

Despite its many successes, conventional band theory has limitations in describing certain exotic materials with nontrivial topological properties or strong electron-electron interactions, which require more advanced theoretical frameworks. In recent years, the study of topological materials has emerged as a new and exciting field in condensed matter physics. Numerous topological materials have been discovered to date, such as topological insulators (TI), topological superconductors, Dirac and Weyl semimetals, and nodal line semimetals [6, 10, 19]. These materials display exceptional properties that extend beyond the scope of conventional band theory, such as robust surface states with spin-momentum locking in TIs and the emergence of exotic quasiparticles in topological semimetals. To capture the topological properties of these materials, theoretical frameworks such as topological band theory and topological field theory have been developed, broadening our understanding of these extraordinary materials [20, 21].

1.2.1 Berry Phase

The concept of topology originally comes from mathematics, where it refers to the study of geometric properties that are preserved under continuous deformations. In the context of condensed matter physics, topology has been used to describe the global features of the electronic bands, which remain invariant under continuous deformations.

The key concept of the topology band theory is the Berry phase [20]. The Berry phase

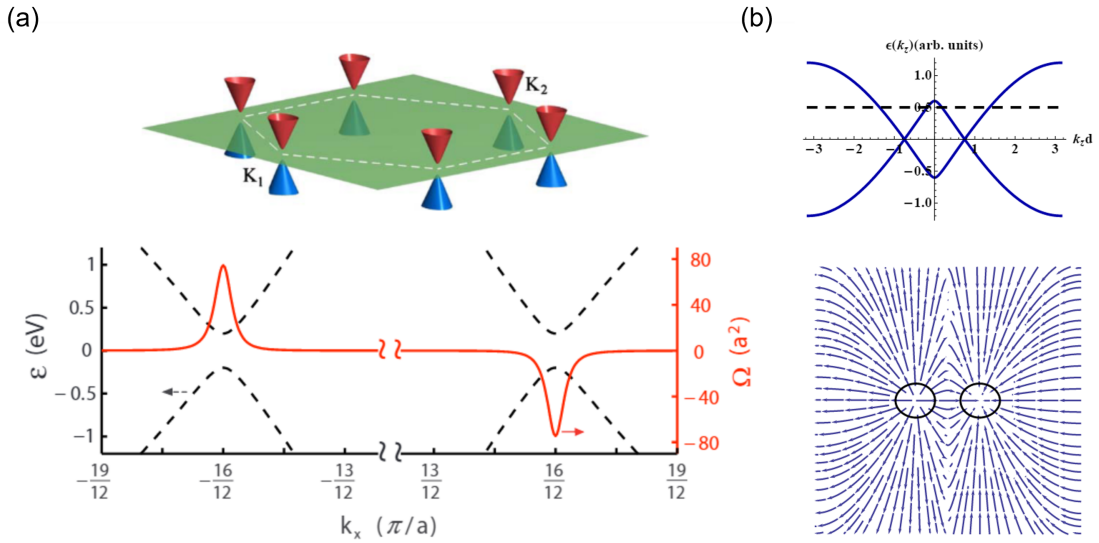

Figure 1.2: **Berry Curvature in topological materials** (a) Energy bands (top panel) and Berry curvature of the conduction band (bottom panel) of a graphene sheet with broken inversion symmetry. (b) Energy bands along the k_z direction of a type-I Weyl semimetal (top panel). Field lines of the Berry curvature in the $k_y = 0$ plane generated by the pair of Weyl nodes (bottom panel). The two contours denote the corresponding Fermi surfaces, enclosing the Weyl nodes. From [2, 3].

is a geometric phase, in contrast to the time-dependent dynamical phase [22]. In solid-state systems, it is acquired by the Bloch wavefunctions as they undergo a cyclic adiabatic evolution in the parameter space of the system's Hamiltonian, typically the crystal momentum k space.

$$\gamma_n = \oint_C d\mathbf{k} \cdot \langle u_n(\mathbf{k}) | \, i\nabla \, | u_n(\mathbf{k}) \rangle \tag{1.20}$$

where the integrand $\langle u_n(\mathbf{k}) | \, i\nabla \, | u_n(\mathbf{k}) \rangle$ is called the Berry connection A_n or Berry vector potential. The Berry connection is gauge-dependent, similar to the vector potential $\mathbf{A}$. In analogy to electrodynamics $\mathbf{B} = \nabla \times \mathbf{A}$, in 3-dimensional k-space a gauge-independent field can be derived:

$$\mathbf{\Omega_n} = \nabla \times \mathbf{A}_n \tag{1.21}$$

where $\mathbf{\Omega_n}$ is the Berry curvature.

In analogy to the magnetic flux density B, Berry curvature is a pseudovector, therefore has a non-vanishing value only when the inversion symmetry or time-reversal symmetry is broken. In materials that break either time-reversal symmetry or inversion symmetry, the Berry curvature is typically negligible in most regions of the momentum space but exhibits sharp and pronounced peaks in areas where Fermi lines intersect or form avoided crossings. Fig. 1.2(a) illustrates the energy band and Berry curvature of a single-layered graphene sheet with a staggered sublattice potential that breaks inversion symmetry [2]. The Berry curvature is enhanced near the massive Dirac points with opposite signs at the K_1 and K_2 valleys due to the presence of time-reversal symmetry. Fig. 1.2(b) showcases the energy band and the field lines of Berry curvature in an ideal type-I Weyl semimetal with either time-reversal symmetry or inversion symmetry breaking [3]. The Weyl nodes, represented by the crossing points of the energy bands in the top panel of Fig. 1.2(b), generate a Berry curvature field that mimics the magnetic flux density B generated by magnetic monopoles.

The Berry curvature plays a significant role in understanding the topological properties of electronic band structures in materials. For instance, the Berry curvature can be used to calculate topological invariants, such as the Chern number n, which characterizes the topological nature of electronic bands.

$$n = \frac{1}{2\pi} \int d^2\mathbf{k}\ \mathbf{\Omega_n} \tag{1.22}$$

Berry curvature is also instrumental in understanding topological properties, such as the intrinsic anomalous Hall effect.

$$\sigma_{ij}^{AH-int} = -\epsilon_{ijl} \frac{e^2}{h} \sum_n \int \frac{d\mathbf{k}}{(2\pi)^d} f(\epsilon_n(\mathbf{k}))\Omega_n^l(\mathbf{k}) \tag{1.23}$$

Where ϵ_{ijl} is the antisymmetric tensor, $\epsilon_n(\mathbf{k})$ is the eigenvalues of a Bloch Hamiltonian H, and $f(\epsilon_n(\mathbf{k}))$ is the Fermi-Dirac distribution.

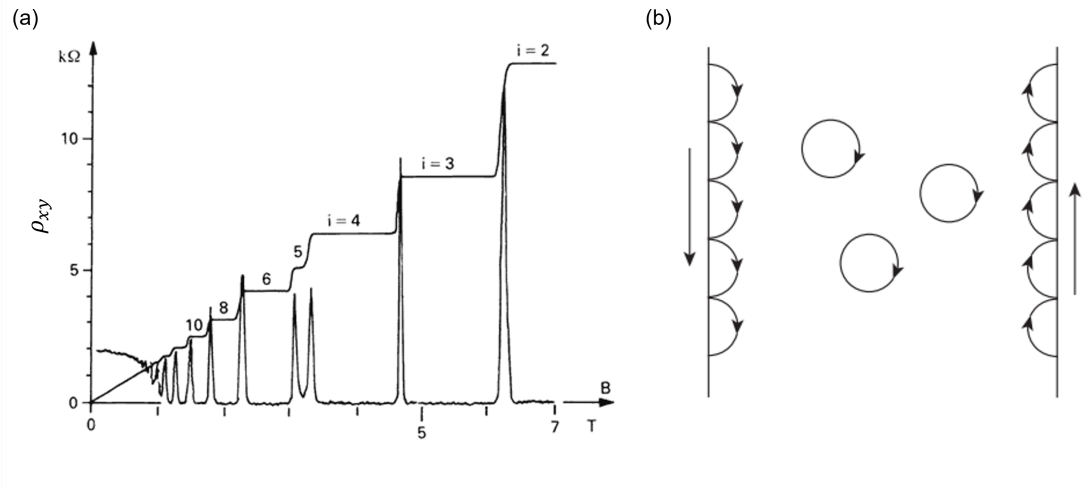

Figure 1.3: **Integer quantum Hall effect** (a) The Hall resistivity ρ_{xy} varies stepwise with the changes in magnetic field B, while the longitudinal resistivity ρ_{xx} is vanishingly small. (b) Semiclassical schematic of the integer quantum Hall effect. The circles demonstrate the cyclotron orbits of electrons in the presence of a magnetic field pointing into the paper, while the half circles represent the "skipping orbits" when electrons bounce off the sample edges. From [4, 5].

1.2.2 Quantum Hall and TKNN invairant

The integer quantum Hall effect is the first discovered topological state, characterized by a quantized Hall conductance σ_{xy} and a suppressed longitudinal conductance σ_{xx} of a two-dimensional electron gas (2DEG) under a strong magnetic field at low-temperature [23]. Semiclassically, this phenomenon can be understood as the cyclotron motion of electrons forming circular orbits in the bulk and "skipping orbits" on the edge, as Fig. 1.3(b) shows. The edge currents are subject to the external magnetic field moving in the opposite direction on the two opposite edges. Electrons in such chiral edge states are free from backscattering since the two edge states with opposite propagating directions are well separated in real space. The difference in electrochemical potential between the two dissipationless chiral edge states gives rise to the quantized Hall conductance. The quantized Hall conductance is given by:

$$\sigma_{xy} = ne^2/h \tag{1.24}$$

where n is an integer, e is the charge of an electron, and h is the Planck constant. This phenomenon can be explained by the formation of discrete, equidistant energy levels, so-called Landau levels, in the 2DEG under a strong magnetic field. By choosing the Landau Gauge for the vector potential $\mathbf{A}(\mathbf{r}) = -xB\hat{\mathbf{y}}$, the Hamiltonian can be written as:

$$H = \frac{1}{2m_e}[p_x^2 + (p_y - \frac{eB}{c}x)^2] \tag{1.25}$$

where the periodic potential and corresponding band structure were ignored for simplicity in the demonstration. Since such a system is translational invariant in y direction, the Hamiltonian can be further simplified to be that of a 1D harmonic oscillator:

$$H_k = \frac{p_x^2}{2m_e} + \frac{1}{2}m_e\omega_c^2(x - kl^2)^2 \tag{1.26}$$

Where $\omega_c = \frac{eB}{m_e c}$ is the cyclotron frequency and $l = \sqrt{\frac{\hbar c}{eB}}$ is the magnetic length. The energy eigenvalues of the Hamiltonian is, therefore, the same as those of the harmonic oscillator:

$$E_{k,n} = (n + \frac{1}{2})\hbar\omega_c \tag{1.27}$$

The corresponding eigenfunctions are given by:

$$\psi_{nk}(\mathbf{r}) = e^{iky}H_n(x/l - kl)e^{-\frac{1}{2l^2}(x-kl^2)^2} \tag{1.28}$$

where H_n is the nth Hermite polynomial. The degeneracy in each Landau level can be calculated by the formula:

$$N = \sum_k 1 = \frac{L_y}{2\pi}\int_0^{L_x/l^2} dk = \frac{L_x L_y}{2\pi l^2} = \frac{\Phi}{\Phi_0} \tag{1.29}$$

where $\Phi = BA$ is the flux in the system and $\Phi_0 = \frac{hc}{e}$ is the flux quantum. We can rewrite the Hall coefficient as:

$$R_H = \frac{B}{nec} = \frac{h}{e^2}\frac{Be}{nhc} = \frac{h}{e^2}\frac{BA}{hc/e}\frac{1}{nA} = \frac{h}{e^2}\frac{\Phi}{\Phi_0}\frac{1}{N_e} \tag{1.30}$$

Based on Eq. 1.27, Eq. 1.29, and Eq. 1.30, it is clear that as the external magnetic field B increases, the energy spacing between the Landau levels expands, the number of states in each landau level increases, and electrons tend to occupy lower Landau levels. As each

landau level is filled, the Hall conductance increases by a quantized value of e^2/h, while the longitudinal conductance lays in the insulating regime. In the presence of disorders, the Landau levels are broadened, and thus the Hall conductance forms a series of step-like quantized plateaus.

As we generalize the Landau levels into three-dimensional electronic systems, we would see the occupation of the highest Landau level ranges from completely full to entirely empty, leading to the quantum oscillations in magnetization (De Haas-Van Alphen effect) and conductivity (Shubnikov-de Haas effect).

The quantization of the Hall conductance plateau is found to be extremely precise (one part in 10^9), independent of the details of the Hamiltonian. The universality and robustness of the quantized Hall conductance result from the fact that the physics observable σ_{xy} can be represented by a topological invariant, the Thouless-Kohmoto-Nightingale-Nijs (TKNN) invariant [24]. The TKNN invariant characterizes the topology of the occupied energy bands in a system and is closely related to the Chern number. The TKNN invariant is defined as:

$$n = \frac{1}{2\pi} \int_{BZ} d^2k \sum_n \Omega_n(\mathbf{k}) \tag{1.31}$$

which has the same form as the total Chern number $\sum n$ (Eq. 1.22) of all the occupied bands. Using the Kubo formula, TKNN showed that the n in σ_{xy} (Eq. 1.24) has the same form as the TKNN invariant (1.31). Such a topological invariant protects the topological states so that they are robust against smooth changes of the Hamiltonian, unless a quantum phase transition happens leading to a change of the topological invariant.

1.2.3 Topological insulators and Z_2 Invariant

The integer quantum Hall effect is present only when the time-reversal symmetry is broken, which raises the question of whether there are topological states in the presence of time-reversal symmetry. The answer is yes. In 2005, Kane and Mele proposed a model in graphene with a spin-orbital coupling (SOC) term [25]:

$$H_{SO} = \Delta_{SO} \psi^\dagger \sigma_z \tau_z s_z \psi \tag{1.32}$$

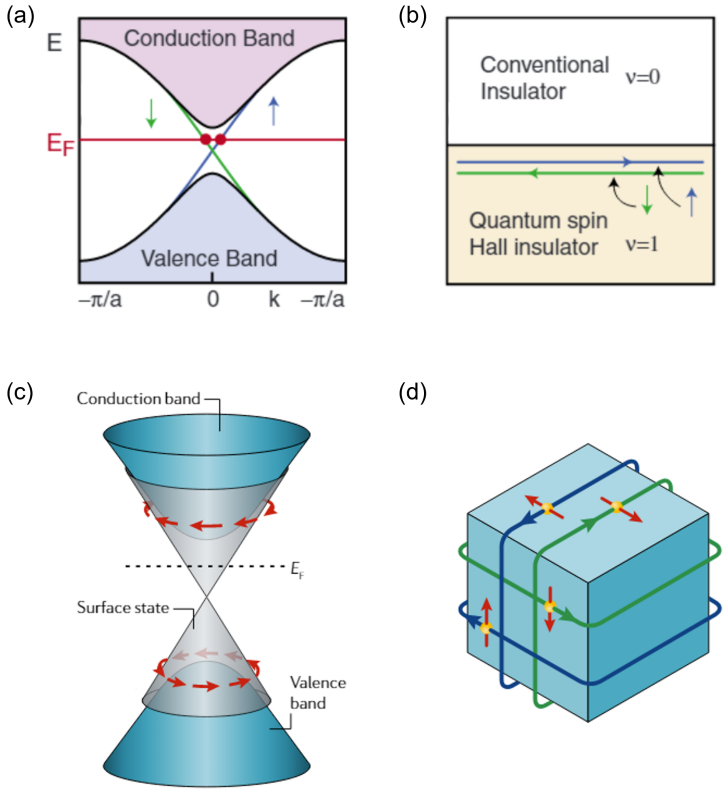

Figure 1.4: **2D and 3D topological insulators** (a) Energy dispersion of the QSH insulator in the Kane-Mele model (b) Edge states in the QSH insulator (c) Electronic structure of a 3D TI with massless Dirac-like surface states with spin-momentum locking (d) Surface states of a 3D TI in real space. Taken from [6, 7].

where the σ_z, τ_z, and s_z are the Pauli matrices representing the sublattice, valley, and electron spin, respectively. This spin-orbit coupling term opens up a gap while preserving the time-reversal symmetry $\mathcal{T}$. Unlike the conventional gap in a normal insulator, this gap in the Kane-Mele model is topologically non-trivial and gives rise to the quantum spin Hall insulator (QSHI). The QSH state is characterized by two counter-propagating copies of dissipationless charge flow with opposite spin locked to its momentum, which is the so-called helical edge state.

More generally, such a topologically non-trivial band insulator that respects the time-

reversal symmetry can exist even when the spin S_z is not a good quantum number, which is the so-called topological insulator (TI). A 2D TI is characterized by its insulating bulk and conductive helical edge states, while a 3D TI has insulating bulk states and Dirac-cone-like surface states with spin-momentum locking. The gapless Dirac-like 2D surface states in a 3D TI can be described by the Hamiltonian:

$$H = v_F(-k_y\sigma_x + k_x\sigma_y) \tag{1.33}$$

where v_F is the Fermi velocity and σ_x and σ_y are the Pauli matrices for spin. Such edge or surface states are protected by the time-reversal symmetry and the corresponding Kramers' degeneracy, which guarantees the band degeneracy at the corner of the first Brillouin Zone (e.g. $k_x = 0, \pi/a, k_y = 0, \pi/a$ in the 2D case.) In the context of edge or surface modes, back-scattering is strictly prohibited as it would violate the Kramers degeneracy.

The topological nature of the TI is described by the Z_2 invariant. For a 2D TI, Z_2 invariant ν is defined as [26]:

$$(-1)^\nu = \prod_{a=1}^{4} \delta_a \tag{1.34}$$

where δ_a is the Pfaffian of a matrix $w_{mn} = \langle u_m(\mathbf{k})| \boldsymbol{\Theta} |u_n(\mathbf{k})\rangle$ evaluated at the time-reversal invariant momenta (TRIM) Λ and $\boldsymbol{\Theta}$ is the time reversal operator.

$$\delta_a = Pf[w(\Lambda_a)]/\sqrt{Det[w(\Lambda_a)]} \tag{1.35}$$

Such a Z_2 invariant ν distinguishes between topologically trivial and non-trivial phases, with $\nu = 1$ denoting the topologically non-trivial phase and $\nu = 0$ denoting the topologically trivial case.

The evaluation of the Z_2 invariant can be simplified if additional symmetry is present. For example, in the case of a QSHI, the spin-up and spin-down states can be represented by two Chern numbers $n_\uparrow$ and $n_\downarrow$.While the time-reversal symmetry guarantees that $n_\uparrow + n_\downarrow = 0$, the difference $(n_\uparrow - n_\downarrow)/2$ can simply describe the topology of a QSHI. The Z_2 invariant, in this case, is simplified as:

$$\nu = (n_\uparrow - n_\downarrow)/2 \ mod\ 2 \tag{1.36}$$

In an inversion-symmetric system, the Z_2 invariant can be calculated by the direct product of the parity eigenvalues ξ at the four Λ points.

$$\delta_a = \prod_m \xi_m(\Lambda_a) \tag{1.37}$$

In the case of 3D TI, four Z_2 invariants $(\nu_0; \nu_1\nu_2\nu_3)$ are used to fully characterize its band topology, where ν_0 is the 3D Z_2 invariant and $\nu_{1,2,3}$ are 2D Z_2 invariants. If $\nu_0 = 0$ and ν_1, ν_2 or ν_3 is nonzero, a weak TI is identified, which can be seen as stacks of weakly coupled 2D TIs along the $(\nu_1\nu_2\nu_3)$ direction. If $\nu_0 = 1$, it represents a strong TI in 3D whose topologically non-trivial band structures cannot be continuously deformed into stacks of weakly coupled 2D TIs. In practice, one feasible method to calculate the Z_2 invariant is through the use of the Wannier charge center (WCC) method.

Material-wise, a wide range of 2D and 3D TIs have been discovered to date. Although the Kane-Mele model was proposed in a graphene system [25], it ended up with the SOC in graphene being too weak for observing the QSH effect proposed in the Kane-Mele model. Instead, the first 2D TI was realized in (Hg,Cd)Te quantum wells as proposed by Bernevig, Huges, and Zhang [27] by fine-tuning the band gap via varying the thickness of HgTe in the quantum well [28]. Later on, a series of monolayer transition metal dichalcogenides (TMDC) such as WTe_2, $MoTe_2$ in the 1T' phase were predicted as 2D TIs [29]. An extensive amount of experimental evidence has shown the monolayer 1T'-WTe_2 is a 2D TI [30, 31, 32].

The first 3D TI was realized in the $Bi_{1-x}Sb_x$ alloy with x between 0.07 and 0.22, where the characteristic surface bands were directed mapped by angle resolved photoemission spectroscopy (ARPES) [33]. Later on, a group of stiochoimetric 3D TIs with a single surface Dirac cone and large band gap was found in Bi_2Te_3, Bi_2Se_3, and Sb_2Te_3 [34, 35, 36, 37], providing an ideal platform to study the unique properties associated with band topology. For example, on the basis of $Bi_2(Te/Se)_3$, topological superconductivity candidate was found with Cu intercalations [38], whereas magnetic topological insulator (MTI) with quantum anomalous Hall effect was first discovered in Cr doped $(Bi/Sb)_2Te_3$ [8]. The focus of this thesis, $MnBi_2Te_4$, the first intrinsic MTI, is also based on the series of TIs Bi_2Te_3. It provides a valuable platform to study the interplay between magnetism and band topology,

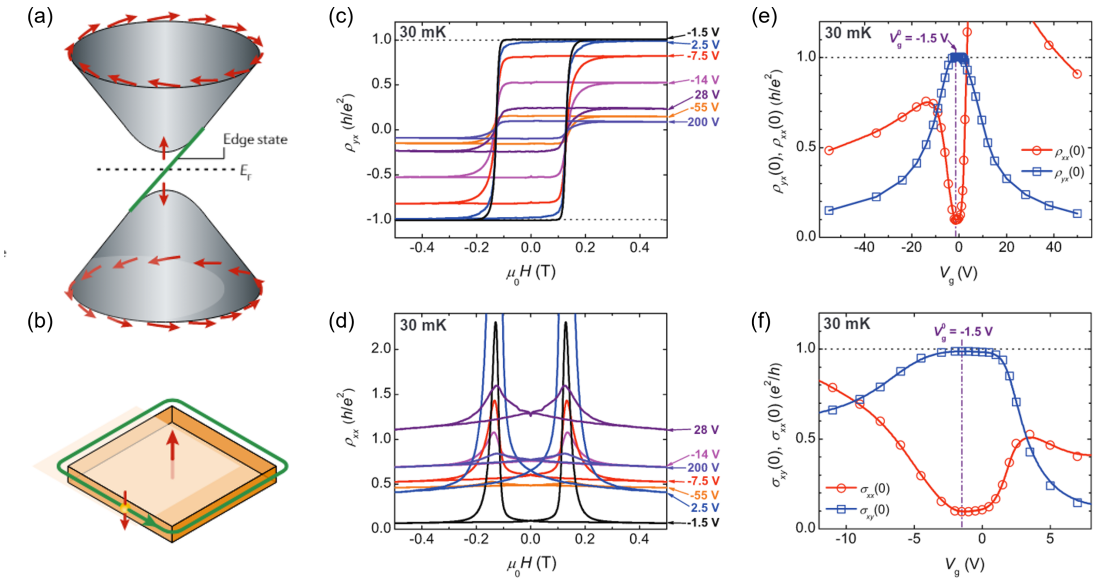

Figure 1.5: **Magnetic topological insulator and quantum Anomalous Hall effect** (a) Schematic of the gapped Dirac-like dispersion of the surface state in a MTI. (b) Schematic of the chiral edge mode that appears in a MTI when the Fermi level, E_F, is located in the mass gap induced by the magnetic exchange interaction. (c)-(f) QAH effect measured in Cr doped (Bi, Sb)$_2$Te$_3$ (c) Magnetic field dependence of ρ_{yx} at different bottom gate voltage V_{gS}. (d) Magnetic field dependence of ρ_{xx} at different bottom gate voltage V_{gS}. (e) The gate dependence of $\rho_{yx}(0)$ (empty blue squares) and $\rho_{xx}(0)$ (empty red circles). (f) The gate dependence of $\sigma_{xy}(0)$ (empty blue squares) and $\sigma_{xx}(0)$ (empty red circles) on V_g. Adapted from [7, 8].

as we will discuss in later chapters.

1.2.4 Magnetic topological insulators

A necessary condition for forming a topological nontrivial insulator is the band inversion and band gap reopening caused by spin-orbit interaction. We have introduced both the theoretical model and material realizations of such TIs in the presence of time-reversal symmetry in the last section 1.2.3. In fact, in the presence of a spontaneous magnetization or, equivalently, a broken time-reversal symmetry, the nontrivial band topology and its corresponding topologically protected edge states still exist, but with certain modifications.

Unlike the gapless Dirac-like surface states in 3D TIs (Eq. 1.33), the surface states of a 3D MTI open up an exchange gap in the Dirac gap dispersion due to the coupling between spontaneous magnetization and the conduction electrons, as described by the model Hamiltonian:

$$H = v_F(-k_y\sigma_x + k_x\sigma_y) + m\sigma_z \tag{1.38}$$

1.2.4.1 Quantum Anomalous Hall insulator

In the 2D limit, by tuning the Fermi level into the exchange gap, one can observe a quantized Hall conductance with vanishing longitudinal conductance in the absence of an external magnetic field, which is the so-called quantum anomalous Hall (QAH) effect [39]. Although the QAH effect is usually introduced as the equivalent of the IQH effect at zero magnetic field due to their similarities in the quantized Hall conductance σ_{xy} and dissipationless chiral edge mode, the microscopic origins of the quantization of IQH and QAH effects are quite different. In IQH insulators, the quantization is the result of the formation of Laudau levels originating from the cyclotron motion of 2D charge carriers as introduced in section 1.2.2, while in QAH insulators, the quantization is related to the opening of an exchange gap near the Fermi energy E_F.

Chern number can be used to describe its band topology. It can be defined as:

$$C = 2\int_{BZ} \hat{\mathbf{R}} \cdot (\frac{\partial \hat{\mathbf{R}}}{\partial k_x} \times \frac{\partial \hat{\mathbf{R}}}{\partial k_y})\frac{dk_x dk_y}{4\pi} = sgn(m) \tag{1.39}$$

where $\mathbf{R} = (-v_F k_y, v_F k_x, m)$ and $\hat{\mathbf{R}} = \mathbf{R}/|\mathbf{R}|$. The Chern number of the QAH state is equal to the sign of the mass term, which depends on the sign of the exchange coupling and the magnetization direction.

The QAH effect was initially proposed in honeycomb and kagome lattices with staggered magnetic fluxes. However, it was not realized in experiments for more than a decade due to the difficulties in material design and device fabrication. In 2013, the QAH effect was first realized experimentally in Cr doped $(Bi_{0.1}Sb_{0.9})_2Te_3$ thin film on a $SrTiO_3$ substrate at T

= 30 mK [8]. In this case, the ferromagnetism is mediated by the local valence electrons, via van Vleck or Bloembergen-Rowland mechanism. Shortly after, the QAH effect was also observed in V doped $(Bi_{1-y}Sb_y)_2Te_3$ with a better quantization at 25mK which persists to about 120mK [40]. Although the Curie temperature in the transition metal (Cr or V) doped $(Bi,Sb)_2Te_3$ is relatively high ($\sim$ 20K), the quantization of Hall conductance is only observable at 10s or 100s of millikelvin. This is probably due to the existence of dissipative channels, such as the residual carriers from the bulk band, impurity channels caused by defects and magnetic dopants, and nonchiral quasi-helical edge modes.

1.2.4.2 Axion insulator

While a QAH insulator, which breaks time-reversal symmetry, is characterized by the Chern number (Eq. 1.39), there exists another type of MTI, called axion insulator that is protected by inversion and time reversal, or the composition of either one with a rotation or a translation [41]. Axion is a hypothetical particle in high-energy physics, which possibly explains the strong charge-parity problem in quantum chromodynamics and is a candidate for dark matter. In the context of condensed matter systems, in analogy to the axion field in high-energy physics, the electromagnetic response of an axion insulator can be described by an effective axion field θ in topological field theory:

$$\theta = -\frac{1}{4\pi}\int_{BZ} d^3k\ \epsilon^{\mu\nu\sigma} Tr[A_\mu \partial_\nu A_\sigma - \frac{2i}{3} A_\mu A_\nu A_\sigma] \tag{1.40}$$

where A is the Berry connection, ϵ is the Levi-Civita symbol, and the trace runs over the band index of the Berry connection over occupied bands. The axion field θ can also be understood as a contribution to the magnetoelectric polarization from extended orbitals.

In the presence of the axion field θ, an additional term $\mathcal{L}_\theta$ needs to be added to the Lagrangian:

$$\mathcal{L}_\theta = \frac{\alpha}{4\pi^2}\theta\ \mathbf{E}\cdot\mathbf{B} \tag{1.41}$$

where α is the fine-structure constant. This term leads to a modification to the Maxwell equation:

$$\nabla\cdot\mathbf{E} = 4\pi\rho - \frac{\alpha}{\pi}(\nabla\theta)\cdot\mathbf{B} \tag{1.42}$$

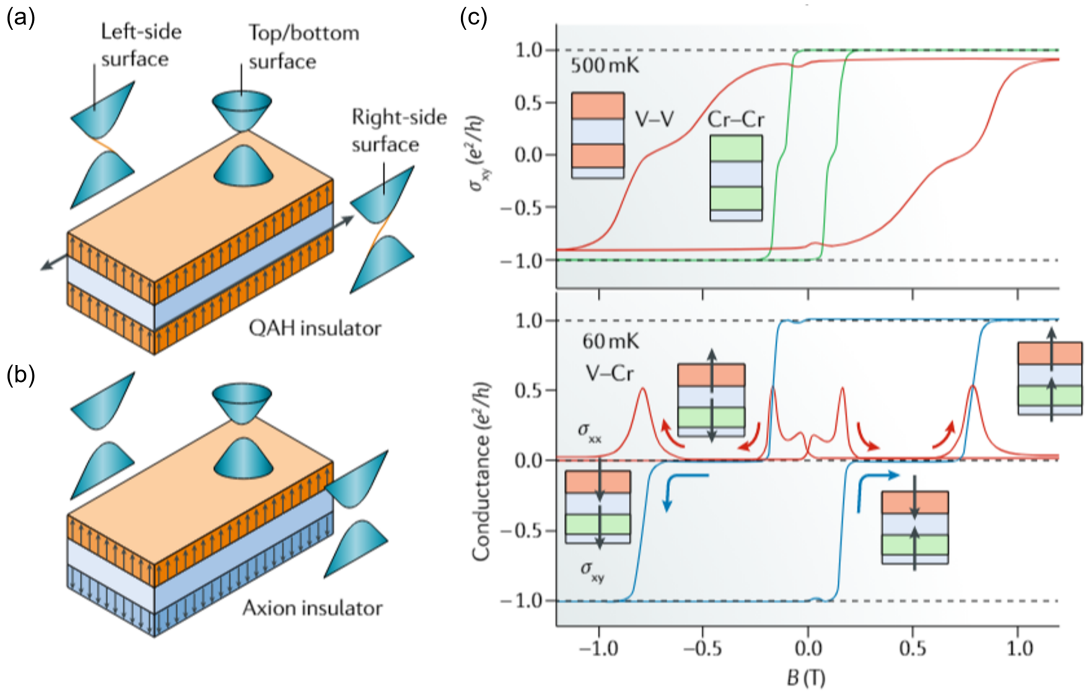

Figure 1.6: **Axion insulator states in magnetic topological insulator heterostructures** (a) schematic of a QAH state with parallel magnetization directions on the top (V-doped) and bottom (Cr-doped) magnetic layers (b) schematic of an axion insulator state with antiparallel magnetization on those layers. (c) The top panel shows the magnetic field dependence of σ_{xy} at 500 mK for symmetric modulation-doped heterostructures with V (pink) and Cr (green). The lower panel shows σ_{xy} and σ_{xx} at 60 mK for V-doped and Cr-doped heterostructures. The insets show the magnetization configuration at each magnetic field. From [7, 9]

$$\nabla \times \mathbf{B} = \frac{4\pi}{c}\mu_0 \mathbf{J} + \frac{1}{c}\frac{\partial \mathbf{E}}{\partial t} + \frac{\alpha}{\pi}[\frac{1}{c}\mathbf{B}(\frac{\partial}{\partial t}\theta) + (\nabla\theta) \times \mathbf{E}] \tag{1.43}$$

The application of a magnetic field induces electric polarization, whereas an electric field induces magnetization.

$$\mathbf{P} = \frac{e^2}{2h}\frac{\theta}{\pi}\mathbf{B} = \sqrt{\frac{\epsilon_0}{\mu_0}}\alpha\frac{\theta}{\pi}\mathbf{B} \tag{1.44}$$

$$\mathbf{M} = \frac{e^2}{2h}\frac{\theta}{\pi}\mathbf{E} = \sqrt{\frac{\epsilon_0}{\mu_0}}\alpha\frac{\theta}{\pi}\mathbf{E} \tag{1.45}$$

Such magnetoelectric effects broadly exist not only in axion insulators and TIs but also in some topologically trivial materials with non-vanishing θ, such as the magnetoelectric

Cr_2O_3 and multiferroic (Fn, Zn)$_2Mo_3O_8$.

However, the magnetoelectric effect is more significant in TIs and axion insulators, where θ is quantized ($\theta = \pi$). The direct consequence of a quantized axion field in the bulk is a half-quantized Hall effect on the surface. To produce an axion insulator, it is necessary to realize an antiparallel magnetization (M) or an opposite sign of the exchange gaps on the top and bottom surfaces. Therefore, the half-quantized Hall conductances on the top and bottom surface ($\sigma_{xy} = \pm\frac{e^2}{2h}$) of an axion insulator cancel each other, forming a zero Hall conductance plateau, which characterizes the axion insulator. Such a zero Hall plateau was previously observed in a modulation-doped heterostructure of (Bi,Sb)$_2$Te$_3$ with V and Cr where the magnetization M pointing up on the top surface and down on the bottom surface [9], as the lower panel of Fig. 1.6(c) shows. Due to the large coercive field difference between the two magnetic layers as the upper panel of Fig. 1.6(c) shows, an antiparallel magnetic configuration on the top and bottom surface when the magnetic field B is in between the coercive field of the V doped layer and Cr doped leads to a broad zero Hall conductance plateau.

Another consequence of the quantized axion field is the quantized rotation of the field polarization axis in the units of the fine structure constant α. Such a quantization in optical-magnetic responses can be measured by performing both Kerr and Faraday rotation measurements with a low-frequency optical probe (e.g. terahertz spectroscopy), whose energy is lower than the exchange gap of the surface state.

1.2.5 Dirac and Weyl semimetals

The previously introduced topological states are all insulators, where topological invariants could be sharply delineated due to the presence of energy gaps. It is natural to ask "Do topological quantum numbers exist in metals where there is no such gap?". It turns out that topological states can also exist in metals.For instance, when transitioning from a 3D TI to a trivial insulator through a gapless state, a Dirac semimetal phase can be realized in the presence of both time reversal and inversion symmetry [42]. If the time-reversal symmetry or the inversion symmetry is lost, the massless Dirac point could expand into a pair of Weyl

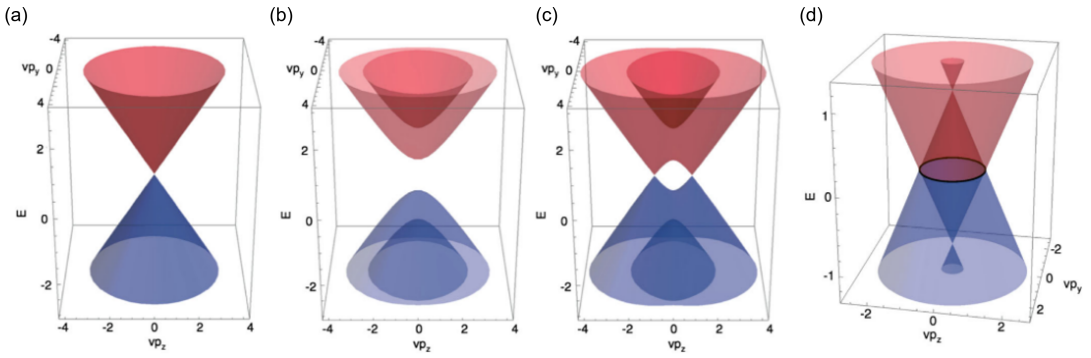

Figure 1.7: **Electronic structures of topological semimatels.** Schematic electronic structures of (a) Dirac semimetal (b) magnetic semiconductor (c) Weyl semimetal (d) nodal line semimetal. Taken from [10].

nodes with opposite chiralities, leading to a Weyl semimetal phase. Both the low-energy excitations of Dirac and Weyl semimetals are quasiparticles of relativistic fermions, which can be described by the Dirac equation and Weyl equation, respectively. Their characteristic electronic properties lead to exotic surface states in the form of Fermi arcs and novel responses to applied electric and magnetic fields, such as the intrinsic anomalous Hall effect and chiral anomaly.

1.2.5.1 Dirac semimetal

The Dirac equation was proposed by Paul A.M. Dirac in 1928 [43], to describe the wave function of a spin $\frac{1}{2}$ particle in relativistic quantum mechanics:

$$(i\gamma^{\mu}\partial_{\mu} - m)\psi = 0 \tag{1.46}$$

where $\mu = 0, 1, ..., d$ denotes the time and space dimensions, γ are anti-commuting matrices with $\{\gamma^{\mu}, \gamma^{\nu}\} = 0, \mu \neq \nu$ and $(\gamma^0)^2 = -(\gamma^i)^2 = \mathbb{1}$, and effective speed of light $c = 1$. For 1 and 2 dimensions, γ are two and three (2×2) matrices, while for 3 dimensions, γ are four (4×4) matrices. By solving the Dirac equation, one would get:

$$E_{\pm} = \pm\sqrt{m^2 + p^2} \tag{1.47}$$

When the mass term vanishes ($m = 0$), the energy depends linearly on momentum with a speed of the effective speed of light $c = 1$.

Quasiparticles of Dirac fermions described by the massless Dirac equation can be found in condensed matter systems. While the best-known example is graphene, whose linear energy dispersion near the K and K' points is captured by the massless 2D Dirac equation, a Dirac semimetal usually refers to a 3D topological phase of matter. It is characterized by a unique electronic structure in which the conduction band and valance band cross at discrete points, forming linear band crossings described by massless Dirac equations (Eq. 1.7(a)). These crossing points stabilized by inversion, time reversal, and certain crystal symmetries are called Dirac points.

1.2.5.2 Weyl semimetal

In 1929, Weyl introduced a simplified version of the Dirac equation (Eq. 1.46) in odd spacial dimensions, which led to the foundation of Weyl semimetals. For simplicity, we first consider d=1. One only needs two anticommuting matrices: $\gamma^0 = \sigma_z$ and $\gamma^1 = i\sigma_y$, where σ_z and σ_y are the Pauli matrices. If a massless particle is considered, the equation can be simplified as $i\partial_t\psi = \gamma_5 p\psi$, where $\gamma_5 = \gamma^0\gamma^1 = \sigma^x$ and $p = -i\partial_x$. By picking the eigenstates of the Hermitian matrix $\gamma_5\psi_\pm = \pm\psi_\pm$, one would obtain the 1D Weyl equation:

$$i\partial_t\psi_\pm = \pm p\psi_\pm \tag{1.48}$$

The solution to the Weyl equation $E_\pm(p) = \pm p$ represents a right-moving particle and a left-moving particle, respectively.

In three dimensions, the gamma matrices are (4×4) anti-commuting matrices: $\gamma^0 = \mathbb{1} \otimes \tau_x$, $\gamma^i = \sigma^i \otimes i\tau_y$, and $\gamma^5 = -\mathbb{1} \otimes \tau_z$. The 3D Weyl equation is thus given by:

$$i\partial_t\psi_\pm = \mp\mathbf{p} \cdot \sigma\psi_\pm \tag{1.49}$$

The corresponding Weyl fermions, therefore, propagate parallel or antiparallel to their spin, which represents the so-called chirality. A single Weyl fermion in an electromagnetic field will lead to a violation of charge conservation law. In consequence, Weyl fermions with opposite chiralities appear in pairs in Weyl semimetals. Fig. 1.7(c) shows a schematic of

the electronic structure of Weyl semimetals, obtain by lifting up the band degeneracies in a Dirac semimetal (Fig. 1.7(a)) by applying a Zeeman field to break the time-reversal symmetry.

To realize a WSM, one needs to find a 3D crystal with nondegenerate bands by breaking inversion or time-reversal symmetry. Under the combined symmetry operation of the inversion and TRS $\widetilde{\mathcal{T}} = \mathcal{P}\mathcal{T}$, crystal momenta are invariant and $\widetilde{\mathcal{T}}^2 = -1$, leading to a doubly degenerate energy band. Furthermore, the chirality of the Weyl nodes is even under TRS and odd under inversion. Thus, in the presence of the combined $\widetilde{\mathcal{T}} = \mathcal{P}\mathcal{T}$ symmetry, two Weyl nodes with opposite chirality are degenerate, which will lead to the annihilation of Weyl nodes.

When either inversion or time-reversal symmetry is broken, the bands typically become nondegenerate, and it can be shown that there exist band crossings whose low energy excitations resemble Weyl fermion due to accidental degeneracies. Consider a universal 2×2 Hamiltonian that describes the two energy bands closest to the Fermi level:

$$H(\mathbf{k}) = f_0(\mathbf{k})\mathbb{1} + f_1(\mathbf{k})\sigma_x + f_2(\mathbf{k})\sigma_y + f_3(\mathbf{k})\sigma_z \tag{1.50}$$

To achieve band crossings, the conditions $f_1 = f_2 = f_3 = 0$ must be met. In three-dimensional materials, we have three independent variables k_x, k_y, k_z to satisfy this condition. As a result, the band crossings can be realized without fine-tuning the energy bands, enabling the existence of accidental twofold degeneracies in three-dimensional solids in the absence of any symmetry.

Furthermore, to ensure the generic linear dispersion near the Weyl point, we can expand the Hamiltonian about $\mathbf{k} = \mathbf{k_0} + \delta\mathbf{k}$:

$$H(\mathbf{k}) = f_0(\mathbf{k})\mathbb{1} + \mathbf{v_0} \cdot \delta\mathbf{k}\mathbb{1} + \sum_{a=x,y,z} \mathbf{v_a} \cdot \delta\mathbf{k}\sigma^a \tag{1.51}$$

where $\mathbf{v}_\mu = \nabla_k f_\mu(\mathbf{k})|\mathbf{k} = \mathbf{k_0}(\mu = 0, ..., 3)$. To ensure the band crossings near the Fermi energy, $f_0(\mathbf{k}_0)$ has to be a value close to 0. If $\mathbf{v}_0 = 0$ and $\mathbf{v}_a = v_0\hat{a}$ (a = x,y,z), the Weyl equation (Eq. 1.49) is retrieved. Consequently, one can conclude that Weyl nodes can exist in three-dimensional solids due to accidental symmetry. Moreover, the Weyl nodes are stable against small perturbations. Since if a small perturbation is applied on f_a, the

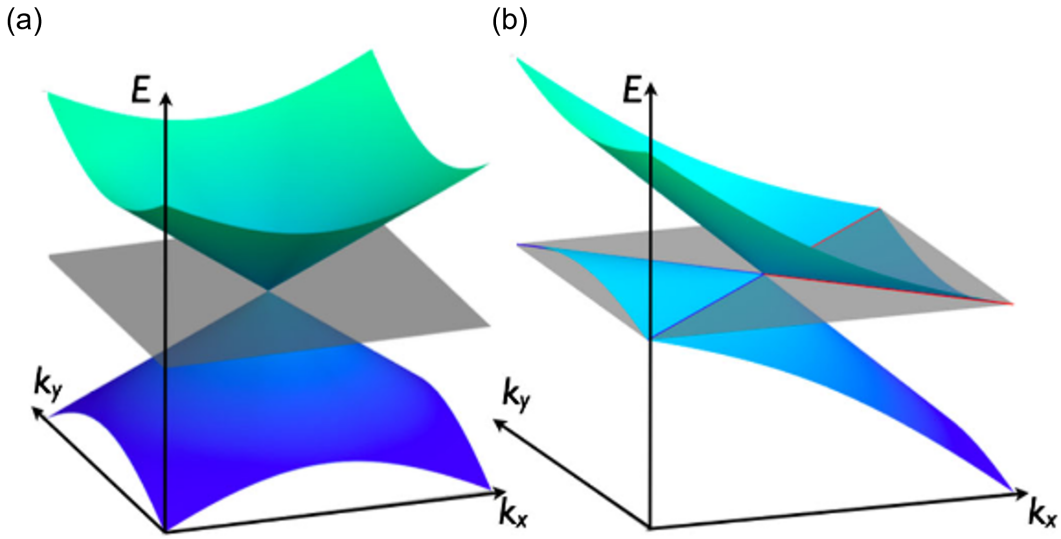

Figure 1.8: **Electronic structures near a type-I and type-II Weyl node** (a) Electronic structure near a type-I Weyl node with an untilted (or slightly tilted) Weyl cone and a point like Fermi surface (b) Electronic structure near a type-II Weyl semimetal with a tilted Weyl cone and a coexistence of electron and hole Fermi pockets touching at the Weyl point. Taken from [10].

band crossing (i.e. Weyl node) will move in three-dimensional space, but will not disappear unless annihilating with another Weyl node of opposite chirality.

To realize a Weyl semimetal, a 3D crystal with nondegenerate bands must be found by breaking either inversion or time-reversal symmetry. Inversion symmetry broken WSMs with preserved TRS have at least four Weyl nodes. The chirality of Weyl nodes is even under TRS, meaning that a Weyl node at $\mathbf{k}$ with a fixed chirality (e.g., C = 1) ensures the existence of another Weyl node at $-\mathbf{k}$ with the same chirality. To conserve chirality, there must be at least four Weyl nodes in a WSM with broken inversion symmetry but preserved TRS. For WSMs with broken TRS but preserved inversion symmetry, it is possible to realize the ideal WSM phase with a single pair of Weyl nodes having opposite chiralities. This is due to the chirality being odd under inversion symmetry. In such scenarios, in the absence of other topologically trivial bands at the Fermi energy, the physical properties of the Weyl

nodes can be studied without ambiguity, leading to a better understanding of their unique characteristics.

In addition to the type-I WSM phase, which is described exactly by the Weyl equation (Eq. 1.49), there exists another type of WSM, known as type-II WSM. This occurs when the velocity parameter $\mathbf{v}_0$ in Eq. 1.51 introduces a large enough tilt of the Weyl cone that violates Lorentz invariance. In a type-I WSM, the Weyl cone is untilted or slightly tilted, with electron and hole pockets occupying separate energy levels above or below the Weyl points, as Fig.1.8(a) shows. When the Fermi level is at the Weyl point, the Fermi surface is point-like. On the other hand, a type-II WSM allows for the coexistence of electron and hole pockets at certain Fermi energy levels (Fig. 1.8(b)). When the Fermi level is tuned precisely to the Weyl point, the coexisting electron and hole pockets intersect at the Weyl nodes, creating a unique electronic structure in these materials.

Weyl nodes act as monopoles of Berry flux. The Berry flux on a surface surrounding a Weyl point is exactly $2\pi C$, where C represents the chirality. The field lines of Berry flux for a pair of Weyl nodes with opposite chiralities resemble the field lines of the magnetic field created by magnetic monopoles, as illustrated in Fig. 1.2(b). This unique topology of WSMs leads to remarkable phenomena, including:

1. Fermi Arcs: Fermi arcs are unique surface states that connect pairs of Weyl nodes with opposite chiralities on the surface Brillouin zone, resulting in intriguing transport and optical properties (Fig. 1.9). These surface states arise due to the topological protection provided by the underlying bulk Weyl points. Unlike closed loops, Fermi arcs form open curves in momentum space, serving as strong evidence for the existence of a WSM. When the Fermi energy is away from the Weyl points, the Fermi arc connects two bulk Weyl pockets tangentially (Fig. 1.9(b)). Even when two Weyl pockets merge, Fermi arcs can persist. Visualization of Fermi arcs is possible through techniques such as ARPES (Fig. 1.9(c)) and scanning tunneling spectroscopy (STM). Moreover, quantum oscillation measurements involving closed loops of Fermi arcs and certain bulk states with specific geometries can provide further insight into Fermi arc properties.

2. Chiral Anomaly: The chiral anomaly refers to the non-conservation of chiral current when an external magnetic field $\mathbf{B}$ and an external electric field $\mathbf{E}$ are applied parallel to

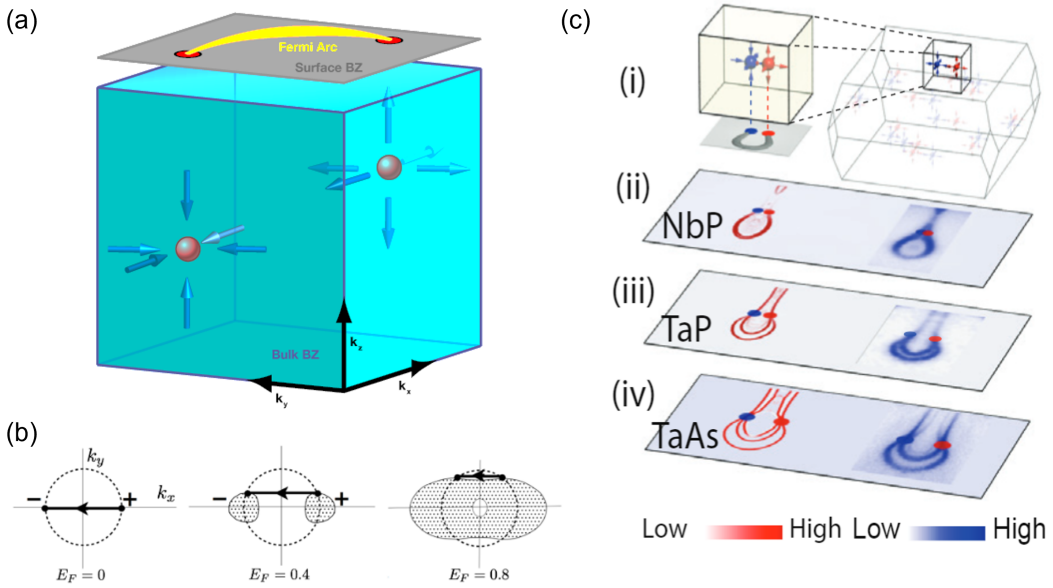

Figure 1.9: **Schematic and experimental observations of Fermi arcs** (a) Schematic of Weyl nodes and Fermi arcs in **k** space (b) Evolution of Fermi arcs as the chemical potential moves away from the Weyl nodes. (c) Comparison of theoretically calculated and experimentally observed Fermi arcs in NaP, TaP, and TaAs. Taken from [10, 11].

each other. This leads to an imbalance in the number of left-handed and right-handed Weyl fermions, and a non-zero chiral current. The chiral anomaly can be quantified by the following equation:

$$\frac{dn_{R/L}^{3D}}{dt} = \pm\frac{e^2}{h^2}\mathbf{E}\cdot\mathbf{B}, \tag{1.52}$$

To understand the chiral anomaly in 3D WSMs in a simple way, first consider the formation of Landau levels by applying a magnetic field along the z-axis, as Fig. 1.10(a) shows. In a WSM, the zeroth Landau level is chiral. Introducing an electric field parallel to the magnetic field (z-axis) generates an effective chemical potential difference between Weyl nodes with opposite chiralities, leading to a non-conserved chiral charge. As a result, a chiral magnetic effect characterized by negative magnetoresistance can be observed experimentally when the magnetic and electric fields are in parallel. The quantitative relationship between

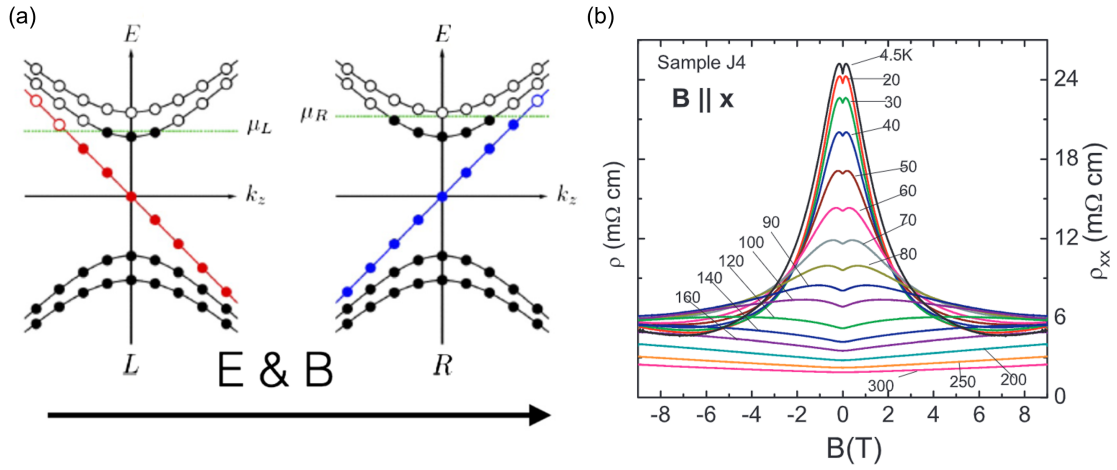

Figure 1.10: **Schematic and experimental observations of chiral anomaly** (a) Schematic of the Landau levels of a Weyl semimetal with magnetic field and electric field in parallel and along z axis. The zeroth Landau levels are chiral. (b) Chiral anomaly observed in Nb_3Bi at varied temperatures with magnetic field and electric field in parallel and along the x-axis. Taken from [10, 12].

magnetoconductivity and magnetic field can be expressed as [44]:

$$\sigma(B) = \sigma_0 + \frac{e^4 B^2 \tau_a}{4\pi^4 g(\epsilon_F)} \tag{1.53}$$

This negative magnetoresistance (or positive magnetoconductivity) exhibits a unique anisotropy concerning the angle between the electric and magnetic fields. Notably, the chiral magnetic effect persists even without reaching the quantum limit, meaning that the formation of Landau levels is not a requirement.

3. Intrinsic Anomalous Hall Conductivity: The anomalous Hall effect (AHE) is a phenomenon originally observed in ferromagnetic materials, where an electric current passing through the material generates a transverse voltage in the absence of an external magnetic field. In ferromagnetic materials, the AHE arises due to the presence of magnetization and can be explained under the influence of the anomalous velocity of the electrons, which is a consequence of spin-orbit coupling.

$$\frac{d < \vec{r} >}{dt} = \frac{\partial E}{\hbar \partial \vec{k}} + \frac{e}{\hbar} E \times \Omega_n \tag{1.54}$$

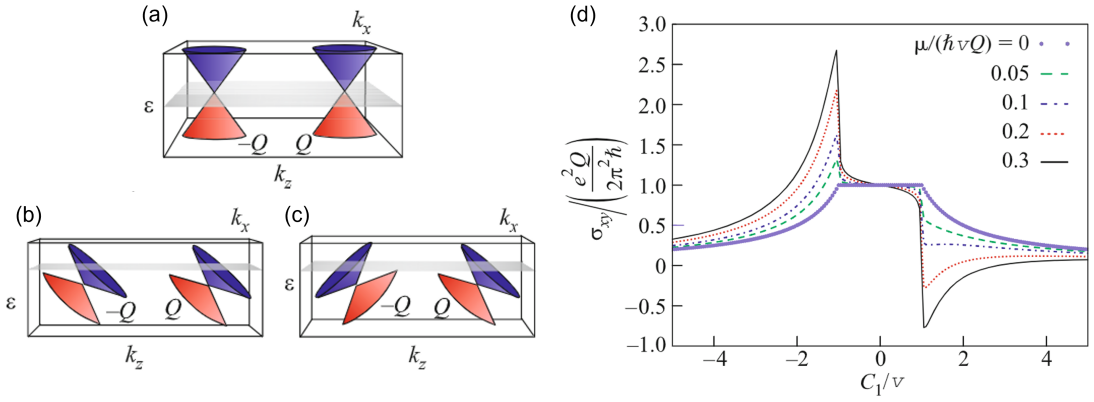

Figure 1.11: **Intrinsic anomalous Hall effect of Weyl semimetals** (a)-(c) Electronic structures of Weyl semimetals with different tilting angles. (a) an untilted type-I WSM with $C_1 = C_2 = 0$. (b) a type-II WSM with both Weyl cones tilting in the same direction with $C_1 = C_2 < -v$. (c) a type-II WSM with two Weyl cones tilting in the opposite direction with $C_1 = -C_2 < -v$ (d) Normalized anomalous Hall conductivity $\sigma_{xy}/(\frac{e^2Q}{2\pi^2\hbar})$ as a function of the tilting of the Weyl cones C_1/v for varied values of normalized chemical potential $\mu/(\hbar vQ)$ with fixed $C_2 = -C_1$. Taken from [13].

The anomalous velocity as shown in the second term of Eq.1.54 is found related to the Berry curvature Ω. As a result, the intrinsic anomalous Hall conductivity can be expressed as an integral over the Fermi sea of the Berry curvature on each occupied band:

$$\sigma_{ij}^{AH-int} = -\epsilon_{ijl}\frac{e^2}{h}\sum_n \int \frac{d\mathbf{k}}{(2\pi)^d} f(\epsilon_n(\mathbf{k}))\Omega_n^l(\mathbf{k}) \tag{1.55}$$

Where ϵ_{ijl} is the antisymmetric tensor, $\epsilon_n(\mathbf{k})$ is the eigenvalues of a Bloch Hamiltonian H, and $f(\epsilon_n(\mathbf{k}))$ is the Fermi-Dirac distribution.

In a WSM, the intrinsic anomalous Hall effect is significant due to the non-vanishing Berry curvature and the unique role of a Weyl node as a monopole of Berry curvature. In type-I Weyl semimetals, the intrinsic anomalous Hall conductivity is quantized, determined solely by the separation between Weyl nodes in momentum space Q.

$$\sigma_{xy}^{quant} = \frac{e^2Q}{2\pi^2\hbar} \tag{1.56}$$

This quantization arises due to the topological nature of Weyl nodes, which act as sources or sinks of Berry curvature. The net Berry curvature integrated over a closed surface enclosing a Weyl node is equal to the Chern number, an integer value representing the topological charge of the node.

In type-II Weyl semimetals, the intrinsic anomalous Hall depends on the chemical potential and the tilted angle of the Weyl cones. In general, the intrinsic anomalous Hall conductivity of an ideal WSM with only one pair of Weyl nodes can be approximated as:

$$\sigma_{xy}^{IAH} = \frac{e^2}{2\pi^2\hbar}[Q + \frac{\mu}{4\hbar}(\frac{1}{C_2} - \frac{1}{C_1})(ln|\frac{2\hbar v\Lambda}{\mu}| - 1)] \tag{1.57}$$

where Q is the Weyl nodes separation, μ is the chemical potential, C_1 and C_2 denote the tilting angle of the two Weyl cones, v is the Fermi velocity when $C_1 = C_2 = 0$, and Λ is the cutoff momentum. The condition $|\frac{C_{1,2}}{v}| < 1$ represents a type-I WSM (Fig. 1.11(a)), while for $|\frac{C_{1,2}}{v}| \geq 1$, the system corresponds to a type-II WSM (Fig. 1.11(b-c)). Unlike the quantized intrinsic anomalous Hall conductivity of a type-I WSM, the intrinsic anomalous Hall conductivity of a type-II WSM varies significantly with changes in the chemical potential and may exhibit a logarithmic divergence (Fig. 1.11(d)).

1.3 Overview of the topological phase diagram of $MnBi_2Te_4$

As previously introduced, significant progress has been made in MTIs through the doping of TIs with magnetic transition metals and the fabrication of magnetic topological heterostructures. However, the observation of exotic topological phenomena in MTIs, such as the QAHE and Axion insulator state, has been limited to extremely low temperatures due to the presence of impurities and inhomogeneity in doped materials, as well as the delicate proximity effect in heterostructures.

$MnBi_2Te_4$ is the first intrinsic MTI that accommodates various topological phases in different dimensions and magnetism due to the interplay between magnetism and topology. The ground state of bulk $MnBi_2Te_4$ is an antiferromagnetic TI protected by the combined half-layer lattice translation and time-reversal symmetry ($S = \tau_{1/2}\mathcal{T}$). The band gap in the bulk is topologically non-trivial and as large as 0.2 eV. Fig. 1.12(a) shows the rich topological phase diagram, which is theoretically possible to be realized in $MnBi_2Te_4$ with

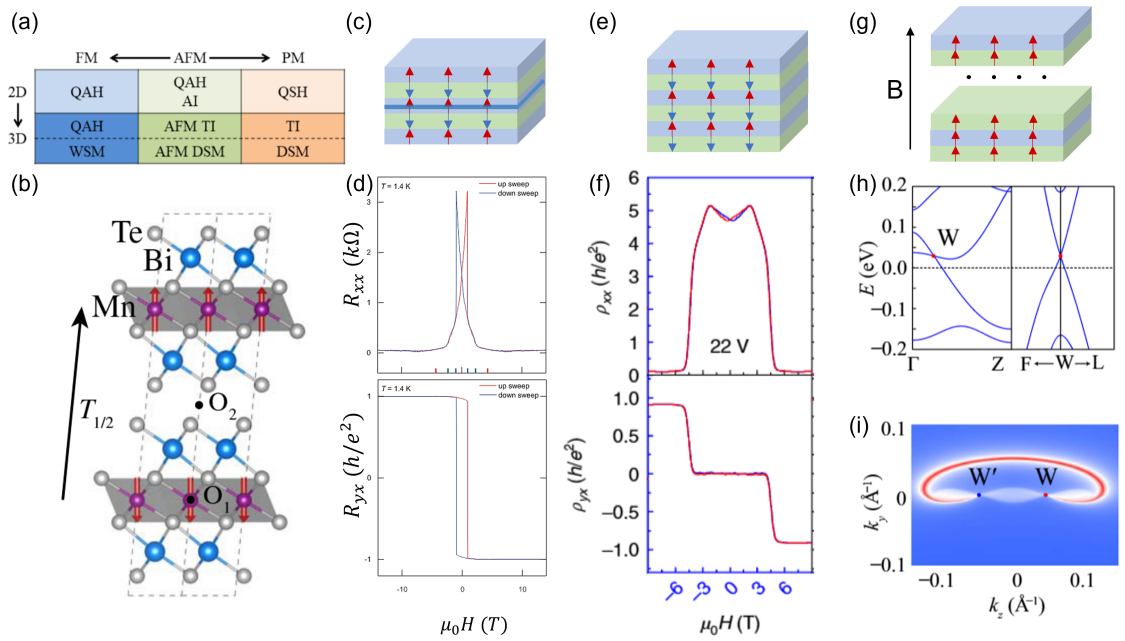

Figure 1.12: **Topological phases in $MnBi_2Te_4$** (a) Rich topological quantum states that are possible to be realized in $MnBi_2Te_4$ in different dimensions and magnetic states (AFM, FM, PM). (b) Crystal structure of $MnBi_2Te_4$. The arrow indicates the half lattice translation $\mathcal{T}_{1/2}$. (c) Schematic of 5 septuple layers of $MnBi_2Te_4$, in which evidence of the QAH state was observed. (d) Field dependence of inline resistance R_{xx} and Hall resistance R_{xy} of a 5 SL $MnBi_2Te_4$ sample at T= 1.4K and $V_g = -200V$. (e) Schematic of 6 septuple layers of $MnBi_2Te_4$, in which evidence of the Axion insulator state was observed. (f) Field dependence of inline resistivity ρ_{xx} and Hall resistivity ρ_{xy} of a 6 SL $MnBi_2Te_4$ sample at T= 1.6K and $V_g = 22V$. (g) Schematics of bulk $MnBi_2Te_4$ in the field-induced FM state, in which an ideal Weyl semimetal state was proposed. (h) electronic structures of FM-z $MnBi_2Te_4$ with a pair of type-II Weyl nodes calculated by DFT. (g) Fermi arcs connecting the two Weyl nodes with opposite charities. Panel (a), (b), (h) and (i) are taken from [14], panel (d) from [15], and panel (f) from [16].

different dimension and magnetic states. Among those, characteristic features of some of the topological states have been observed in experiments.

The thin film limit of $MnBi_2Te_4$ exhibits the QAH insulator state and axion insulator state in odd and even septuple layers, respectively. In even layers of $MnBi_2Te_4$ thin film as Fig. 1.12(e) illustrates, the time reversal symmery Θ and the inversion symmetry about the O_2 point P_2 (Fig. 1.12(b)) are broken, but the combined $P_2\Theta$ symmetry is preserved,

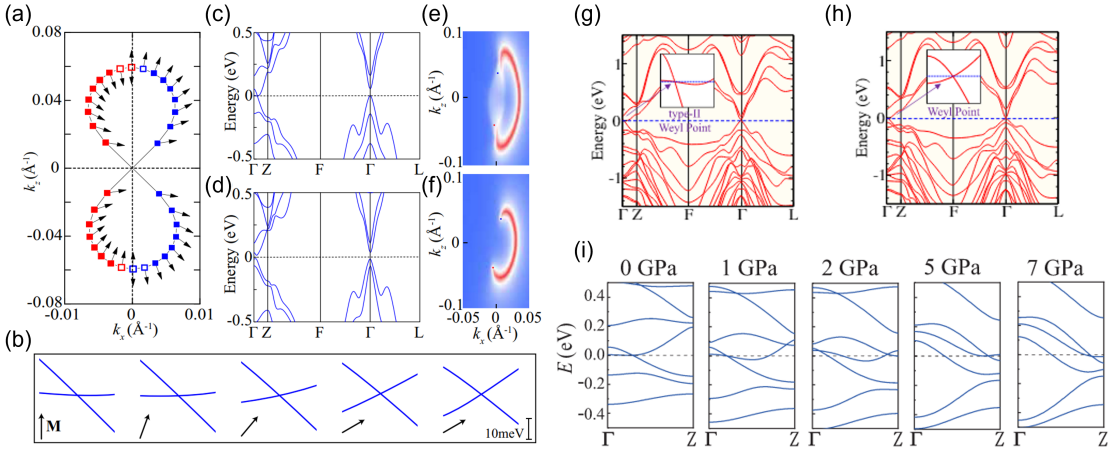

Figure 1.13: **Electronic structure calculations of the Weyl semimetal phase in bulk $MnBi_2Te_4$ under rotating magnetic field, strain and pressure** (a)-(f) Evolution of the electronic structure of bulk $MnBi_2Te_4$ in the field-induced FM state by rotating the external magnetic field angle calculated by DFT. (a) Evolution of Weyl points in momentum space when magnetic orientation denoted by black arrows rotates from the out-of-plane to in-plane direction in the $k_x - k_z$ plane. The solid and open squares denote type-I and type-II Weyl points, respectively. (b) band dispersion near Weyl points along the k_z direction for different magnetic orientations with magnetic field angles as illustrated by the black arrows. (c)-(d) Band structures and (e)-(f) surface states of FM bulk $MnBi_2Te_4$ with magnetic orientation angles of 10° (upper) and 50° (lower). (g)-(h) electronic strcuture of FM-z $MnBi_2Te_4$ under (g) 0.5% and (h) 1% of isotropic strain. (i) Evolution of electronic structures of FM-z $MnBi_2Te_4$ under hydrostatic pressure. Panel (a)-(f) are taken from [14], panel (g)-(h) from [17], and panel (i) from [18].

resulting in double degeneracy of bands. On the other hand, odd layers (Fig. 1.12(c)) have P_2 but lack both Θ and $P_2\Theta$ symmetries, resulting in spin-split bands. The distinct symmetries between even and odd layers lead to different topological properties. In even layers with $P_2\Theta$ symmetry, a topological Chern number C=0 is required, whereas C$\neq$ 0 is permitted in odd layers. Specifically, a QAH insulator state with C=1 was observed in 5 SLs, characterized by quantized Hall conductance and vanishing longitudinal conductance, in the absence of external magnetic field (Fig. 1.12(d))[15] and under a moderate magnetic field [45, 15, 46], while an axion insulator state with C=0 was observed in 6 SLs, characterized by a zero Hall conductance plateau and a large longitudinal resistance (Fig. 1.12(f))

[16]. Additionally, by applying an out-of-plane magnetic field (B > 6T) to the 6SL sample, an axion insulator to Chern insulator (IQH insulator without Landau levels) topological phase transition was realized (Fig. 1.12(f))[16]. Moreover, high-Chern-number states (C = 2, 3) characterized by a ne^2/h Hall conductance was also observed in thin flim limits of $MnBi_2Te_4$ under a magnetic field along c-axis [46, 47]. However, discrepency remains in these experimental studies on the topological states of thin flim $MnBi_2Te_4$, which may be attributed to subtle variations in material growth and fabrication techniques, as well as the diverse possibilities of realizing different types of topological states. Future studies on thin film $MnBi_2Te_4$ with extreme caution are needed to advance our understanding of its topological properties and potentially unlock its potential for practical applications.

By applying an out-of-plane magnetic field to the bulk $MnBi_2Te_4$ (Fig. 1.12(g)), an ideal Weyl semimetal phase can be stabilized in the field-induced FM sate. Fig. 1.12(h) displays the electronic structures near the type-II Weyl nodes calculated by DFT, while Fig. 1.12(i) shows the Fermi arc connecting the Weyl nodes. Moreover, the electronic structures near the Weyl crossings are highly susceptible to external factors such as strain, magnetic field angle, and pressure. A possible Lifshitz transition from a type-II to a type-I Weyl semimetal was proposed by varying the orientations of the magnetic moments or applying strain, as Fig. 1.13(a)-(h) demonstrates. It is proposed that the tilting of the Weyl cones will also rotate from a type-II to type-I WSM as the magnetic orientation rotates from out-of-plane to in-plane (Fig. 1.13(b)), with the pair of Weyl nodes eventually annihilating with each other when the magnetic orientation becomes fully in-plane. Isotropic strain has also been reported to be able to tune a type-II WSM phase in FM-z $MnBi_2Te_4$ into a type-I WSM (Fig. 1.13(g)-(h)). Under a hydrostatic pressure, FM-z $MnBi_2Te_4$ is predicted to undergo a series of topological phase transitions. The type-II Weyl nodes under ambient pressure will first move towards each other and annihilate at a pressure $\sim$ 2 GPa. Meanwhile, a new pair of type-I Weyl points emerges at around 1 GPa. With increasing pressure, the dispersion of the type-I Weyl cones starts to tilt and eventually turns into type-II Weyl cones near 5 GPa. However, the electronic structures of $MnBi_2Te_4$ are highly sensitive to its magnetism and details in real materials, such as lattice constants, defect types and densities, and the correlation strength. As a result, it is uncertain whether the real system

will behave as predicted by DFT calculations. The focus of this thesis is to use vairous experimental probes to systematically investigate the ideal Weyl semimetal phase and its associated Lifshitz transitions under external fields. This will help uncover the truth about the WSM state in $MnBi_2Te_4$ and pave the way for future studies on magnetic topological materials.

While the topological phases introduced above have attracted extensive studies, there are still a number of other phases proposed in theory that have yet to be observed due to experimental challenges. For instance, an AFM mirror topological crystalline insulator has been proposed in the AFM-x state, where the magnetic moments lie in-plane [14]. Although this magnetic state is difficult to achieve in $MnBi_2Te_4$, it might be feasible in compounds based on Eu, Ni, or V. Additionally, Majorana hinge modes have been proposed in $MnBi_2Te_4$/superconductor heterostructures through the proximity effect [48]. A range of higher order TIs have also been proposed in $MnBi_2Te_4$ and related systems. For example, a hypothetical higher-order Mobius insulator has been proposed in the canted AFM state, characterized by a Mobius twist in its topological surface state [49]. Further investigation is needed to explore these phases.

Chapter 2

EXPERIMENTAL METHOD

This chapter will begin by discussing the details of the crystal growth procedures developed for $MnBi_{2-x}Sb_xTe_4$. It will then provide an overview of the experimental measurements featured in this thesis, including electrical transport and magnetic properties measurements conducted under high magnetic fields and hydrostatic pressure on $MnBi_{2-x}Sb_xTe_4$.

2.1 Crystal growths

Single crystals of $MnBi_{2-x}Sb_xTe_4$ were grown by a flux method. Mixtures of arc-melted Mn (alfa aesar, 99.9998%), Bi granules (strem, 99.9999%), Sb shot (alfa aesar, 99.9999%), and Te lump (alfa aesar, 99.9999%) in the molar ratio of $1 : 10 \times (2 - x) : 10x : 16$ (Mn:Bi:Sb:Te) were grinded and placed in a Canfield crucible, and sealed inside a quartz tube under high vacuum (< 10 mTorr). The quartz tube and crucibles were pre-cleaned using oxygen plasma followed by deionized water using an ultrasonic cleaner and baked at 180°C overnight. The tube loaded with charge was then heated to 900°C and held for 12 hours. After slowly cooling across a ∼10°C window around 600°C over a week, the excess flux was quickly removed by centrifugation above the melting temperature of Bi_2Te_3 (585°C). For the Sb-heavy compound, the decanting temperature is near 600°C, whereas for the Bi-heavy compound, the optimum decanting temperature is near 593°C. The exact optimal decanting temperature depends on the real temperature and thermal gradient inside the furnaces. Crystals produced by this self-flux method were typically in the size of 1mm × 5mm × 5mm (Fig. 2.2(a)). The compositions were determined by Energy-dispersive X-ray spectroscopy (EDS) on a cleaved surface using a Sirion XL30 scanning electron microscope. Measurements were made at several locations on multiple samples within one batch. As shown in Fig. 2.1, measured values were proportional to the nominal composition in all cases. Small deviations observed in the data were likely due to the application of different

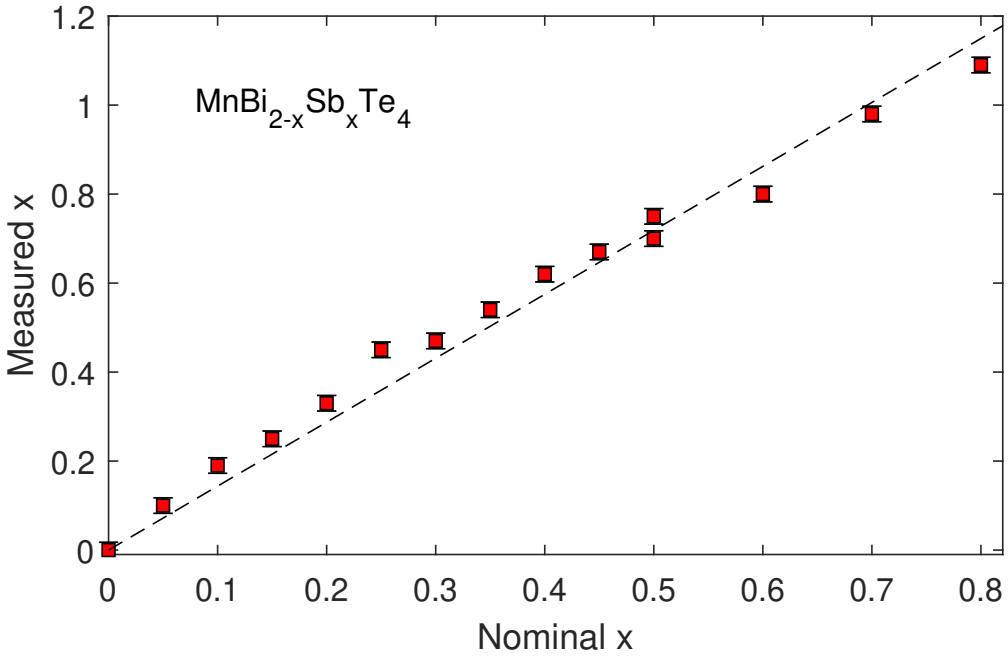

Figure 2.1: **Summary of growths of $MnBi_{2-x}Sb_xTe_4$.** The Sb concentration determined by EDS verses the nominal composition. The changes in slope observed in the data were likely due to the application of different decanting temperatures, particularly around nominal x = 0.25 and 0.5.

decanting temperatures as mentioned before, particularly around nominal x = 0.25 and 0.5.

2.2 Electrical transport measurements

Electrical transport measurements were made in a standard four-probe or six-probe contact configuration with current direction in-plane and voltage contacts on the exposed [001] surface. Magnetotransport measurements were carried out in a 14 T Physical Property Measurement System (PPMS), a 36 T series connected hybrid magnet, a 31T resistive magnet at the National High Magnetic Field Laboratory (NHMFL) in Tallahassee, FL, or a 65T pulsed magnetic field at NHMFL in Los Alamos, NM. The magnetic field is out-of-plane along c-axis of the crystal if not otherwise noted. For angle-dependent magnetotransport measurements, the magnetic field rotates from out of plane to inplne perpendicular to the

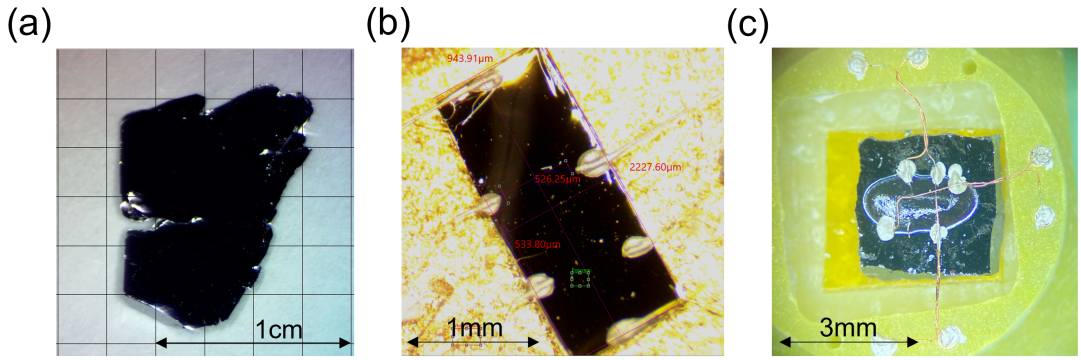

Figure 2.2: **Single crystal and samples of $MnBi_{2-x}Sb_xTe_4$.** (a) Single crystal of $MnBi_{2-x}Sb_xTe_4$ (x = 0.75). (b) a sample of $MnBi_{2-x}Sb_xTe_4$ (x=0.7) with six-probe contacts for magnetotransport measurement under a DC magnetic field (c) a six-probe $MnBi_{2-x}Sb_xTe_4$ sample glued on an intrinsic silicon substrate with stycast epoxy mounted on a puck for magnetotransport measurement under a pulsed magnetic field.

current direction. To eliminate any effects from contact misalignment, the magnetoresistivities and Hall resistivities were symmetrized and antisymmetrized, respectively.

For magnetotransport measurements under a DC field (up to 36T), samples were prepared in a standard way - a bar-shaped (typically 1mm $\times$ 400 μm $\times$ 30μm) sample was prepared (Fig. 2.2(b)). Electrical contacts were made to the sample by first sputtering the contact pattern with gold using a hand-made paper mask and gold sputterer with argon atmosphere (108 Manual Sputter Coater, Cressington Scientific Instruments). Electrical leads in the form of 25-micron diameter gold wire were attached to the pre-patterned contacts by hand using silver paste. For high field (31T and 36T) measurements, a thin layer of two-part epoxy was applied over the samples to secure the samples under high magnetic field sweeps. For magnetotransport measurements under a pulsed magnetic field (65T), samples were glued down on an intrinsic silicon substrate ($\sim 3mm \times 3mm \times 0.5mm$) with stycast epoxy (Loctite Stycast 2850FT) (Fig. 2.2(c)). The electrical leads are made of twisted pairs of 50 gauge wires. The twisted pairs were arranged in a way to minimize the current loop area and anchored down to the puck with varnish (GE 7031).

2.3 Magnetic properties measurements

The low field magnetization was measured using the vibrating sample magnetometer (VSM) module of a 14 T PPMS. To prepare the sample, a small amount of GE varnish was used to glue it onto a quartz rod, which was then placed in a brass sample holder. The magnetization data were reported in Bohr magnetons per Mn (μB/Mn), which was calculated using the weight of the sample and the EDS-determined stoichiometry.

High-field magnetization measurements were conducted using an extraction magnetometer in a 65 T pulsed magnet at the Pulsed-Field Facility of the NHMFL located at Los Alamos National Laboratory. The extraction magnetometer was a homemade device consisting of a 1.5-mm-bore, 1.5-mm long, 1500-turn compensated coil susceptometer made from 50-gauge high-purity copper wire. To ensure a sizable magnetization signal, multiple samples were glued along the c-axis using two-part epoxy and mounted within a 1.3-mm-diameter ampoule that could be moved in and out of the coil. When a sample was placed inside the coil, the varying magnetization signal V (dM/dt) over time t was induced by the dB/dt of the pulsed magnet. To obtain the sample magnetization, the empty coil data measured without the sample was subtracted from the data measured under identical conditions with the sample present, and then integrated over time. The resulting data were normalized using independent low-field magnetization data to obtain the absolute value in Bohr magnetons per Mn (μB/Mn).

2.4 Application of pressure

To investigate the effect of hydrostatic pressure on the magnetotransport of our sample, we applied pressures of up to 2.2 GPa using a clamp piston cylinder pressure cell (easyLab Pcell 30) while conducting magnetotransport measurements in the 14T PPMS. Fig. 2.3(a) provides a photograph of the pressure cell used in the experiment. A six-probe sample, similar to that shown in Fig. 2.2(b), was prepared, and its magnetotransport was initially measured under ambient pressure. The sample was then placed onto the sample mounting stage of the pressure cell (Fig. 2.3(b)), and the magnetotransport was measured at fixed pressure at a time and at multiple pressure setpoints in ascending order. To monitor

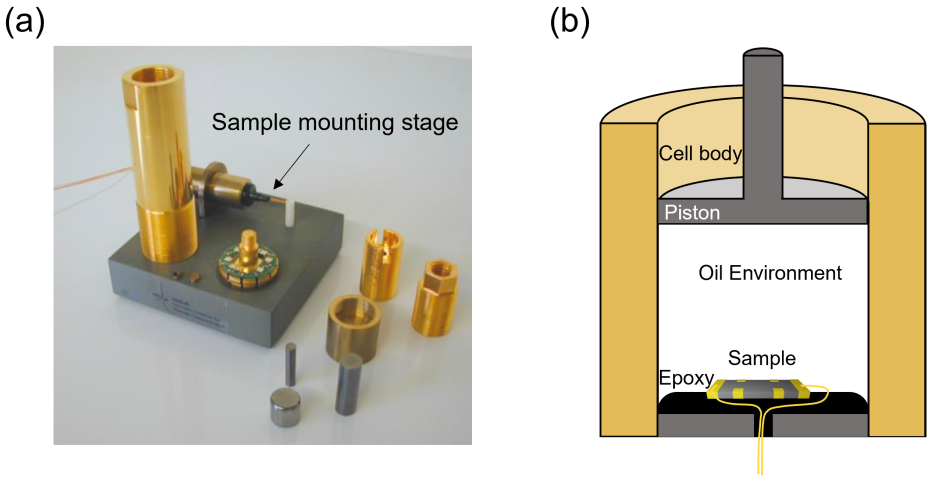

Figure 2.3: **Experimental setup for electrical transport measurements under pressure** (a) photograph of the pressure cell (b) schematic of the inside of the pressure cell

the applied pressure, we used a Sn piece as a manometer by tracking its superconducting transition as a function of pressure.

2.5 Phase diagram

The parent compound $MnBi_2Te_4$ is the first intrinsic magnetic topological material. Its crystal structure, as shown in Fig. 2.4(a), can be seen as a natural heterostructure of magnetic MnTe inserted in the TI Bi_2Te_3. The ground state of $MnBi_2Te_4$ is an A-type AFM TI with an easy axis along c and Neel temperature T_N at 24K. By applying an out-of-plane magnetic field, the AFM phase undergoes a metamagnetic transition, and an FM phase is stabilized near 8T.

Substitute Bi with Sb ($MnBi_{2-x}Sb_xTe_4$) tunes the carrier from electron to hole across the charge neutrality point while preserving the intrinsic magnetism (19 K $< T_N <$ 24 K). Figure 2.4(b) shows the temperature dependence of the zero-field in-plane electrical resistivity ρ_{xx}. For most samples, the resistivity exhibits a metallic behavior, consistent with a degenerately doped semiconductor. For one composition very close to the charge-neutrality point (x = 0.7), the resistivity shows a nonmonotonic temperature dependence.

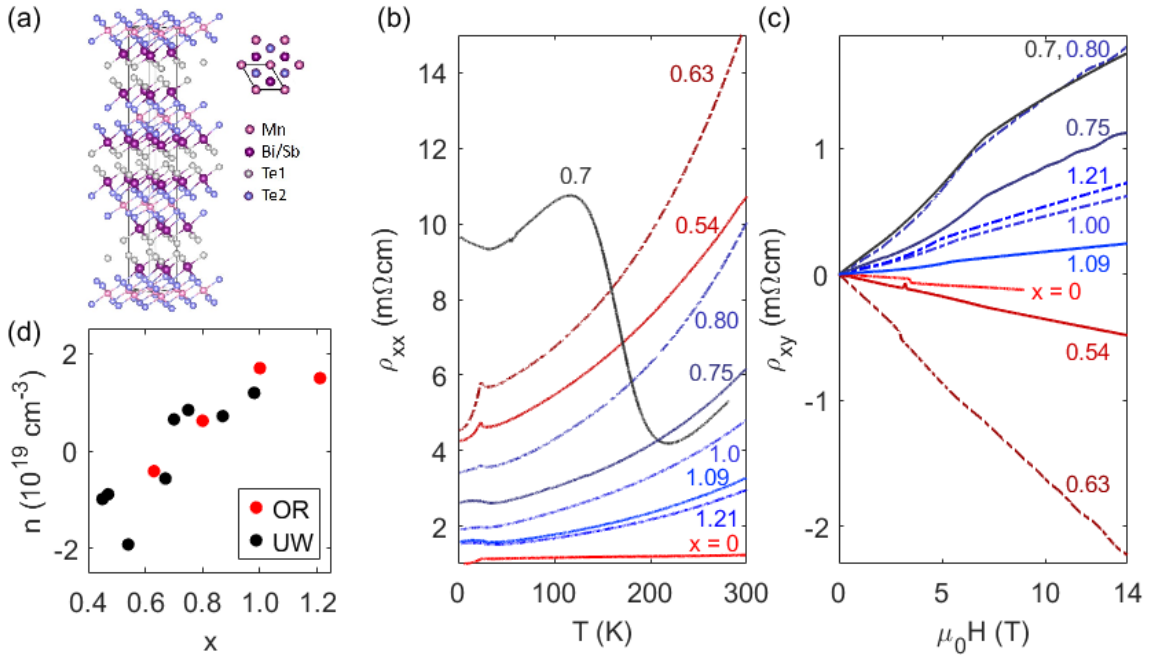

Figure 2.4: **Transport characterization of $MnBi_{2-x}Sb_xTe_4$.** (a) Crystal structure of $MnBi_{2-x}Sb_xTe_4$. (b) Temperature dependence of zero-field in-plane resistivity ρ_{xx}. (c) Field dependence of Hall resistivity ρ_{xy} with field along the c-axis at T = 2K. Dash-dotted lines denote data taken on Oak Ridge (OR) samples, while solid lines represent UW samples. (d) Carrier density as a function of chemical doping x. Carrier density is extracted by fitting the linear background of the Hall resistivity above H_{c2}.

A kink in the resistivity at around 23–25 K marks the AFM transition temperature T_N. Fig. 2.4(c) shows the Hall resistivity ρ_{xy} measured at T = 2 K. The carrier density is extracted by fitting the linear background of the Hall resistivity above H_{c2}. As shown in 2.4(d), the carrier density changes from 6×10^{19} cm^{-3} electrons to 2×10^{19} cm^{-3} holes as the Sb concentration increases, and the system switches from n-type to p-type at a compensation point in the vicinity of x $\sim$ 0.7.

Figure 2.5 shows the magnetization measurement of a representative sample, x = 0.63. As shown in Fig. 2.5(a), when the magnetic field is swept along the c-axis at low temperatures, the sample undergoes an AFM to canted AFM transition, corresponding to the sudden jump of the magnetization at the spin-flop field H_{c1}, followed by a canted AFM to FM transition at the saturation field H_{c2}. Using the magnetization versus field data, we

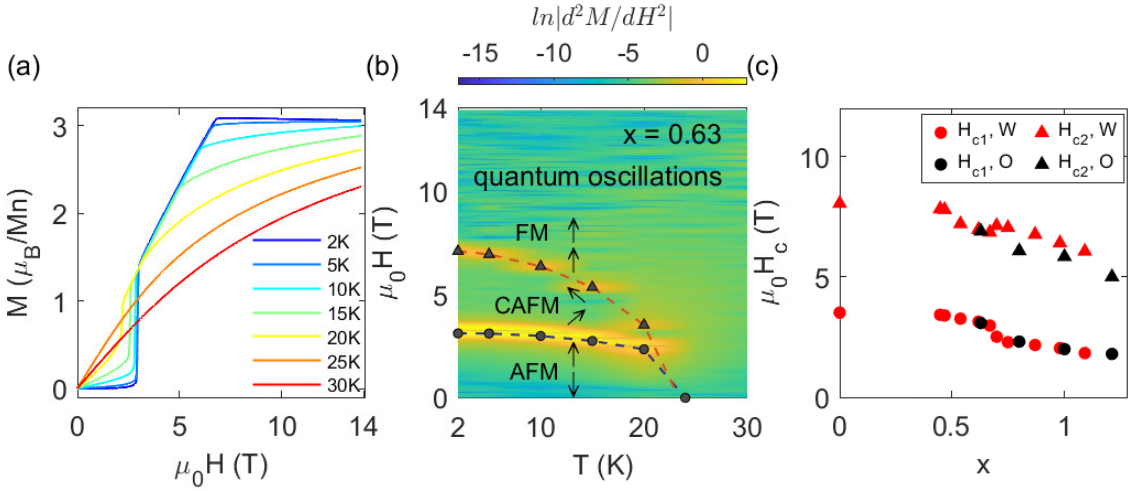

Figure 2.5: **Magnetization characterization of $MnBi_{2-x}Sb_xTe_4$.** (a) Field dependence of magnetization of the $x = 0.63$ OR sample measured at various temperatures. (b) Field-temperature magnetic phase diagram of $MnBi_{2-x}Sb_xTe_4$ for $x = 0.63$. Circles and triangles denote spin-flop field H_{c1} and saturation field H_{c2}, respectively. Dotted lines are guides for the eyes for the phase boundaries. Color in the phase diagrams maps to the logarithm of the absolute value of the second derivative of magnetization with respect to the field. Note: the temperature range is 2–30 K. (c) Doping dependence of spin-flop field H_{c1} (circles) and saturation field H_{c2} (triangles) at 2 K. Red data are taken on UW samples, whereas black data are taken on OR samples.

constructed the magnetic phase diagram for x = 0.63, shown in Fig. 2.5(b). The sharp color changes highlighted in the second derivative of magnetization with respect to the field in a log scale mark the phase boundaries defined by H_{c1} (circles) and H_{c2} (triangles). As the temperature increases, the FM phase eventually crosses over to the paramagnetic (PM) phase. Within the range of the doping focused on in our study, the substitution of Sb only slightly suppresses T_N, H_{c1}, and H_{c2}, without altering the magnetic phase behavior [50].

Chapter 3

ELECTRONIC STRUCTURES PROBED BY QUANTUM OSCILLATIONS IN THE FIELD-INDUCED FERROMAGNETIC STATE OF $MnBi_{2-x}Sb_xTE_4$

3.1 Abstract

The intrinsic antiferromagnetic topological insulator $MnBi_2Te_4$ undergoes a metamagnetic transition in a c-axis magnetic field. It has been predicted that FM $MnBi_2Te_4$ is an ideal Weyl semimetal with a single pair of Weyl nodes. In this chapter, I present measurements of quantum oscillations detected in the field-induced FM phase of $MnBi_{2-x}Sb_xTe_4$, where Sb substitution tunes the majority carriers from electrons to holes. Single-frequency Shubnikov-de Haas oscillations were observed in a wide range of Sb concentrations ($0.54 \leq x \leq 1.21$). The evolution of the oscillation frequency and the effective mass shows reasonable agreement with the Weyl semimetal band structure of FM $MnBi_2Te_4$ predicted by density functional calculations. Intriguingly, the quantum oscillation frequency shows a strong temperature dependence, indicating that the electronic structure depends sensitively on magnetism.

3.2 Introduction

The recently discovered magnetic topological material $MnBi_2Te_4$ presents a unique platform to study band topology intertwined with magnetic order[14, 17, 51, 52]. The crystal structure of $MnBi_2Te_4$ (Fig. 2.4(a)) consists of van der Waals bonded septuple layers. Each of the septuple layers can be viewed as a natural heterostructure of a magnetic MnTe layer sandwiched by Bi_2Te_3 TIs. The layered structure enables exfoliation to reach the regime of a two-dimensional phenomenon. For example, the quantum anomalous Hall effect has been observed in atomically thin flakes [16, 15, 53, 45]. The ground state of bulk $MnBi_2Te_4$ is a layered antiferromagnet (AFM) ($T_N = 24$ K), in which the individually ferromagnetic Mn-Te layers are coupled antiferromagnetically in the out-of-plane direction (the c-axis),

which is also the easy-axis of the moments. Density functional theory (DFT) calculations indicate that the three-dimensional bulk electronic structure in the AFM phase is an antiferromagnetic TI, with an insulating bulk and gapped surface state on the top and bottom surfaces. Although soon after the material realization, ARPES studies of $MnBi_2Te_4$ revealed the Dirac surface states predicted by the theory [54, 55, 56, 57, 58, 59], controversy remains as to whether the Dirac point is gapped as expected [60].

When a magnetic field is applied along the c-axis, the AFM phase undergoes a metamagnetic transition, and an FM phase is stabilized at 8 T. Compared with the antiferromagnetic phase, the electronic structure in the field-induced FM phase is much less explored. This is partly because the magnetic field and ARPES measurements are incompatible. It has been predicted that the electronic structure in the FM phase of $MnBi_2Te_4$ is an ideal type-II Weyl semimetal, with a single pair of Weyl nodes that is situated on the k_z axis [14, 17]. If so, the metamagnetic transition is also a field-induced topological phase transition. Recent scanning tunneling spectroscopy (STS) measurements found that the local density of states is almost unchanged across the AFM-FM transition [61, 62], inconsistent with a topological phase transition. However, STS only probes the surface. Clearly, a direct measurement of the bulk electronic structure of FM $MnBi_2Te_4$ is desirable to resolve this issue.

Sb-substituted $MnBi_2Te_4$ ($MnBi_{2-x}Sb_xTe_4$) offers the opportunity to study the electronic structure in the FM phase via quantum oscillation measurements. The Sb substitution effectively tunes the carriers from electrons to holes while preserving their intrinsic magnetism ($19 < T_N < 24$ K) [58, 50]. Close to the charge-neutrality point, the mobility is enhanced, and quantum oscillations have been observed [63]. The measurement of quantum oscillations has been a canonical method to probe the bulk electronic structures of metals and semiconductors. In particular, the doping dependence of the oscillation frequency and effective mass provides strong constraints on the band dispersion near the band edge.

In this chapter, I present measurements of the Shubnikov-de Haas (SdH) oscillations in the field-induced FM phase of $MnBi_{2-x}Sb_xTe_4$ over a wide range of Sb concentrations ($0.54 \leq x \leq 1.21$). By comparing the measured oscillation frequency, carrier density, and effective mass with DFT calculations, we find overall reasonable agreement with calculations assuming a rigid band shift of the Weyl semimetal band structure in FM $MnBi_2Te_4$.

Interestingly, the oscillation frequency shows a strong temperature dependence. We can explain this unusual phenomenon as a manifestation of the high sensitivity of the electronic structure to the size of the magnetization in this material.

3.3 Results

Shubnikov–de Haas (SdH) oscillations were observed in the transverse magnetoresistance of $MnBi_{2-x}Sb_xTe_4$. Figure 3.1 shows the in-plane longitudinal resistivity ρ_{xx} as a function of c-axis magnetic field. The magnetoresistance (MR) exhibits a strong field dependence. At base temperature, two successive features can be seen in most samples, corresponding to H_{c1} and H_{c2}. As the temperature increases, the two anomalies merge and eventually smear out above T_N. For all the doping levels shown in the figure, quantum oscillations can be seen once the field surpasses H_{c2}. In Fig. 3.2, the oscillatory part of the resistivity is plotted against the inverse of the magnetic field. The oscillatory part was extracted by subtracting a fifth-order polynomial background. Using a fast Fourier transform (FFT), we obtained the frequency spectrum for each doping level, plotted in Fig. 3.3. The oscillation frequency, defined as the peak position in the FFT spectrum at base temperature, is plotted as a function of composition in Fig. 3.3(l). Starting from the electron-doped side, the oscillation frequency decreases as x increases and reaches 82 T for $x = 0.63$. After crossing the compensation point, the frequency increases monotonically from 37 to 144 T as x increases from 0.7 to 1.21.

The quantum oscillation frequency is related to the extremal area of the Fermi surface cross-section (A) projected along the field direction via the Onsager relation $F_s = (\hbar/2\pi e)A$. The compositional dependence of the frequency (Fig. 3.3(l)) is consistent with the shrinking and expanding of the Fermi surface as the system is tuned across the charge neutrality point. Notice that for a three-dimensional Fermi surface, the full angular dependence of the frequency is required to determine the carrier density from its volume. Such a three-dimensional mapping is impossible for $MnBi_{2-x}Sb_xTe_4$ because the rotation of the magnetic field also changes the direction of magnetization, which inevitably changes the electronic structure [64]. In this subsection, we focus on the electronic structure when the magnetization is aligned to the c-axis by the magnetic field. The angle dependence of the quantum

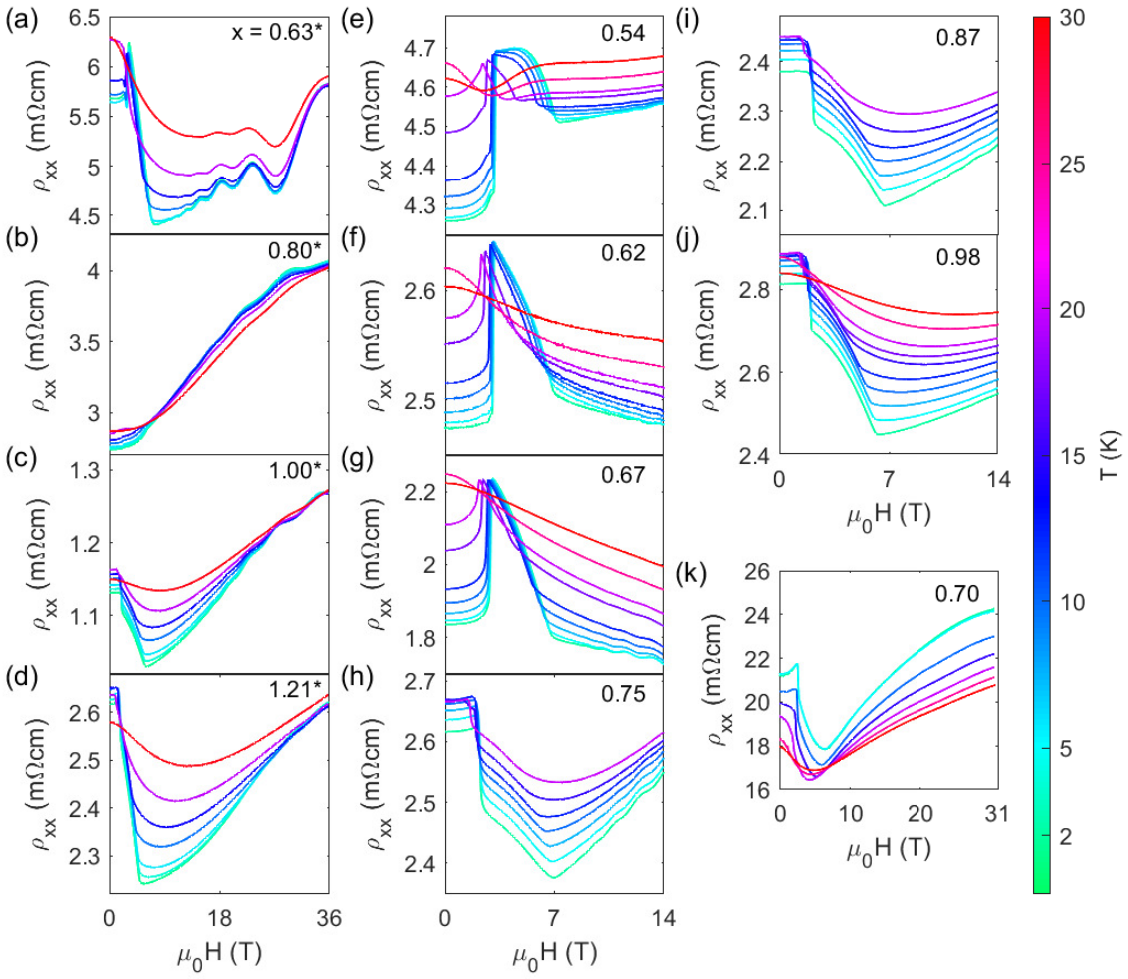

Figure 3.1: **Magnetoresistivity of $MnBi_{2-x}Sb_xTe_4$.** Field dependence of ρ_{xx} for $MnBi_{2-x}Sb_xTe_4$ with c-axis magnetic fields up to 36 T [OR samples (a)-(d)], 14 T [UW samples (e)-(j)], and 31T [UW sample (k)]. The temperature of the measurements is color-coded based on the scale bar on the right.

oscillations will be discussed in detail in Chapter 5.

We next turn to the temperature dependence of the quantum oscillations. As usual, we proceed to determine the effective mass $m = m^* m_e$ by fitting the temperature dependence

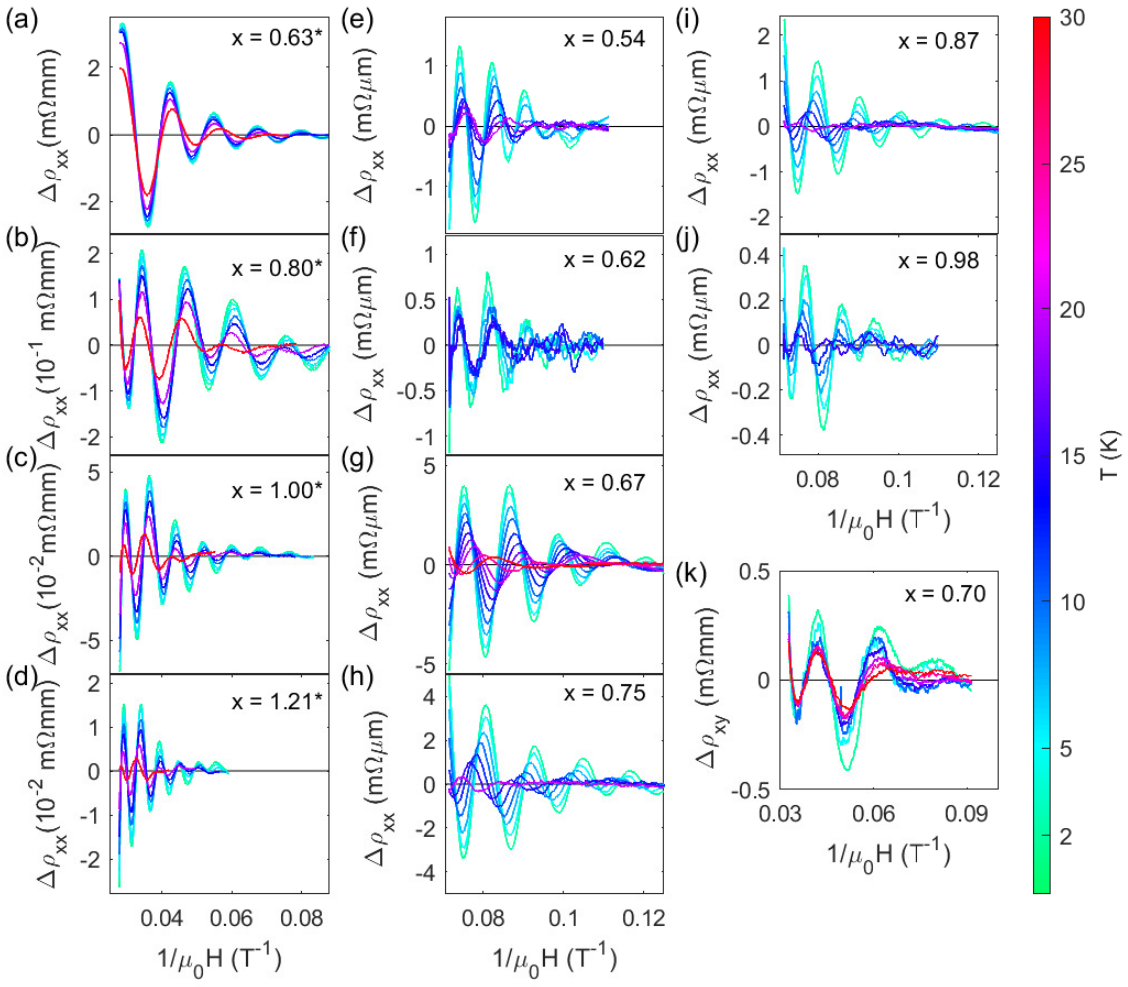

Figure 3.2: **Shubnikov-de Haas oscillations of $MnBi_{2-x}Sb_xTe_4$.** Oscillatory part of ρ_{xx} for $MnBi_{2-x}Sb_xTe_4$ as a function of inverse field obtained by subtracting a fifth-order polynomial background.

of the amplitude of oscillations to the Lifshitz-Kosevich factor,

$$R_T = \frac{\alpha T m^*}{B sinh(\alpha T m^*/B)} \tag{3.1}$$

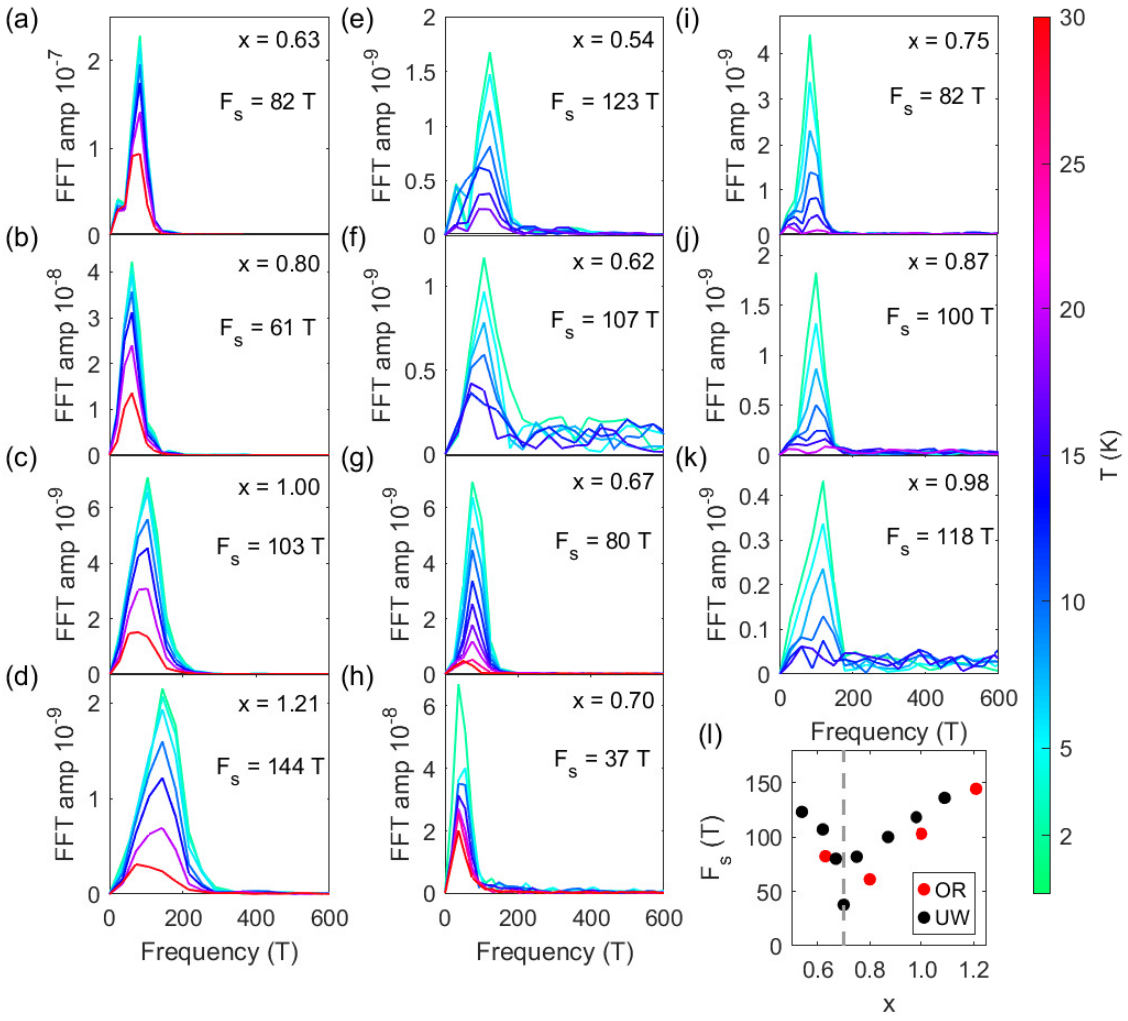

Figure 3.3: **Fast Fourier transform (FFT) spectrum and oscillation frequency of $MnBi_{2-x}Sb_xTe_4$.** (a)–(k) FFT spectrum of the oscillatory part of resistivity for $MnBi_{2-x}Sb_xTe_4$ at various temperatures. (l) Doping dependence of the peak frequency F_S. Red (black) dots are data taken from OR (UW) samples. The gray dashed line denotes the doping level closest to the charge-neutral point.

where $\alpha = 2\pi^2 k_B m_e/e\hbar$. We determine the amplitude by taking the difference between the peak and valley resistances measured at the highest field, where the magnetization is in the

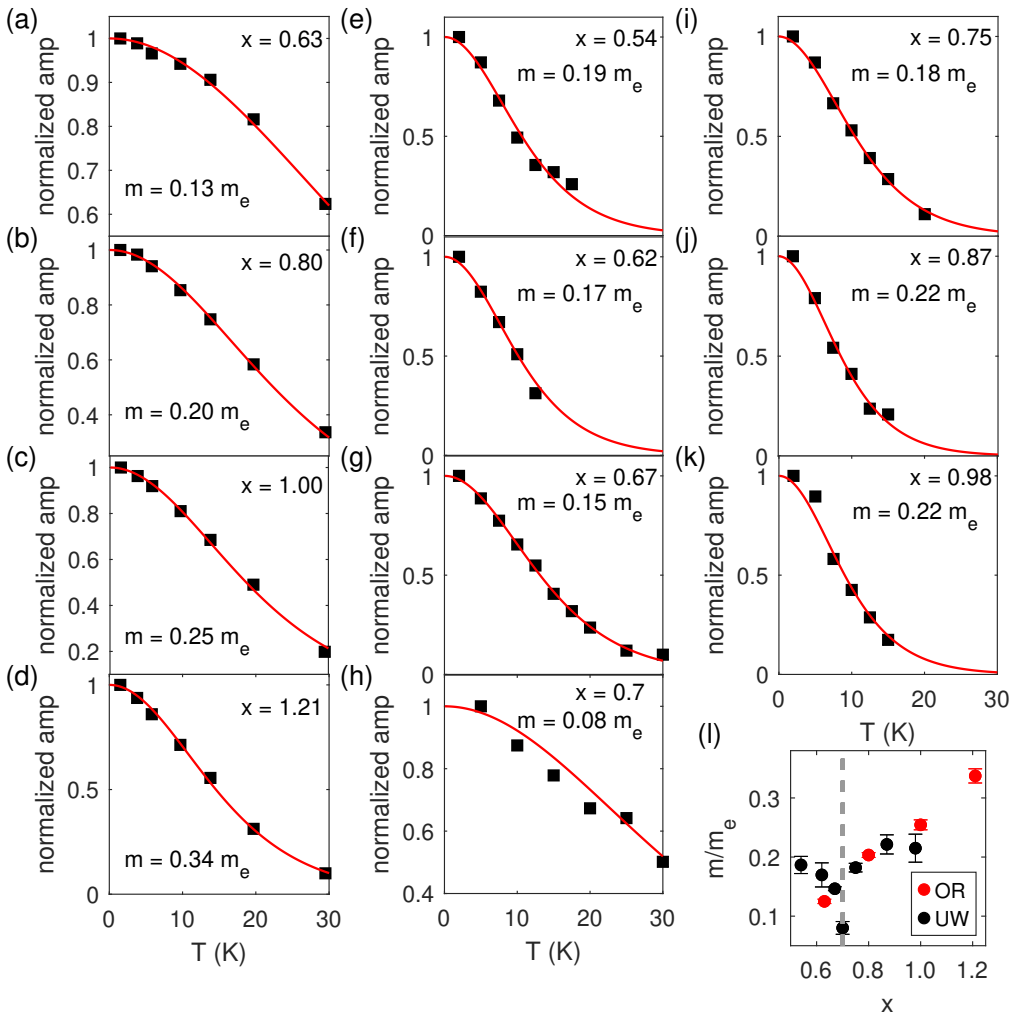

Figure 3.4: **Effective mass m/m_e of $MnBi_{2-x}Sb_xTe_4$ extracted from Lifshitz-Kosevich fitting.** (a)–(k) Temperature dependence of the oscillation amplitude measured near 36 T [(a)–(d) OR samples], 14 T [(e)–(g),(i)–(k) UW samples], and 31 T [(h) UW sample]. Red solid curves are fits to the Lifshitz-Kosevich factor to obtain the effective mass. (l) Doping dependence of the effective mass for OR samples (red) and UW samples (black). The gray dashed line denotes the doping level closest to the charge neutrality point.

saturation state. As shown in Fig. 3.4, the temperature dependence is well fitted by the thermal damping factor R_T in all cases. The extracted effective mass shows a strong doping

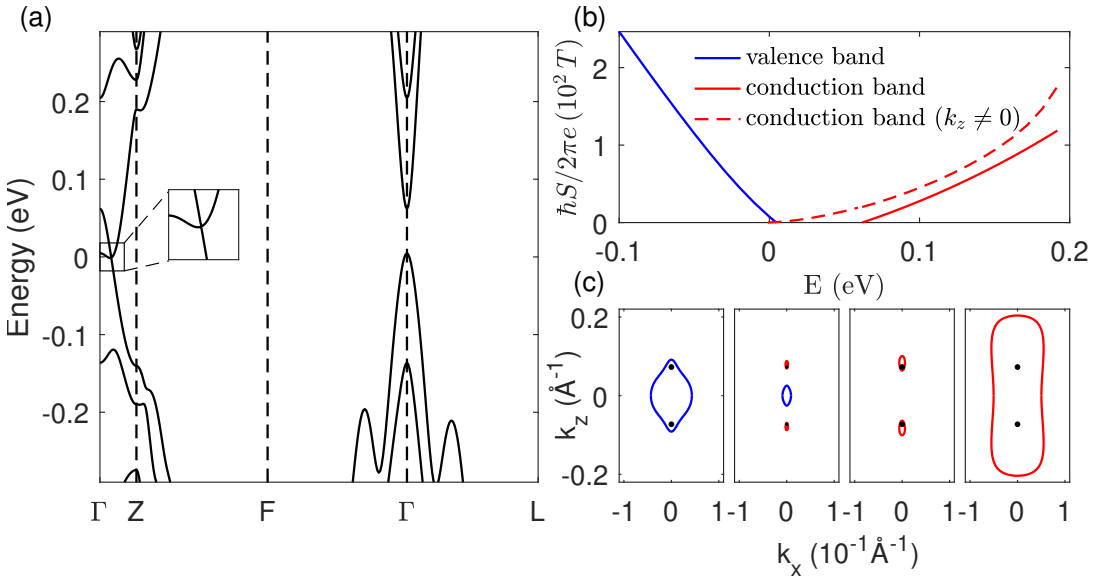

Figure 3.5: **Density functional theory calculations** (a) Band structure of $MnBi_2Te_4$ in the FM state with magnetic moments saturated along the c-axis calculated by DFT. (b) Calculated oscillation frequency vs Fermi energy for the electron (red) and hole (blue) pocket. The electron pocket has two extremal orbits. The dashed (solid) line represents the $k_z \neq 0$ ($k_z = 0$) extremal orbit. (c) Evolution of the Fermi surface projected onto the $k_x - k_z$ plane passing from heavily electron-doped (rightmost panel) to heavily hole-doped (leftmost panel).

dependence [Fig. 3.4(l)], indicating that the energy bands are non-parabolic.

To gain further insights, we used DFT to calculate the band structure of FM $MnBi_2Te_4$ with the magnetization fully saturated along the c-axis [Fig. 3.5(a)]. We obtain a Weyl crossing along the $\Gamma - Z$ direction, consistent with previous studies. The frequencies corresponding to the extremal orbits are plotted in Fig. 3.5(b) as a function of Fermi energy. The evolution of Fermi surface projections onto the $k_y = 0$ plane as the Fermi level moves is illustrated in Fig. 3.5(c).

We then compare the experimentally measured constraints on the electronic structures with theoretically calculated results. The effective mass, m, is the derivative of the cyclotron orbit area A with respect to energy, E:

$$m = \frac{\hbar^2}{2\pi}\frac{\partial A}{\partial E} \tag{3.2}$$

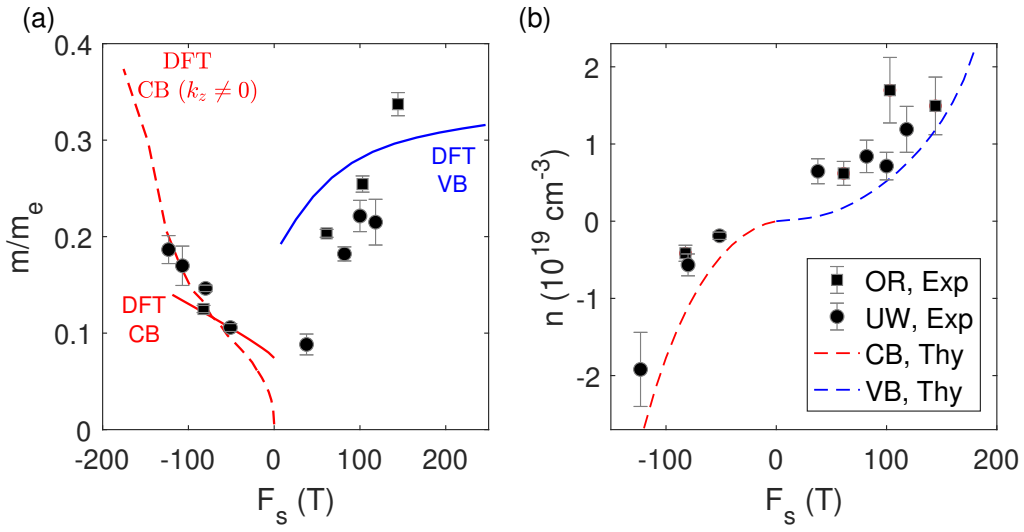

Figure 3.6: **Comparison between experiment and theory.** Theoretical predictions (dashed lines) and experimental measurements of the effective mass (a) and carrier density (b) as a function of quantum oscillation frequency. Circles are for UW samples, and squares are for OR samples. In both (a) and (b), red lines represent calculations for the conduction band, and blue lines are calculations for the valence band. In (a), the red dashed line is the calculations for the $k_z \neq 0$ extremal orbit of the conduction band, while the red solid line is for the $k_z = 0$ orbit of the conduction band

The effective mass m as a function of A is determined by the band dispersion E(k), and A is in turn directly related to the oscillation frequency F_S via the Onsager relation, $F_s = (\hbar/2\pi e)A$. Therefore, the experimentally measured variation of m with respect to F_s provides strong constraints on the underlying band dispersion. In Fig. 3.6(a), the measured effective mass versus oscillation frequency is plotted alongside the prediction based on the Weyl dispersion (blue and red curves) calculated by DFT. The Weyl dispersion shows a good agreement with the experimental values. In particular, the calculated values of the effective mass of the conduction band match almost perfectly with the experimental data, and the valence-band effective mass also falls within the range of measured values, although the experimental doping dependence seems somewhat stronger. We also calculated the carrier density (from the Fermi surface volume) versus oscillation frequency from the Weyl band structures, and it too shows good agreement with the experimental data (Fig. 3.6(b)). To

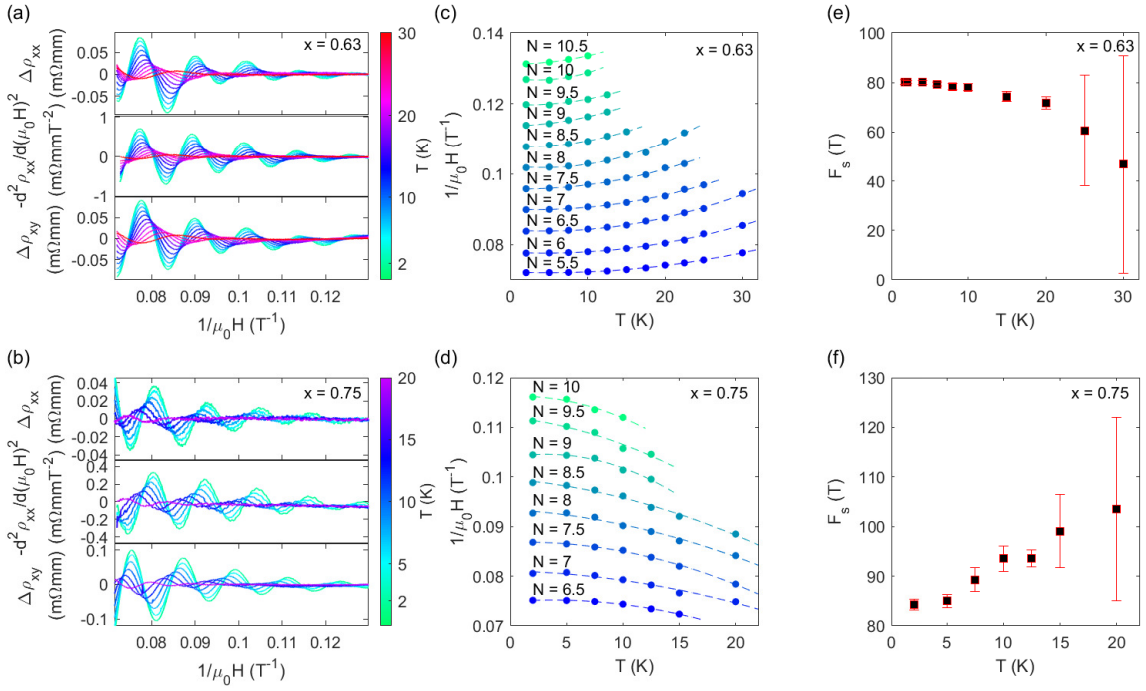

Figure 3.7: **Anomalous temperature dependence of SdH oscillations of $MnBi_{2-x}Sb_xTe_4$.** (a),(b) Oscillatory part of ρ_{xx} , second derivative of ρ_{xx}, and background subtracted ρ_{xy} for (a) electron-doped (x = 0.63) and (b) hole-doped (x = 0.75) $MnBi_{2-x}Sb_xTe_4$ at varied temperatures as a function of inverse field $1/\mu_0 H$. (c),(d) Temperature dependence of peak and valley positions in the SdH oscillations for (c) x = 0.63 and (d) x = 0.75. (e),(f) Oscillation frequency F_S as a function of temperature for (e) electron-doped (x = 0.63) and (f) hole-doped (x = 0.75) $MnBi_{2-x}Sb_xTe_4$.

conclude, The evolution of the oscillation frequency and the effective mass shows reasonable agreement with the Weyl semimetal band structure of FM $MnBi_2Te_4$ predicted by density functional calculations.

3.4 Discussion

3.4.1 Anomalous temperature dependence of SdH oscillation frequencies

The amplitude of quantum oscillations always decays with temperatures due to the smearing of the Fermi-Dirac distribution, but the frequency is usually a constant as a function of temperature. Surprisingly, here, in addition to the thermal damping, we also observed substantial shifts of the peak and valley positions (Fig. 3.2) as temperature increased. A closer inspection of the FFT spectra (Fig. 3.3) shows that the oscillation frequency also shifts with temperature. To ensure that this shift is not an artifact due to background subtraction, we extracted the oscillatory data of two representative samples, $x = 0.63$ (electron-doped) and $x = 0.75$ (hole-doped), using three different methods: background subtracted ρ_{xx}, second derivative of ρ_{xx} with respect to H, and background subtracted Hall resistivity ρ_{xy}. The results shown in Figs. 3.7(a) and 3.7(b) all exhibit the same clear shifts of the peak and valley positions, which are plotted in Figs. 3.7(c) and 3.7(d). From these, we obtained the oscillation frequency by extracting the period in the inverse field, which is plotted versus temperature in Figs. 3.7(e) and 3.7(f). Interestingly, as the temperature increases, the electron-doped sample ($x = 0.63$) shows a decrease in frequency whereas the hole-doped sample ($x = 0.75$) shows an increase.

In the standard theory, the frequency of quantum oscillations reflects the area of the Fermi surface. The Fermi surface may change in principle if the Fermi energy shifts with temperature due to an asymmetric density of states, but such a shift is usually very small. In the cases of Dirac or Weyl semimetals, energy-dependent cyclotron mass also leads to a frequency shift as the temperature changes [28]. However, the temperature dependence of the oscillation frequency that we observed in $MnBi_{2-x}Sb_xTe_4$ is orders of magnitude larger than the effect caused by band curvature. Hence, such a significant change in frequency suggests instead a modification of the energy bands connected to the temperature-dependent magnetic order. As the temperature increases, the field-induced magnetization decreases due to thermal fluctuations, and the size of the Fermi surface changes accordingly. The opposite trend in electron-doped and hole-doped samples indicates that both the conduction and valence bands move upward in energy as the temperature increases so that the

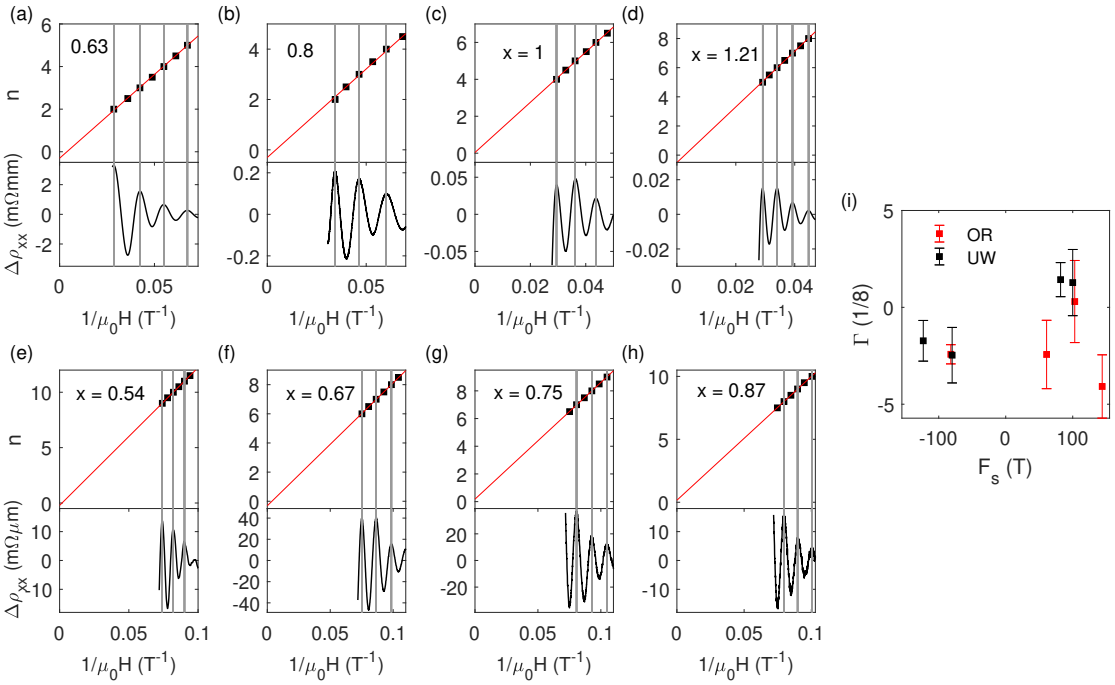

Figure 3.8: **The phase shift of quantum oscillations extracted from the Landau fan diagram** (a)–(h) Plot of the Landau level index against the inverse field, with integer Landau level indices assigned to resistivity peaks. Red solid curves are linear fits. (i) The phase shift Γ extracted from the y-intercept of the linear fits in the Landau fan diagram as a function of oscillation frequency.

electron pocket size decreases while the hole pocket size increases. We note that shifts of the oscillation with temperature have been observed in the magnetic topological semimetal PrAlSi [29], and in the magnetic semimetal CeBiPt [30], suggesting that the phenomenon may be generic to magnetic semimetals.

3.4.2 Berry phase extracted from the Landau fan diagram

Another indicator that has been widely used to determine the topological nature of a band structure is the phase shift, λ, of the quantum oscillations [31]. This has three contributions: ϕ_B, due to the geometric phase; ϕ_R, due to the orbital magnetic moment; and ϕ_Z, due to the Zeeman coupling. It has often been assumed that in 3D metals, Dirac-type bands lead to $\phi_B = \pi$ and parabolic bands lead to $\phi_B = 0$. However, a recent

comprehensive analysis has shown that ϕ_B is in general a continuous quantity and is only fixed to the specific values of 0 and π in certain symmetry classes determined by the space group and the type of cyclotron orbits [32]. The cyclotron orbit and the point group symmetry of FM $MnBi_{2-x}Sb_xTe_4$ do not belong to one of those symmetry classes, and therefore we do not expect to observe either $\phi_B = 0$ or π. Hence the phase shift cannot be used as conclusive evidence for Weyl points in this system.

For the sake of completeness, however, we present an analysis of the phase shift of the quantum oscillations. We analyzed the doping dependence of phase shift λ by constructing Landau fan diagrams from quantum oscillations, as shown in Fig. 3.8. We assigned integer Landau level indices to resistivity peaks, which were shown to coincide with Landau band edges in a study in which numerical simulation of a minimal magnetic Weyl semimetal was performed [65]. The phase shift λ is determined by the following relation:

$$\Gamma = -\frac{1}{2} + \lambda + \delta \tag{3.3}$$

in which Γ is the y-intercept of the linear fits to Landau indices n versus inverse field, and $|\delta|$ is 1/8 with the sign depending on whether the orbit is the minimum or maximum of the Fermi surface. We plot Γ as a function of oscillation frequency in Fig. 3.8(i). Notice that λ contains a contribution from Berry curvature, orbital moment, and Zeeman coupling, i.e., $\lambda = (\Phi_B + \Phi_R + \Phi_Z)/2\pi$. Their contributions cannot be separated without an analysis of the higher harmonics of quantum oscillations, which we did not observe. We also do not expect $\Phi_B = 0$ or π based on the space group symmetry and the orbits of $MnBi_{2-x}Sb_xTe_4$. Hence, we cannot determine the existence of Weyl points based on the extracted Γ.

3.5 Conclusions

In summary, we obtained important insight into the bulk electronic structure of FM $MnBi_{2-x}Sb_xTe_4$ using quantum oscillation measurements. From the temperature dependence of the oscillation frequency, we infer that the electronic structure is sensitive to the magnitude of the magnetization, while in the limit of saturated c-axis magnetization, we find good overall agreement with band-structure calculations. This lays the foundation for understanding magnetism-induced topological phases in this class of materials.

We close this chapter by identifying two remaining questions that require further investigation. Firstly, for an ideal type-II Weyl semimetal, as the Fermi energy moves from the heavily electron-doped to the heavily hole-doped condition, the Fermi surface evolves from a single electron pocket that encloses both Weyl points, to two electron pockets each enclosing a single Weyl point, to a coexistence of one hole pocket and two electron pockets, and finally to one hole pocket that encloses both Weyl points. However, in this study, only a single quantum oscillation frequency was observed. A more detailed investigation of the electronic structures near the putative Weyl crossing is necessary to conclusively identify the electronic band topology of FM $MnBi_{2-x}Sb_xTe_4$. Secondly, this study has been focused on the electronic strcutures of FM $MnBi_{2-x}Sb_xTe_4$ when the magnetization is polarized along c-axis. Both theoretical calculations and experimental observations have demonstrated that the electronic structure of this material sensitively depends on its magnetism. It is therefore important to investigate how the electronic structure changes as the magnetization is polarized along different angles. We will address these two questions in the following chapters.

Chapter 4

FERMI SURFACE EVOLUTION AND ANOMALOUS HALL EFFECT IN AN IDEAL TYPE-II WEYL SEMIMETAL $MnBi_{2-x}Sb_xTe_4$

4.1 Abstract

Weyl semimetals (WSMs) are three-dimensional topological materials that exhibit fascinating properties due to the presence of Weyl nodes in their band structure, including chiral anomaly, Fermi arc, and intrinsic anomalous Hall effect. However, the existing WSMs discovered so far often possess multiple pairs of Weyl nodes, posing challenge in disentangling the contributions to transport phenomena from different energy bands and mechanisms. To overcome this challenge, we have identified field-induced ferromagnetic $MnBi_{2-x}Sb_xTe_4$ as an ideal type-II WSM with a single pair of Weyl nodes. By employing a combination of quantum oscillations and high-field Hall measurements, we have resolved the evolution of Fermi surfaces as the Fermi level is tuned across the charge neutrality point. This evolution precisely matches the band structure of an ideal type-II WSM. Furthermore, the anomalous Hall conductivity exhibits a singular, heartbeat-like behavior as the Fermi level is tuned across the Weyl nodes, a unique feature previously predicted theoretically for a type-II WSM. Our findings establish $MnBi_{2-x}Sb_xTe_4$ as an ideal and tunable platform for further investigation into Weyl physics.

4.2 Introduction

The Weyl semimetal (WSM) is a three-dimensional gapless topological phase characterized by energy bands that intersect at points in momentum space known as Weyl nodes [10, 66, 67]. The stability of these band crossings relies on the breaking of either time reversal or inversion symmetry. The low energy quasiparticles near the Weyl nodes are described by the relativistic Weyl equations, giving rise to Weyl fermions in condensed matter systems. Unlike their high energy counterpart, the Weyl fermions in WSMs are not constrained

by Lorentz symmetry, allowing the Weyl cones to tilt in the energy-momentum space [68]. When the tilting of the cones is large enough that the velocity changes sign along the tilting direction, a transition from type-I to type-II WSMs occurs. In type-I WSM (Fig. 4.1(b)), the Fermi surfaces are point-like objects located at the Weyl nodes when the Fermi energy aligns with the Weyl crossing. In contrast, in type-II WSMs (Fig. 4.1(a)), the tilting of the cones leads to extended electron and hole Fermi pockets touching at the Weyl nodes [69].

The tilting of Weyl cones leads to distinct transport behavior in two types of WSMs [70, 3, 13]. In a type-I WSM without cone tilting, the anomalous Hall effect is solely determined by the location and the topological charge of the Weyl nodes, and the free carriers do not contribute to the anomalous Hall conductivity (AHC) either intrinsically or extrinsically. Consequently, the magnitude of AHC is independent of the Fermi level position, even when the Fermi level is tuned above or below the Weyl crossings [3]. On the other hand, in a type-II WSMs, in addition to the contribution from the Weyl points, the tilting of the Weyl cones give rise a logarithmically divergent contribution to AHC from the Fermi surfaces, which is only truncated by the finite size of electron and hole pockets [13]. As a result, when the Fermi level is tuned across the type-II Weyl crossing and the electron and hole pocket shrinks and emerges, the AHC changes rapidly, exhibiting a singular behavior as a function of doping.

An outstanding challenge in the field of WSMs is to isolate the effect of Weyl nodes and experimentally observe the theoretically predicted exotic transport effects. Unfortunately, most of the WSMs discovered so far have multiple pairs of Weyl nodes and coexist with other topological trivial bands, complicating the interpretation of transport measurements. For instance, in $Co_3Sn_2S_2$, a magnetic Weyl semimetal, three pairs of Weyl nodes are observed along with 16 electron pockets and 12 hole pockets [71, 72, 73, 74]. Such complex band structures make it very challenging to disentangle the contributions to AHC from various energy bands and intrinsic/extrinsic mechanisms. A solution to this challenge is to realize a tunable material system with a single pair of Weyl nodes, an ideal WSM, and simultaneously monitor the evolution of Fermi surfaces and AHC as the Fermi level is tuned across the Weyl nodes.

In this paper, we show that the field induced ferromagnetic state of $MnBi_{2-x}Sb_xTe_4$ is

the long sought ideal WSM. By substituting Bi with Sb, we are able to tune the carriers from n-type to p-type, allowing us to study the evolution of Fermi surfaces by a combination of quantum oscillations and high field Hall measurements. The observed evolution of the Fermi surfaces can only be explained by the band structure of a single pair of type-II Weyl nodes. Furthermore, the anomalous Hall conductivity exhibits a strong dependence on doping near charge neutrality, displaying a divergent behavior that is consistent with expectations for a type-II WSM [13] and in agreement with results from density functional theory (DFT) calculations. Our findings provide a definitive identification of an ideal type-II Weyl semimetal in $MnBi_{2-x}Sb_xTe_4$, offering a valuable platform for further studies of Weyl physics.

4.3 Results

$MnBi_2Te_4$ is a van der Waals layered antiferromagnetic topological insulator. DFT calculations have predicted that the band structure of $MnBi_2Te_4$ in the field induced ferromagnetic phase is characterized by a single pair of type-II Weyl nodes [14, 75]. However, these calculations have also shown that $MnBi_2Te_4$ can be easily tuned to a type-I WSM or a trivial insulator phase by small amount of strain [76]. Previous quantum oscillations studies of $MnBi_{2-x}Sb_xTe_4$ show that the doping dependence of oscillation frequencies and effective mass is broadly consistent with the DFT calculations [77, 78]. Nevertheless, only a single oscillation frequency has been observed, which is insufficient to conclusively determine whether it is a type-I, type-II WSM or a trivial FM insulator. Anomalous transport behavior including enhanced mobility and AHC has been observed [78], but their relationship with Fermi surface topology has not been fully established.

One of the reasons why it is challenging to resolve multiple frequencies in $MnBi_{2-x}Sb_xTe_4$ is due to the low oscillation frequency (< 100 T) and the limited field range (where oscillations can only be observed above the spin-flip transition at 7 T). To overcome this difficulty, we applied a large magnetic field by a 60 T pulsed magnet and a 31 T DC magnet to a series of $MnBi_{2-x}Sb_xTe_4$ samples with a dense chemical doping distribution near charge neutrality. Fig. 4.2 summarizes representative data of the Shubnikov de-Haas (SdH) oscillations in $MnBi_{2-x}Sb_xTe_4$. We categorized the data into three categories, n-doped ($x < 0.7$, Fig.

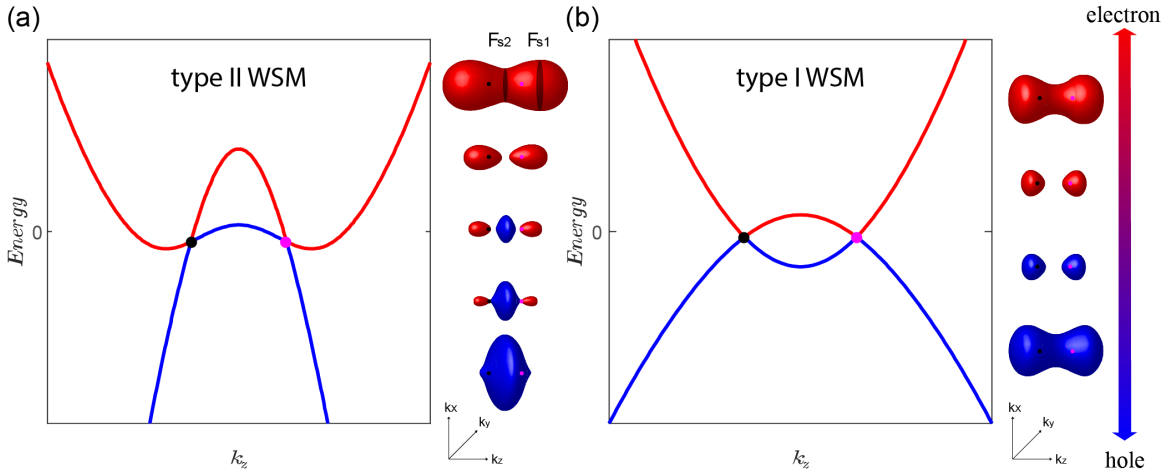

Figure 4.1: **Schematic diagram of band structures and Fermi pockets of an ideal type-II and type-I Weyl semimetals** (a)-(b) Band dispersion of an ideal type-II (a) and type-I (b) Weyl semimetals along the k_z direction when a pair of Weyl nodes locates along the $\Gamma - Z$ cut. On the right, the evolution of the Fermi pockets as the Fermi level moves across the Weyl nodes are exhibited. The red line and pockets refer to electrons, whereas the blue line and pockets represent hole carriers. The magenta and black points represent the Weyl nodes with positive and negative chirality respectively.

4.2(a)-(f)), p-doped ($x > 0.7$, Fig. 4.2(i)-(l)), and near charge neutrality ($x \sim 0.7$, Fig. 4.2(g)-(h)). All the data were measured at the base temperature with the magnetic field along the c-axis. In the case of n-doped samples, the amplitude of the magnetoresistance oscillations shows a dramatic increase when the magnetic field is above 40T (Fig. 4.2(e)-(f)), whereas for the p-doped samples, the amplitude of oscillations gradually increases with the field, consistent with the thermal damping behavior of single-frequency oscillations (Fig. 4.2(i)-(l)). A closer inspection of the data for the n-doped sample reveals that the change in oscillation amplitude is caused by a beating effect from multiple frequencies (Fig. 4.2(a)-(d)), which is also observed in data below 40T (Fig. 4.2(e)-(f)).

We utilized FFT to the oscillatory signals to gain a quick overview of the evolution of oscillation frequencies as a function of doping (Fig. 4.2(m)). The FFT spectrum reveals that the oscillation frequency decreases as the doping approaches charge neutrality, which is consistent with the previous studies. However, on the n-doped side ($x < 0.7$), two peaks

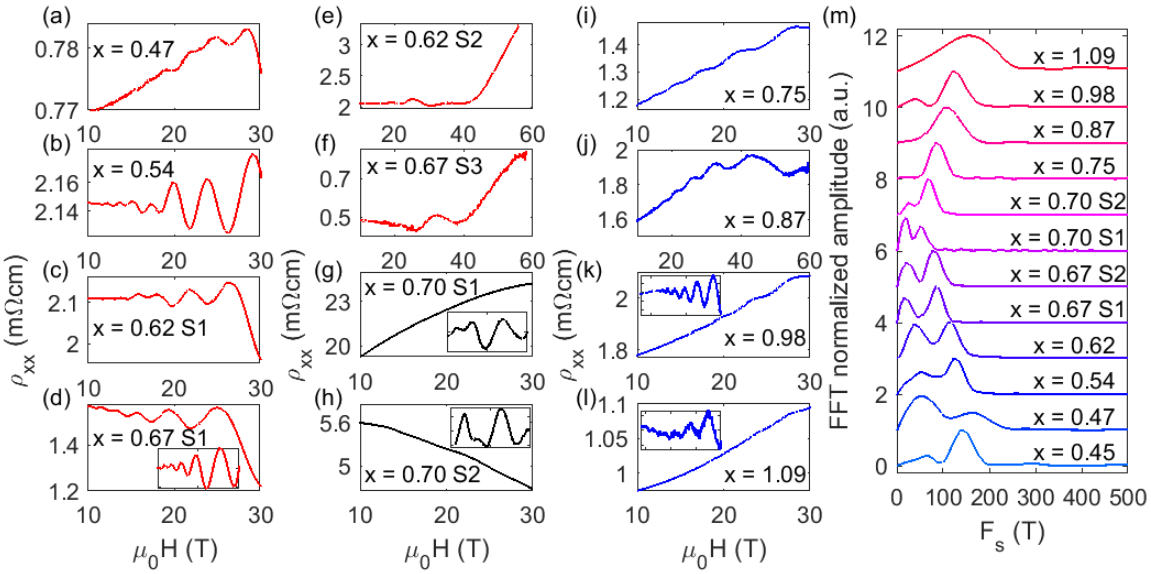

Figure 4.2: **SdH oscillations and FFT of $MnBi_{2-x}Sb_xTe_4$ under pulsed (60T) and DC (31T) magnetic field** (a) - (i) magnetoresistivity of (a)-(f) electron-doped, (g)-(h) near charge neutrality point, and (i)-(l) hole-doped $MnBi_{2-x}Sb_xTe_4$ samples. Insert demonstrates the oscillatory part after polynomial background subtraction. (m) Fast Fourier transform spectrum of the SdH oscillations for various dopings. Each spectrum is offset by 1 for clarity.

are always observed, whereas on the p-doped side ($x > 0.7$), only one peak is observed. We note that the FFT peaks are broad due to the limited number of observed oscillations, especially for the samples near charge neutrality. In such conditions, a more accurate analysis is obtained by directly fitting the oscillatory signals with the Lifshitz-Kasovich (LK) formula (see Appendix). Representative examples of the fitting are shown in fig 4.3(a)-(d). The fitting yields two oscillation frequencies for electron-doped samples, and a single frequency of 146T for p-doped sample with x = 1.09. The fit also confirms that the rapid increase of oscillation amplitude above 40T is indeed caused by a beating effect of two oscillation frequencies as the system approaches the quantum limit. Fig. 4.3(e) summarizes the frequency as a function of doping extracted from the fitting, showing good agreement with the FFT analysis.

The oscillation frequency provides us with information about the extremal cross-sectional

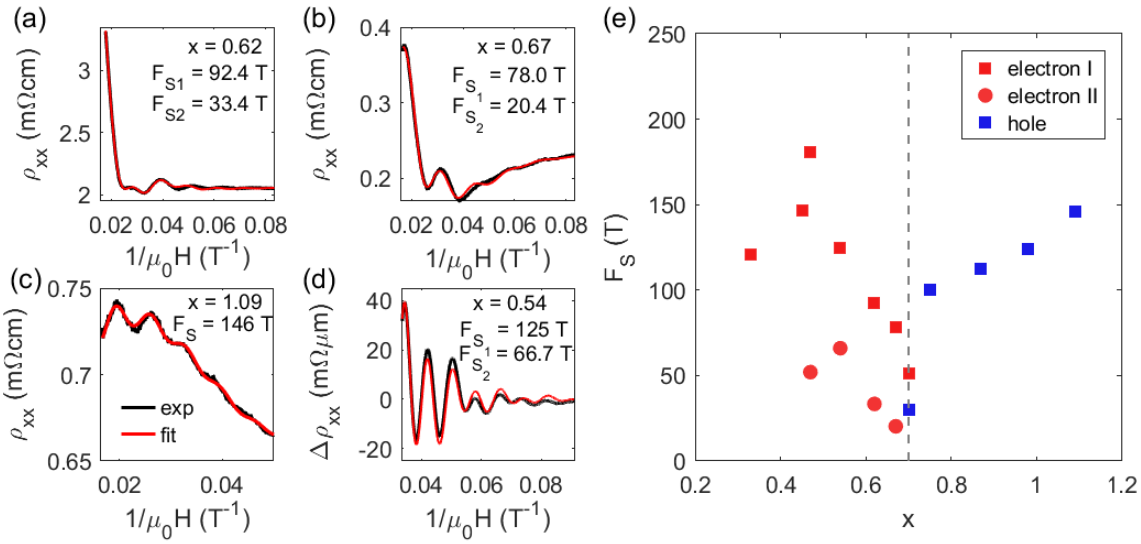

Figure 4.3: **Analytical fitting of SdH oscillations of $MnBi_{2-x}Sb_xTe_4$** (a) – (c) Magnetoresistivity as a function of $1/\mu_0 H$ measured under a 60T pulsed magnetic field with $\mu_0 H//[001]$ at 1.5K and the analytical fit to the Lifshitz-Kosevich (LK) formula for (a) electron-doped x = 0.62, (b) electron-doped x = 0.67, and (c) hole-doped x = 1.09. (d) Oscillatory part of the magnetoresistivity as a function of $1/\mu_0 H$ measured under a 31T DC magnetic field with $\mu_0 H//[001]$ at 1.5K for electron-doped $MnBi_{2-x}Sb_xTe_4$ (x = 0.54) and the analytical fit to the Lifshitz-Kosevich (LK) formula. The black lines represent the experimental data, whereas the red lines represent the fit. (e) doping dependence of oscillation frequencies extracted from the analytical fitting to the LK formula. The red squares denote the band maximum ($k_z \neq 0$) of the electron pocket whereas the red circles denote the band minimum ($k_z = 0$) of the electron pocket. The blue squares represent the band maximum at $k_z = 0$ of the hole pocket.

area of the Fermi surface perpendicular to the magnetic field, as determined by the Onsager relation ($F_s = \frac{\hbar}{2\pi e} A$). However, it does not indicate whether these frequencies correspond to separate Fermi surfaces or different extremal cross-sectional areas of a single Fermi surface. To address this question, we turn to the Hall resistivity. Specifically, we focus on the Hall resistivity above the saturation field, which is relevant to the electronic structure in the field induced ferromagnetic state. Our findings, as shown in Fig. 4.4, reveal that the Hall resistivities are always linear in B, except for the doping closest to charge neutrality ($x = 0.7$). The linear Hall resistivity can only arise from a single type of carrier. Therefore,

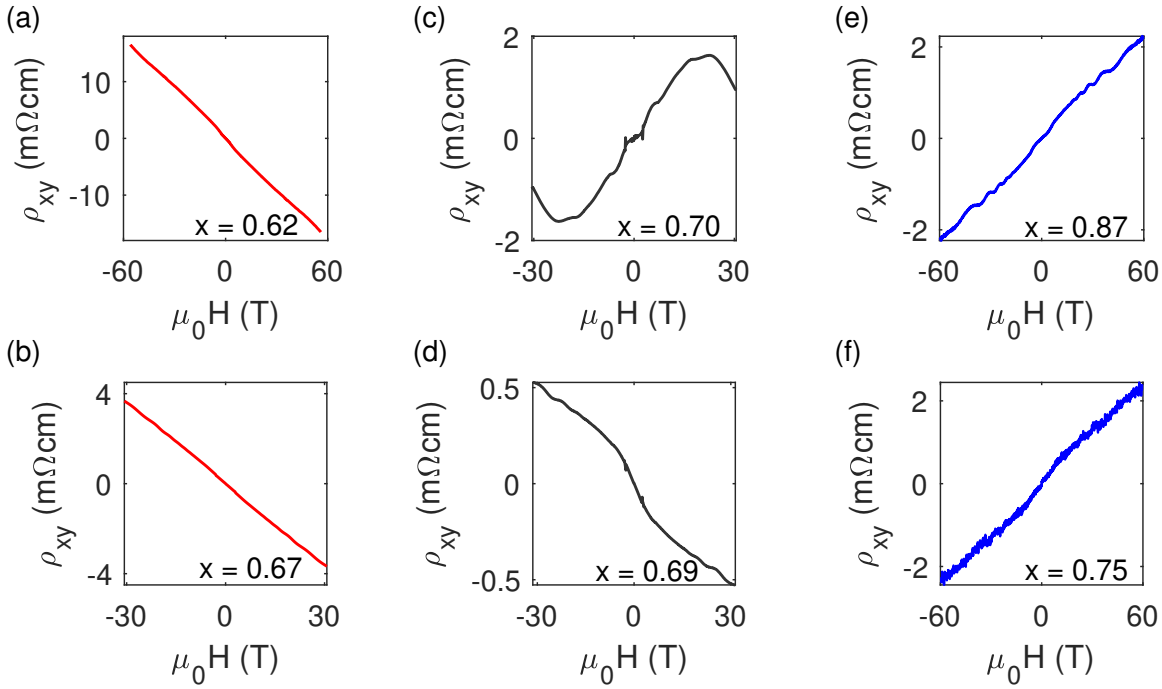

Figure 4.4: **High field Hall resistivity of $MnBi_{2-x}Sb_xTe_4$** (a)-(f) Hall resistivity with $\mu_0 H//[001]$ at 1.5K for electron-doped (a) x = 0.62, (b) x = 0.67, near the charge neutrality point (c) x = 0.70, (d) x = 0.69, and hole-doped (e) x = 0.87, (f) x = 0.75 samples.

we conclude that the two frequencies observed in the quantum oscillations arise from the two extremal cross-sectional areas of a single Fermi surface, except for $x = 0.7$.

The high field Hall resistivity of $x = 0.7$ exhibits strong nonlinearity, changing from a positive slope to a negative slope, as shown Fig. 4.4(c). This suggests the coexistence of electrons and holes pockets. To extract the electron and hole carrier densities, we fit the Hall resistivity data to the effective two-band model, using the longitudinal resistivity at the upper critical field as a constraint (Fig. 4.5). The fitting yields an electron density $2.37 \times 10^{17} cm^{-3}$ with a mobility of 1144 $cm^2/V/s$ and a hole density $2.35 \times 10^{17} cm^{-3}$ with a mobility of 1252 $cm^2/V/s$. The coexistence of electron and hole carriers rules out the possibility of $MnBi_{2-x}Sb_xTe_4$ being a type-I WSM or gapped insulator, as neither scenario allows for the coexistence of electron and hole pockets.

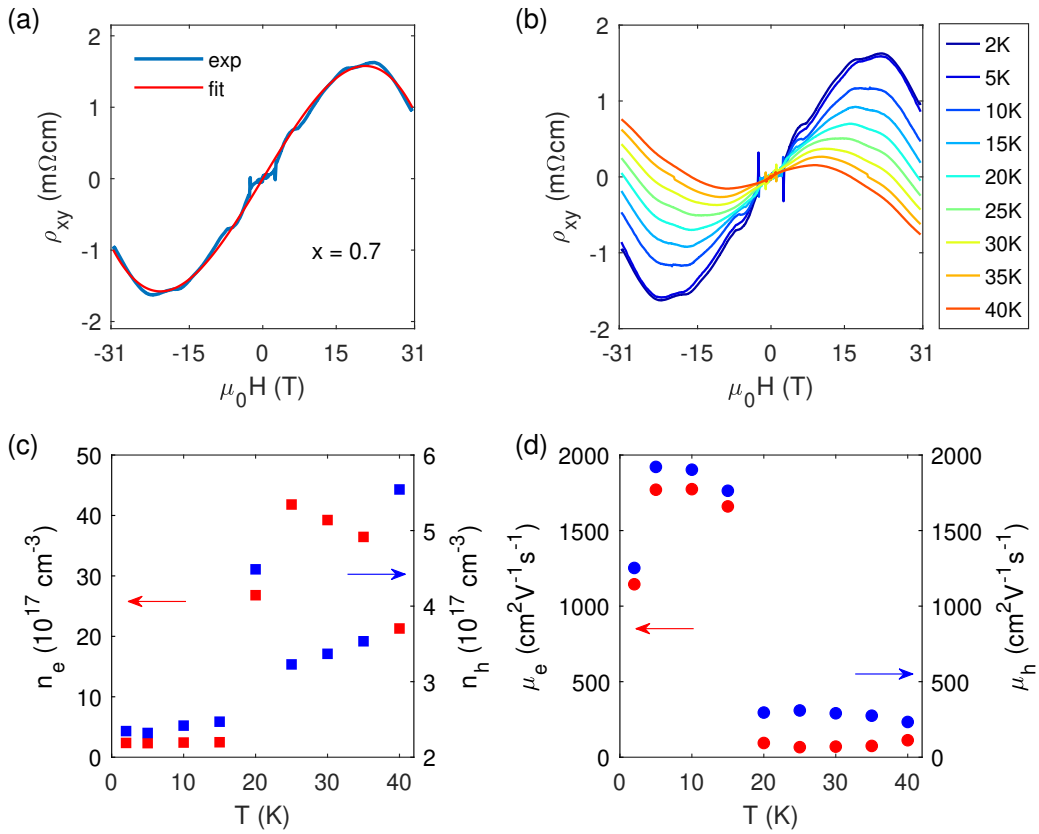

Figure 4.5: **Multiband Hall resistivity of $MnBi_{2-x}Sb_xTe_4$**($x = 0.7$) (a) Hall resistivity (blue) and the fit to the two-band model (red) with $\mu_0 H//[001]$ at 2K (b) The field dependence of Hall resistivity at various temperatures with $\mu_0 H//[001]$ (c)-(d) The temperature dependence of the fitting parameters of the effective two-band model: (c) electron carrier density (red) and hole carrier density (blue) (d) electron mobility (red) and hole mobility (blue).

We can now compare the observed quantum oscillation frequency with the predicted Fermi surfaces based on the type-II WSM band structure (Fig. 4.1(a)). When the Fermi level is slightly above the Weyl nodes and the Lifshitz energy, a single electron pocket encloses two Weyl points and has a dumbbell shape aligned with the k_z axis where the two Weyl nodes are located. As a result, there are three extremal orbits - one minimum at $k_z = 0$ and two equivalent maxima at $k_z \neq 0$. The minimum and maxima correspond to the two

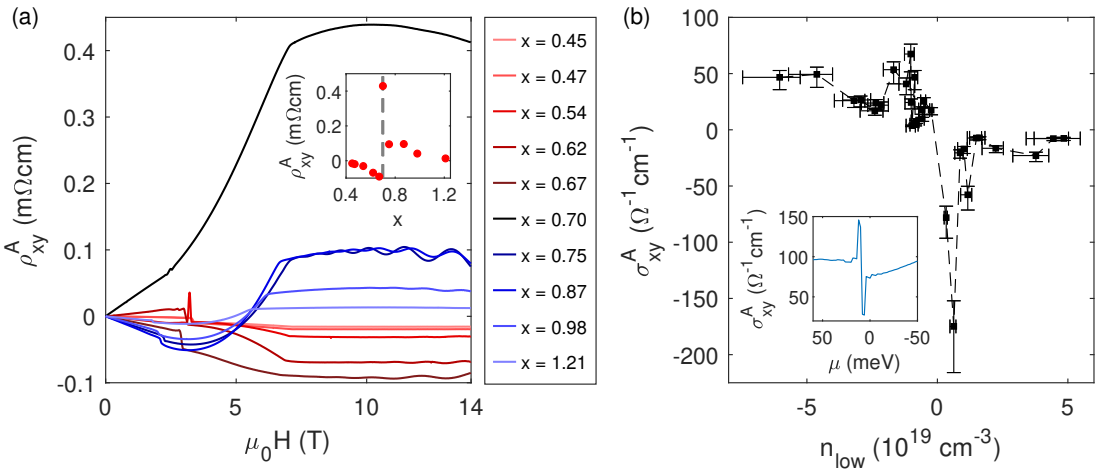

Figure 4.6: **The evolution of anomalous Hall effect near the Weyl points**(a) anomalous Hall resistivity (AHR) as a function of magnetic field strength with μ_0 H//[001] at 2K for different chemical dopings. Insert of (a) shows the doping dependence of AHR. (b) Anomalous Hall conductivity (AHC) as a function of carrier density (n_{low}) extracted by fitting the low-field Hall resistivity linearly. The error bar represents the possible experimental error caused by the uncertainty in the measurements of sample dimensions. Insert of (b) demonstrates the DFT calculations of the AHC as a function of chemical potential in field-induced FM $MnBi_2Te_4$.

frequencies observed in slightly n-doped samples ($0.47 < x < 0.7$). When the Fermi level is well below the Weyl nodes, a single hole pocket with a single extremal orbit at $k_z = 0$ is expected, which agrees with the single oscillation frequency observed in hole-doped samples ($x > 0.7$). Finally, when the Fermi level is below the Lifshitz energy and near the Weyl points, two identical electron pockets and a single hole pocket are expected, each with a single extremal orbit. This explains the two frequencies observed in the $x = 0.7$ sample. Remarkably, the carrier density calculated from the oscillation frequency, assuming spherical Fermi surfaces, qualitatively agrees with carrier density extracted from the two-band fitting of Hall resistivity. This agreement suggests that the quantum oscillations measurements have captured all the carriers participating in the transport, and the Fermi surface evolution described above provides a complete characterization of the electronic structure of this system.

After identifying the Fermi surface topologies $MnBi_{2-x}Sb_xTe_4$, we can now investigate the unique transport signature associated with an ideal type-II WSM. A well know result of the TRS breaking WSM is that the AHC is a topological quantity determined by the separation of Weyl nodes in momentum space, independent of the position of the Fermi level. However, this is not the case when the Weyl cones are tilted, as both Berry curvature and skew scattering effects can contribute to AHC in the presence of Fermi surfaces [79]. In type-II WSM, when the Fermi level is tuned across the Weyl nodes, the rapid changes of Fermi surfaces lead to a dramatic variation of AHC. To explore this effect, we conducted a detailed study of the AHC as a function of doping near charge neutrality point.

Figure 4.6(a) displays the field dependence of the anomalous Hall resistivity for a series of chemical dopings, obtained by subtracting the ordinary Hall resistivity background. The inset of Figure 4.6(a) summarizes the magnitude of the anomalous Hall resistivity as a function of doping. With increasing Sb concentration, the anomalous Hall resistivity changes sign from negative to positive and reaches a maximum magnitude the charge neutrality point ($x = 0.7$). We then converted the anomalous Hall resistivity to AHC and plotted it as a function of carrier density in the AFM state extracted from the low field Hall resistivity (Figure 4.6(b)). This carrier density is considered as a proxy of the Fermi level position. Remarkably, a singular AHC with an upturn followed by a downturn was observed as the Fermi level is tuned from above to below the Weyl points. This behavior is in excellent agreement with the theoretical expectations for an ideal type-II WSM and is also qualitative consistent with the DFT calculations (Insert of Figure 4.6(b)). Although there is an overall shift of approximately $100\Omega^{-1}cm^{-1}$ between the experimental and DFT calculated AHC values, this discrepancy is likely due to the extrinsic contributions to AHC not captured by the calculations, or the differences in the detailed band structures [80]. Nevertheless, the characteristic heartbeat pattern of the AHC of an ideal type-II WSM was observed with a comparable magnitude, further confirming that $MnBi_{2-x}Sb_xTe_4$ is indeed an ideal type-II WSM.

4.4 Conclusion

In conclusion, our findings establish the field-induced ferromagnetic $MnBi_{2-x}Sb_xTe_4$ as an ideal type-II Weyl semimetal, with a single pair of Weyl nodes near Fermi energy. Through the combined techniques of quantum oscillations and high field Hall measurements, we demonstrate that the evolution of Fermi surfaces can only be explained by the band structure of an ideal type-II Weyl semimetal. Furthermore, we observed a strong doping dependence of the anomalous Hall conductivity near charge neutrality, exhibiting a divergent behavior consistent with expectations for a type-II WSM and supported by DFT calculations. Our work highlights $MnBi_{2-x}Sb_xTe_4$ as a promising platform for further investigations into Weyl physics. Moreover, the highly tunable nature of $MnBi_{2-x}Sb_xTe_4$ with electronic structures sensitive to strain, pressure, chemical doping, and magnetic field angle make it a versatile platform for exploring topological phase transitions [14, 17, 81, 82, 83].

Chapter 5

EVIDENCE OF AN IN-SITU CONTROLLED TYPE-II TO TYPE-I WEYL SEMIMETAL TRANSITION BY MAGNETIZATION ROTATION

5.1 Abstract

Weyl semimetals are a distinctive class of topological semimetals that host Weyl fermions as low-energy excitations in their electronic band structure. Controlling Weyl semimetal phases and their properties via a type-II to type-I Lifshitz transition carries significant fundamental interest, offering valuable insights for researchers across condensed matter and high-energy physics. In this chapter, we report the realization of an in-situ controlled Lifshitz transition in field-induced FM $MnBi_{2-x}Sb_xTe_4$ from an ideal type-II to type-I WSM with an easy knob of magnetic field angle. Evidence of this Lifshitz transition includes the anomalous angular dependence of Shubnikov de Haas oscillations and high-field Hall resistivity, indicating changes in Fermi surfaces, and an unusual angle dependence of anomalous Hall conductivity, implying alterations in the underlying Fermi surface topology.

5.2 Introduction

As introduced in previous chapters, WSM is a 3D topological semimetal with singly degenerated bands touching at certain k-points, near which the low energy excitation can be seens as quasiparticles of Weyl Fermions [10]. The band crossings in WSMs, known as Weyl nodes, act as monopoles of Berry curvature. The existence of Weyl nodes leads to exotic phenomena such as chiral anomaly, Fermi arc surface states, and intrinsic anomalous Hall conductivity. WSMs can be broadly classified into two categories: type-I and type-II. Type-I WSMs are characterized by untilted or slightly tilted Weyl cones that meet at the Weyl nodes. In contrast, type-II WSMs exhibit strongly tilted Weyl cones, which cause the coexistence of electron and hole pockets at certain Fermi energy [68]. This distinction between type-I and type-II WSMs results in diverse electronic properties and topological

responses. For instance, type-II WSMs exhibit a pronounced change in the anomalous Hall conductivity as the chemical potential shifts across the Weyl nodes [13] whereas the AHC of type-I WSMs is quantized [3], depends solely on the Weyl nodes seperation when the chemical potential is near the Weyl nodes.

One important focus of topological materials research is the control of topological phase transitions and the corresponding properties. The ability to control and manipulate the transition between type-I and type-II WSMs is of great interest to researchers, as it opens up avenues for exploring novel quantum phenomena and engineering advanced applications in topological materials. The Lifshitz transition from type-I to type-II WSM is also of fundamental interest in high-energy physics for its analogy to black hole horizons [69]. Type-II WSMs display open Fermi surfaces, analogous to event horizons, as Weyl fermions obey the Weyl equation, which is related to the behavior of particles near black holes. Despite the limitations of the analogy, inducing this Lifshitz transition allows researchers to simulate horizon-like boundaries in a controlled laboratory setting, offering valuable insights into black hole physics. Several studies have been conducted on the control of WSM phases in various material systems, employing external parameters such as pressure, chemical doping, and temperature. However, these approaches generally require complex experimental setups or irreversible changes to the material properties.

$MnBi_{2-x}Sb_xTe_4$, an intrinsic magnetic topological material with a strong interplay between magnetism and electronic structure, serves as an ideal platform for realizing topological phase transitions using an external magnetic field as a simple and reversible control parameter. In the field-induced FM state, $MnBi_{2-x}Sb_xTe_4$ has been proposed and observed to be an ideal type-II Weyl semimetal with a single pair of Weyl nodes near the Fermi energy (near x = 0.7) along the $\Gamma - Z$ cut. DFT calculations indicate that the Zeeman field-induced band splitting is considerably larger for the FM-z configuration than for the FM-x configuration in this layered structure, resulting in significant changes in band dispersions near the Weyl points as the magnetic field angle θ varies [81]. Additionally, applying a magnetic field to rotate the magnetic orientation away from the z-axis disrupts the C_{3z} symmetry, leading the Weyl points to shift away from the Γ-Z line and move towards general $\mathbf{k}$ points. A potential quantum phase transition from a type-II to type-I WSM phase may

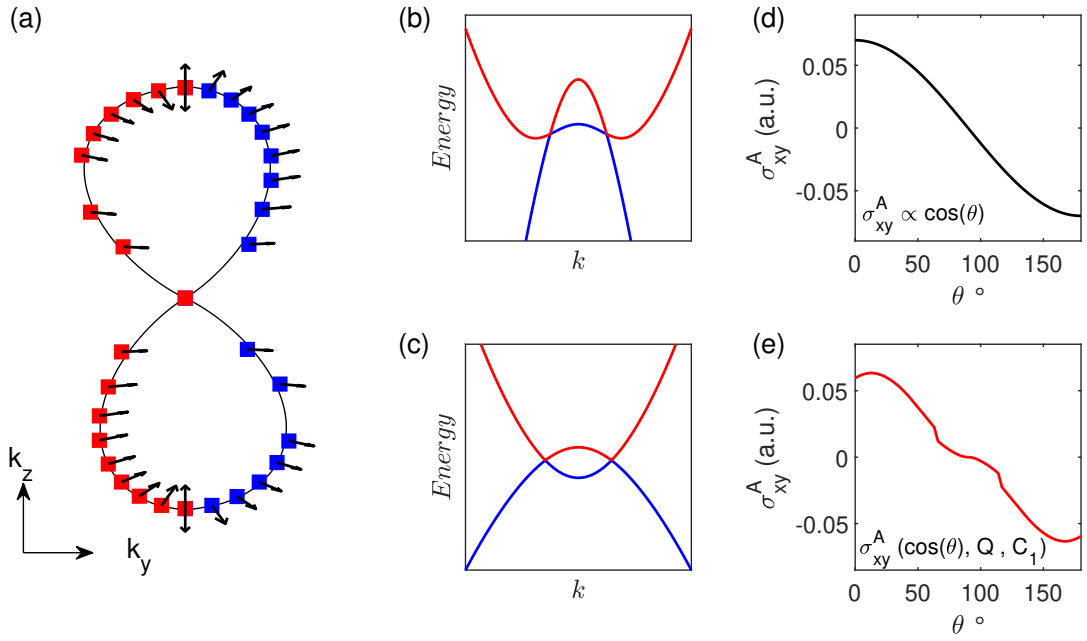

Figure 5.1: **Schematics of Lifshitz transition controlled by magnetic field angle** (a) Schematic of the evolution of Weyl points in momentum space when magnetization orientation (denoted by black arrows) rotates from the out-of-plane to in-plane direction in the k_y -k_z plane. The blue and red squares represent the Weyl points with +1 and -1 chirality. (b)-(c) the electronic structure of (b) an ideal type-II Weyl semimetal and (c) an ideal type-I Weyl semimetal. (d)-(e) the intrinsic anomalous Hall conductivity as a function of magnetic field angle θ when (d) only the geometrical factor $cos(\theta)$ is considered and (e) the geometrical factor, the changes in Weyl nodes separation, and the changes in the Weyl cone tilted angle are simultaneously considered.

occur as the magnetization orientation rotates from out-of-plane to in-plane. When $\theta = 90°$ (FM-x configuration), the two Weyl points ultimately merge, causing the annihilation of Weyl fermions and a topological transition to a trivial phase.

In this chapter, we report experimental evidence of an in-situ controlled Lifshitz transition in FM $MnBi_{2-x}Sb_xTe_4$ from an ideal type-II to type-I WSM with an easy knob of magnetic field angle. The evolution of the electronic structure as the magnetic field rotates from out-of-plane to in-plane is probed by both angular-dependent quantum oscillation and high-field Hall measurements. First, an abrupt change is observed in both frequency and

amplitude of the Shubnikov-de Haas oscillations for the compound (x = 0.7) near the putative Weyl points, while a regular angle dependence is observed for heavier doped samples as expected for a 3D Fermi pocket. Secondly, the high-field Hall resistivity for the sample near the Weyl points shows a significant variation as the magnetic field angle changes, from a two-band Hall behavior to a single-band linear Hall dependence with a comparative slope to that of the low-field AFM case, suggesting a possible Lifshitz transition from a type-II to a type- I WSM in the field-induced FM state. Furthermore, we examine how the tuning of the Weyl nodes and possible Lishitz transition affects the anomalous Hall conductivity, and observed an anomalous zigzag angular dependence for samples near the Weyl points, in agreement with the theoretical expectation on the angular dependence of the intrinsic AHC across a Lifshitz transition from type-II to type-I WSM.

5.3 Results

Fig. 5.2 (a)-(c) display the SdH oscillations of $MnBi_{2-x}Sb_xTe_4$ (x 0.67, 0.7, and 0.75) measured under 31T DC magnetic field as the magnetic field rotates from out-of-plane ($\mu_0 H//c$) to in-plane ($\mu_0 H//ab$). For the electron-doped (x = 0.67, Fig.5.2(a)) and hole-doped (x = 0.75, Fig.5.2(b)) samples, the major frequency of the SdH oscillations obtained by fitting the Landau Fan diagram shows a regular dependence on the magnetic field angle as expected for a 3D Fermi pocket (Fig. 5.2(d)-(e)).

$$F_S^{3D} = F_S^z F_S^i / \sqrt{(F_S^z sin\theta)^2 + (F_S^i cos\theta)^2} \tag{5.1}$$

The amplitude of the oscillations decreases monotonically as the magnetic field rotates towards the a-b plane. In contrast, for the sample whose Fermi level is close to the Weyl points (x = 0.7), both the amplitude and frequency show a non-monotonic angle dependence. The amplitude (frequency) first decreases (increases) as the magnetic field angle increases from 0° to 45°, and changes abruptly near $\theta = 45°$. It is worth mentioning that under a higher magnetic field, a secondary frequency was observed in the electron-doped and critical-doped samples, which beats with the major frequency. However, for the data showcased in Fig. 5.2(b), the beating effect is marginal so that the peak and valley positions relatively accurately reflect the major frequency. However, for the sample near the critical doping, due

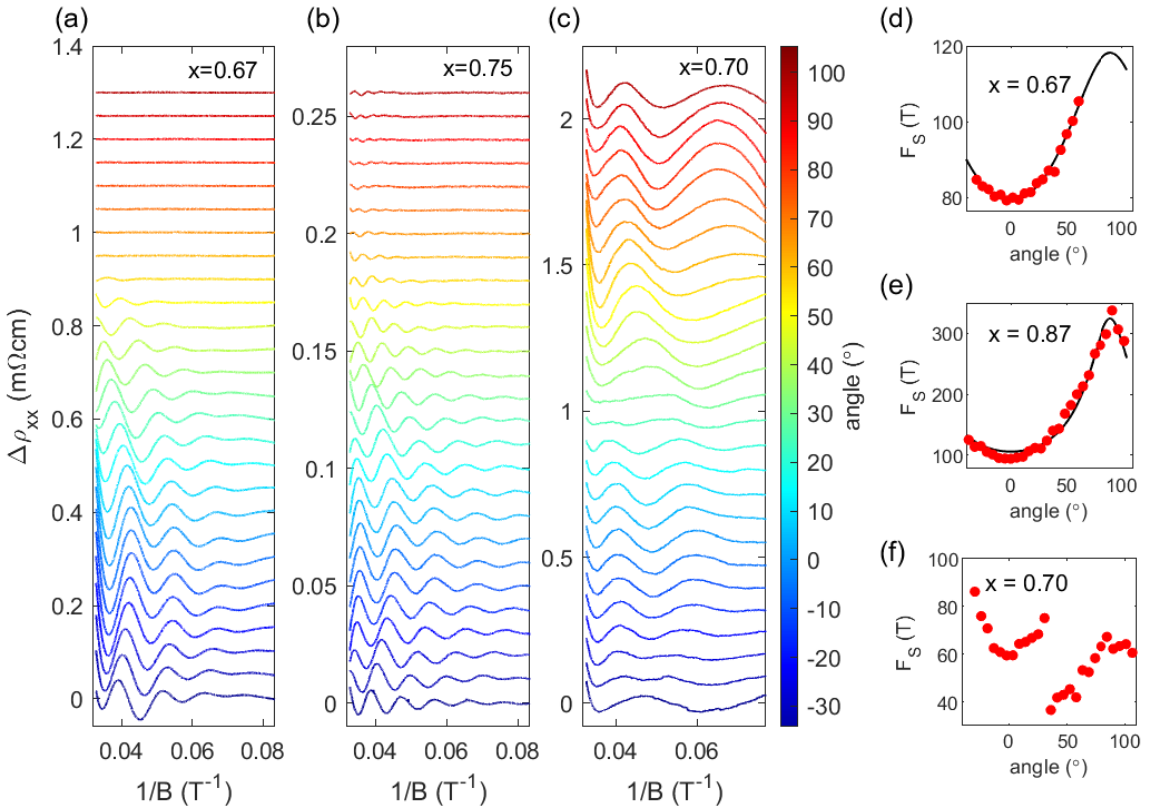

Figure 5.2: **Magnetic field angle dependence of SdH oscillations of $MnBi_{2-x}Sb_xTe_4$.** (a)-(c) Oscillatory part of magnetoresistivity of $MnBi_{2-x}Sb_xTe_4$ (a) electron-doped x = 0.67, (b) hole-doped x = 0.75 (c) near charge neutrality point x = 0.70 under a DC magnetic field of 31T rotating from B //c axis (0°) to B // ab plane (90°). The oscillation signals under different magnetic field angles are offset for clarity and color-coded according to the colorbar to the right of panel (c). (d)-(f) Angle dependence of the major oscillation frequency F_S by tracking the peak and valley positions in $1/B$ and fitting the linear slope. In panel (d) and (e), the black solid lines denote the fitting to the equation of the angle dependence of F_S of a three-dimensional Fermi pocket. In contrast, near the critical doping (x = 0.7), the oscillation frequency shows an abrupt change near 45°, and the oscillation amplitude also reaches a minimum near the same magnetic field angle.

to the small oscillation frequencies of tiny Fermi pockets near the Weyl crossings, only two periods of the oscillatory signal were observed, making it hard to resolve the exact evolution of the SdH oscillations versus the magnetic field angle.

To gain more insights into the evolution of the electronic structure as the magnetic

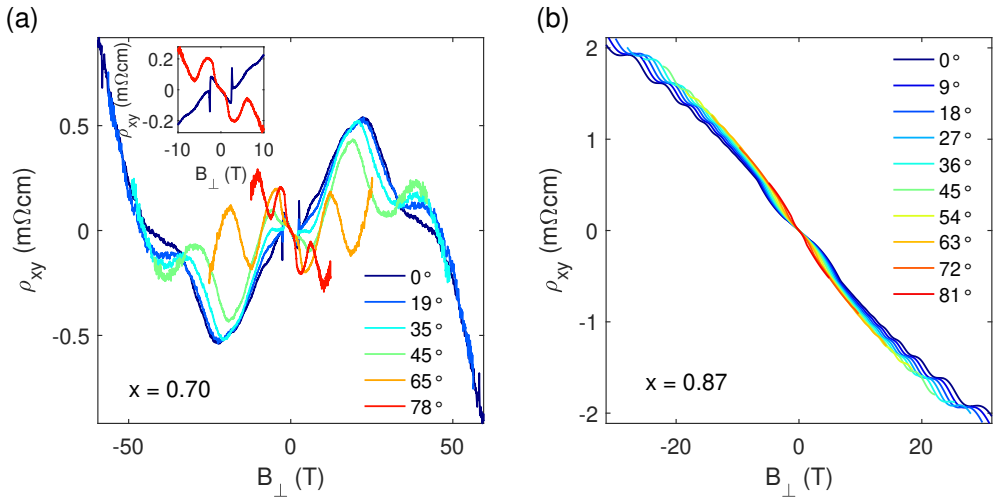

Figure 5.3: **Magnetic field angle dependence of Hall resistivity of $MnBi_{2-x}Sb_xTe_4$.** (a) Hall resistivity of a $MnBi_{2-x}Sb_xTe_4$ (x = 0.7) sample near the charge neutrality point as a function of the out-of-plane projection of magnetic field measured under a 60T pulsed magnetic field with B rotating from B // c axis (0°) to B mostly in the ab plane (78°). (b) Hall resistivity of hole-doped $MnBi_{2-x}Sb_xTe_4$ (x = 0.87) as a function of the out-of-plane projection of magnetic field measured under a 31T DC magnetic field with B rotating from B // c axis (0°) to B mostly in the ab plane (81°). For the heavily hole-doped sample, the Hall resistivities versus the out-of-plane projection of the magnetic field measured under different magnetic field angles collapse together. In contrast, the Hall resistivity of the sample near critical doping only collapses at a low field ($B < H_{c1}$, AFM state). The high-field Hall resistivity of the x = 0.7 sample shows a significant difference under different magnetic field angle, indicating the possibility of a Lifshitz transition as the magnetic field rotates.

field angle changes, we investigated the Hall resistivity ρ_{xy} under a 60T pulsed magnetic field while varying the magnetic field from 0° to 78°. The normal Hall resistivity ρ_{xy} is expected to depend solely on the out-of-plane magnetic field ($B_\perp$) for a fixed electronic structure, resulting in the collapse of the $B_\perp$ dependence of Hall resistivity measured at different angles. Such a collapse was observed in heavily-doped samples as Fig. 5.3(b) shows as an example and in the low field region of the sample close to the Weyl points (Fig. 5.3(a)). For the heavily doped samples, this observation can be explained by the large Fermi surface not significantly affected by subtle changes near the band crossings. In the

low field region ($B < H_{c1}$), the magnetism remains in the AFM-z state and the electronic structure is nearly unaltered. In contrast, the high-field Hall resistivity for the sample near the Weyl points undergoes a significant change as the magnetic field angle rotates, from a two-band Hall behavior ($0° \leq \theta \leq 45°$) to a single-band linear Hall dependence with a comparative slope to the low-field AFM case ($\theta = 78°$). Assuming the total charge in the system is conserved, the net carrier density can be estimated by fitting the linear slope of the low-field Hall resistivity in the AFM state. When the magnetic field is out-of-plane ($\theta = 0°$), the system undergoes an AFM TI to a field-induced ideal type-II WSM transition near the metamagnetic transition, as discussed in previous chapters. The single electron pocket in the AFM state evolves into a coexistence of electron and hole pockets with dominant electron carriers in the FM-z state. As the magnetic field rotates towards the ab plane, the high field slope changes significantly at around $\theta = 60°$. At $\theta = 78°$, the Hall resistivity slope versus the projection of magnetic field $B_\perp$ above $H_c \sim 3T$ becomes comparative to the slope at a low field, suggesting the Fermi surface is dominant by the electron pocket. This is consistent with the possible Lifshitz transition from a type-II WSM where the electron and hole pockets coexist to a type-I WSM with only electron pockets enclosing the Weyl points.

Finally, we investigate the impact of Weyl node evolution and potential Lifshitz transitions on the anomalous Hall conductivity. As predicted by the DFT calculations, the magnetization aligns with the rotation of the magnetic field angle, causing a shift in the Weyl nodes' positions in the k-space [81]. Due to the interplay between magnetism and electronic structure, the Weyl cones undergo a transition from type-II to type-I. When the magnetic field is entirely aligned within the ab plane, the Weyl nodes annihilate each other and the electronic structures become topologically trivial.

Throughout this process, three factors affect the magnetic field angle dependence of the AHC for an ideal WSM (Eq. 1.57). First, a geometric factor proportional to $cos(\theta)$ arises from the rotation of the magnetic field. Second, a factor originating from the change in Weyl node separation, as depicted in Fig. 5.1(a), accelerates the decrease of the AHC as θ increases. The third factor emerges from the alteration in the tilting angle of the Weyl cones and the corresponding Lifshitz transition from type-II to type-I WSM. Since the intrinsic

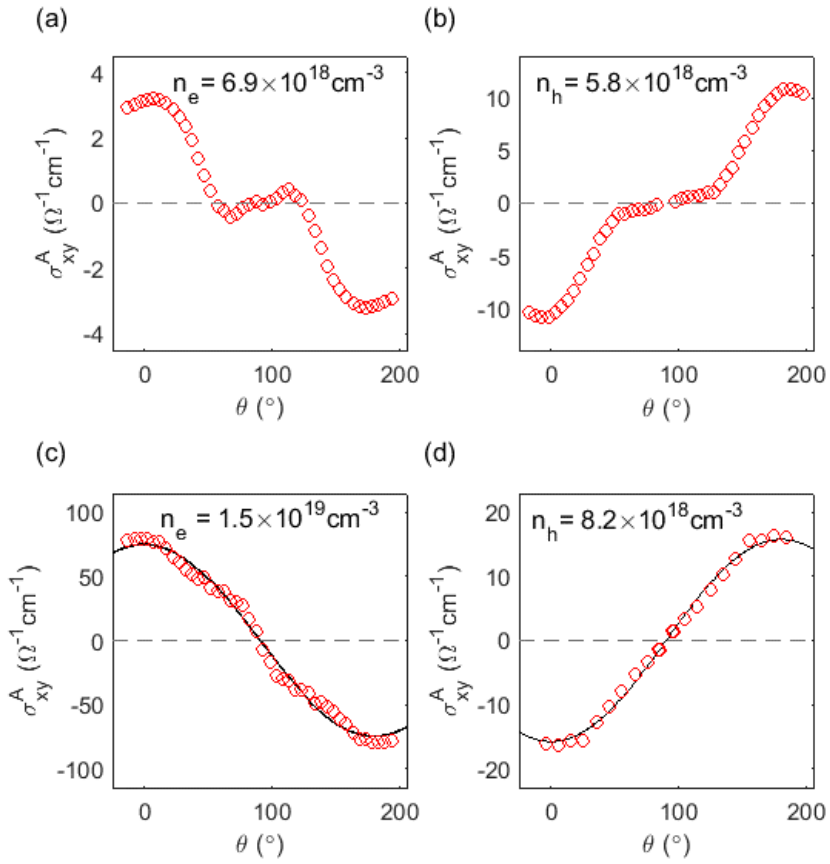

Figure 5.4: **Magnetic field angle dependence of the anomalous Hall conductivity of $MnBi_{2-x}Sb_xTe_4$.** (a)-(d) Anomalous Hall conductivity of $MnBi_{2-x}Sb_xTe_4$ measured under a DC magnetic field of 14T with different magnetic field angles ($\theta = 0°$ denotes B // c axis whereas $\theta = 90°$ represents B // ab plane) at different doping levels (a) slightly electron-doped (b) slightly hole-doped (c) heavily electron-doped (d) heavily hole-doped samples. While the AHC of heavily-doped samples shows a general trend of a trivial cosine dependence as the magnetic field angle rotates away from the c axis, the AHC of samples closer to the critical doping shows an anomalous magnetic field angle dependence. A zigzag behavior is observed in both electron and hole-doped samples with a similar turning point near $\theta = 60°$. Furthermore, the AHC of the slightly electron-doped sample undergoes an anomalous sign change near $\theta = 55°$.

AHC of an ideal type-I WSM relies solely on the Weyl node separation, whereas that of an ideal type-II WSM is influenced by the detailed electronic structures (i.e., the tilting angle of the Weyl cone C), a turning point is anticipated in the magnetic field angle dependence

of the AHC. This turning point marks an abrupt change in angle dependence before and after the Lifshitz transition occurs. Fig. 5.1(e) illustrates the angle dependence of the AHC, taking into account all three factors with a hypothetical Lifshitz transition near $\theta = 60°$ based on Eq. 1.57.

Figure 5.4 presents the dependence of the Anomalous Hall Conductance (AHC) on the magnetic field angle for four distinct $MnBi_{2-x}Sb_xTe_4$ samples with varying carrier densities. In samples with lower carrier densities, an abrupt change is observed near $\theta = 60°$, aligning qualitatively with the Lifshitz transition scenario depicted in Figure 5.1(e). For the sample in Figure 5.4(a), a sign change is detected near $\theta = 55°$, which cannot be comprehended without considering a topological phase transition. For heavily doped samples, as shown in Figure 5.4(c)-(d), the angular dependence can be approximated by a cosine function. This observation can be attributed to the diminishing dominance of the intrinsic AHC contribution from the Weyl nodes as the system moves away from the Weyl points.

5.4 Conclusion and discussion

In conclusion, we have achieved an in-situ controlled type-II to type-I Weyl semimetal transition using the magnetic field angle as a tuning knob. Our results demonstrate anomalous angular dependencies of quantum oscillations and high-field Hall resistivity for samples near the Weyl nodes, consistent with the scenario of a type-II to type-I WSM Lifshitz transition. The anomalous Hall conductivity also exhibits an abrupt turning point as a function of the magnetic field angle, which is unexplainable without considering the Lifshitz transition. These findings offer new insights into the interplay between magnetism and band topology in $MnBi_{2-x}Sb_xTe_4$ and illuminate the design and control of topological materials using the straightforward knob of the magnetic field.

Chapter 6

TUNING MAGNETIC PROPERTIES AND ELECTRONIC STRUCTURES OF $MnBi_{2-x}Sb_xTe_4$ BY HYDROSTATIC PRESSURE

6.1 Abstract

Hydrostatic pressure is a widely-used and powerful technique to tune the electronic structure and magnetic behavior of a material, as it adjusts the crystal lattice and the strength of interactions. In this chapter, we investigate the effect of hydrostatic pressure on the electronic and magnetic properties of FM $MnBi_{2-x}Sb_xTe_4$. As discussed in previous chapters, this material exhibits an ideal type-II Weyl semimetal phase under ambient pressure, accompanied by interlayer antiferromagnetic coupling and intralayer ferromagnetic coupling that favor an A-type AFM ground state. By applying external pressure, we observe a slight increase in the lower critical field H_{c1}, indicating an enhanced AFM interlayer exchange coupling induced by pressure. Furthermore, we detect a noticeable secondary Shubnikov-de Haas oscillation frequency and an abrupt change in the anomalous Hall resistivity when the pressure reaches 1 GPa. These phenomena are potentially associated with the formation of a new pair of Weyl nodes near the Z point, as suggested by density functional theory calculations.

6.2 Introduction

As introduced in previous chapters, $MnBi_{2-x}Sb_xTe_4$ attracts significant interest due to its unique combination of properties, including the potential to accommodate distinct topological phases and rich magnetism [14, 17]. This material exhibits an intriguing interplay between interlayer AFM coupling and intralayer FM coupling, resulting in an A-type AFM ground state [84]. As applying an out-of-plane magnetic field, we have demonstrated that in the field-induced FM state, this material becomes an ideal type-II Weyl semimetal. The coexistence of tunable magnetic orders and the Weyl semimetal phase provides an exciting

platform for studying emergent phenomena and tailoring material properties, particularly under hydrostatic pressure [82, 85, 86]. Hydrostatic pressure is an extensively employed and potent method that allows for the manipulation of the crystal lattice and the strength of interactions. It provides the means to exert control over the electronic structure and magnetic properties of materials.

The application of external pressure influences the magnetic behavior of $MnBi_{2-x}Sb_xTe_4$ by modifying its exchange coupling strength. Under ambient pressure, the interlayer AFM interaction in $MnBi_2Te_4$ arises from long-range superexchange coupling mediated by p orbitals [82]. When pressure is applied, the interlayer AFM interaction is expected to be enhanced due to a decrease in interlayer distances and an increase in interlayer orbital hybridization.

Furthermore, hydrostatic pressure is also expected to impact the electronic structure of $MnBi_{2-x}Sb_xTe_4$ through changes in the crystal lattice and magnetism. Density functional theory calculations suggest that increasing pressure causes the type-II Weyl nodes to approach each other, and more significantly the emergence of a new pair of type-I Weyl nodes above the original pair in Fermi energy near 1 GPa [82]. With further increased pressure, the type-I Weyl nodes move closer to the type-II Weyl nodes in the Fermi energy. Ultimately, the type-II Weyl nodes annihilate near 2 GPa, and the type-I Weyl nodes undergoes a Lifshitz transition into type-II nodes at around 5 GPa.

In this chapter, we investigate the response of FM $MnBi_{2-x}Sb_xTe_4$ to hydrostatic pressure. By subjecting the material to various pressure conditions, we aim to elucidate the effects of pressure on its electronic structure and magnetic properties, with a particular focus on the possible creation of new pairs of Weyl nodes facilitated by hydrostatic pressure.

6.3 Results

We applied an external pressure and concurrently measured the transport properties of an electron-doped $MnBi_{2-x}Sb_xTe_4$ (x = 0.64), as detailed in Chapter 2. Fig. 6.1(a) illustrate the temperature dependence of resistivity under various pressure. As the pressure increases, the resistivity decreases, which is possibly associated with increased carrier density and mobility under pressure. The AFM transition remains largely unaffected, while

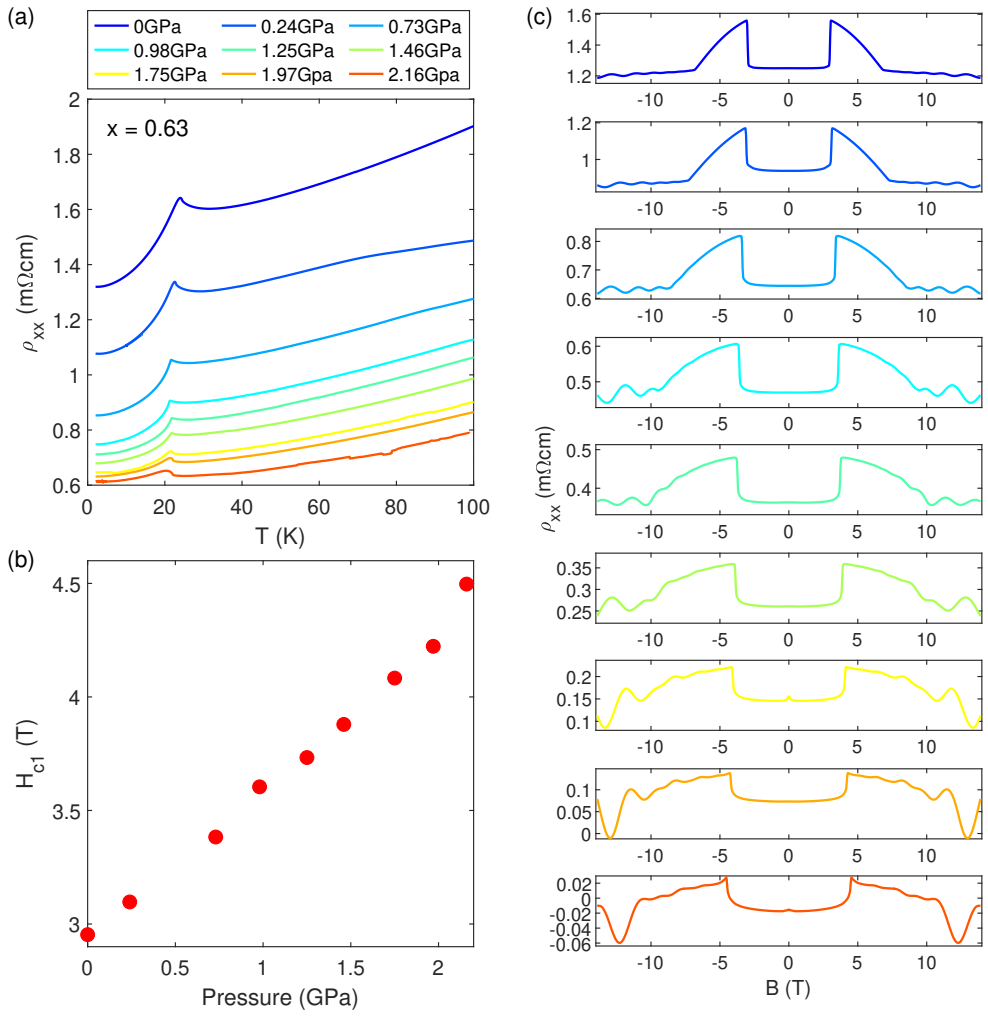

Figure 6.1: **Pressure dependence of transport properties of $MnBi_{2-x}Sb_xTe_4$ (x = 0.63).** (a) Resistivity as a function of temperature of $MnBi_{2-x}Sb_xTe_4(x = 0.63)$ measured under varied external pressure (color-coded). (b) Pressure dependence of the lower critical field H_{c1}. (c) Magnetoresistivity as a function of magnetic field B under varied external pressure represented by distinct colors.

the lower critical field H_{c1} extracted from the abrupt change in magnetoresistivity near 3T in Fig. 6.1(c) slightly increases with pressure (Fig. 6.1(b)). Since the lower critical field

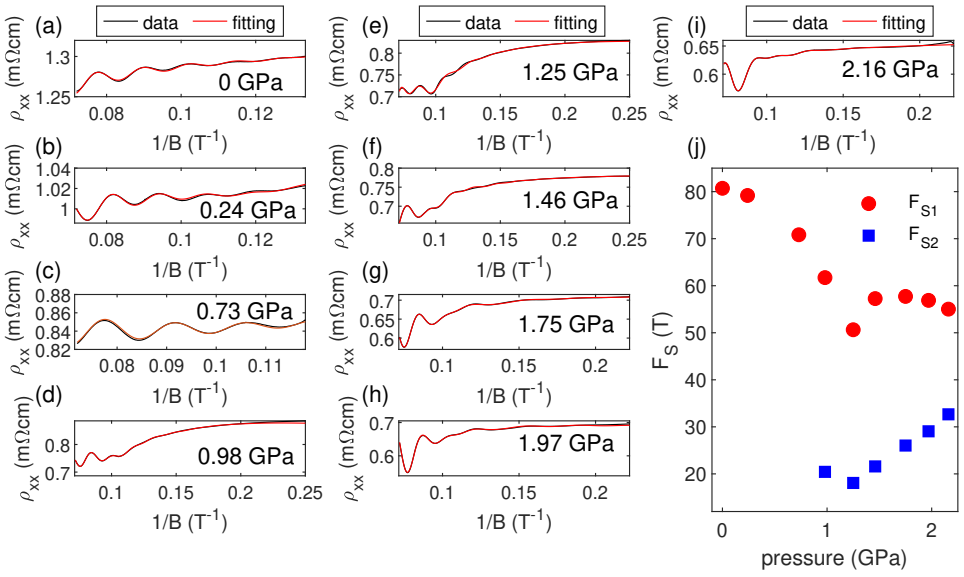

Figure 6.2: **Pressure dependence of Shubnikov-de Haas oscillations of $MnBi_{2-x}Sb_xTe_4$ (x = 0.63).** (a) - (i) Experimental data and analytical fitting of the SdH oscillations along with the magnetoresistivity background under various pressure. The black line represents the experimental data, whereas the red line represents the fitting curve. (j) Oscillation frequencies extracted from the fitting as a function of applied pressure.

of a spin-flop transition is determined by the exchange coupling strength J_c and single-ion anisotropy D through $H_{c1} = 2SD\sqrt{z|J_c|/D - 1}$, our observation indicates the interlayer exchange coupling strength J_c is enhanced compared to the single-ion anisotropy D. This is consistent with DFT calculations, where the out-of-plane exchange coupling J_c was found to increase rapidly with increasing pressure, while the anisotropy energy showed minimal changes within the pressure range we applied [82].

Moreover, significant changes in magnetotransport properties were observed as the pressure increased (Figure 6.1(c)). For pressures below 1 GPa, oscillation signals appeared when the out-of-plane magnetic field exceeded the upper critical field ($H_{c2} \sim 7$T), displaying a single-frequency oscillation pattern up to 14T. With further pressure increase, the abrupt turn in MR near the upper critical field became less noticeable, and the oscillations appeared whenever the external field exceeded the lower critical field near 3T. Notably, a beating effect of quantum oscillations was observed in the magnetoresistivity measurements

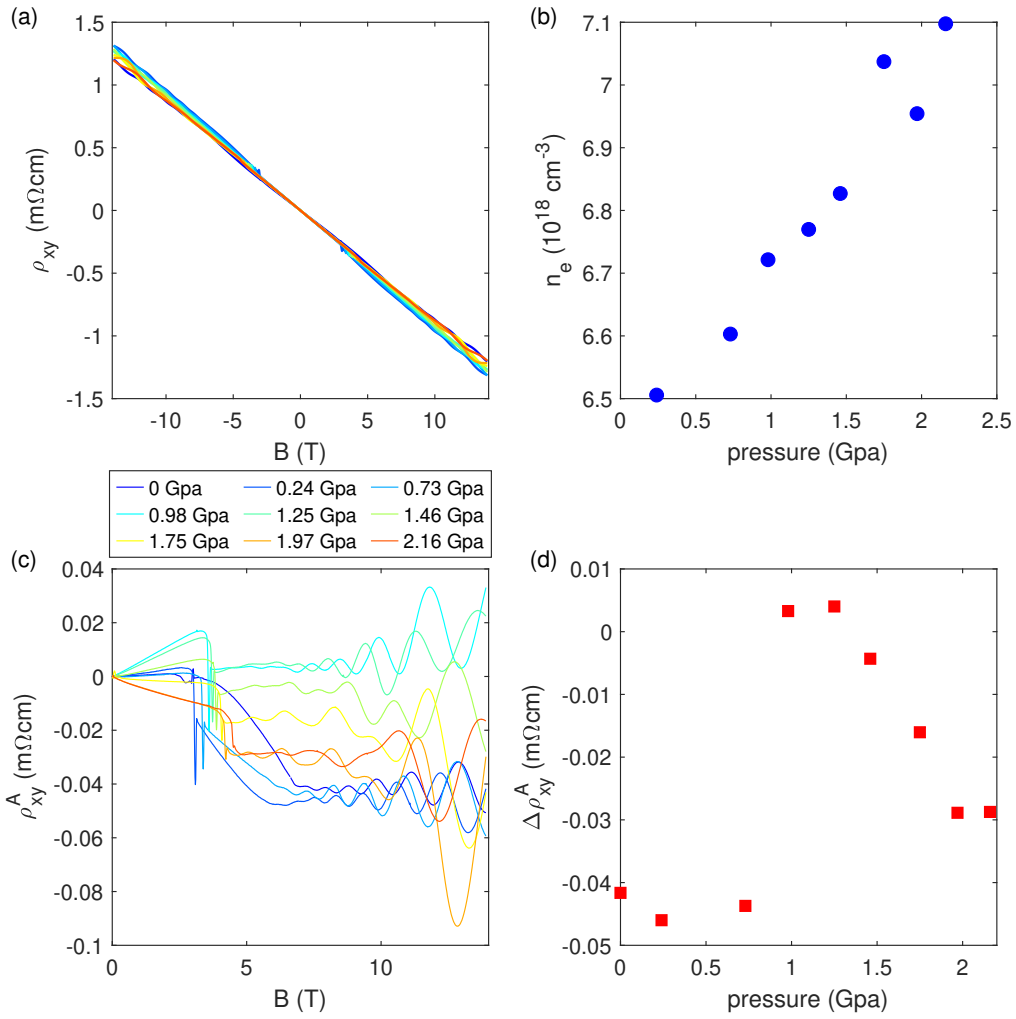

Figure 6.3: **Pressure dependence of Hall effect of $MnBi_{2-x}Sb_xTe_4$ (x = 0.63).** (a) Hall resistivity as a function of magnetic field under varied external pressure (b) Pressure dependence of the carrier density extracted by fitting the linear slope of Hall resistivity above H_{c2}. (c) Anomalous Hall resistivity as a function of magnetic field under various external pressure. (b) Pressure dependence of anomalous Hall resistivity.

under pressures greater than 1 GPa. To analyze the effect of pressure on the SdH oscillations, the oscillatory data was analytically fitted to the two-frequency Lifshitz-Kosevich

formula along with the magnetoresistivity background. Figures 6.2(a)-(i) demonstrate the successful capture of oscillation features under different pressures. The pressure dependence of the oscillation frequencies, summarized in Figure 6.2(j), revealed a decrease in the major frequency from 80T to 55T, while a secondary frequency emerged or became visible near 1 GPa, with the frequency increasing from 20T to 33T. This observation suggests the possible emergence of a Fermi pocket under pressure.

In addition to the pressure dependence of SdH oscillations, the pressure dependence of Hall resistivity is analyzed to gain further insight into the effect of pressure on the electronic structure of FM $MnBi_{2-x}Sb_xTe_4$. The Hall resistivity remain linear up to 14T under various pressures (Fig. 6.3(a)), and the carrier density exhibit only a moderate increase with pressure (Fig. 6.3(b)), which can be well explained by the decrease in the unit cell volume under pressure. However, the anomalous Hall resistivity exhibit an abrupt change near 1 Gpa, accompanied by a sign change (Fig. 6.3 (c)-(d)). A similar pressure region also witness the visibility of a secondary frequency in SdH oscillations, suggesting a potential Lifshitz transition where a new pair of type-I Weyl nodes merges, as proposed by DFT calculations [82].

6.4 Conclusion

In conclusion, our study highlights the effectiveness of hydrostatic pressure as a powerful tool for tuning the electronic and magnetic properties of $MnBi_{2-x}Sb_xTe_4$. The observed changes in the lower critical field, Shubnikov-de Haas oscillations, and anomalous Hall resistivity suggest pressure-induced modifications in the material's magnetic and electronic behavior. The potential formation of a new pair of Weyl nodes near the Z point under pressure offers exciting prospects for investigating the extended topological aspects of this material. These findings contribute to a deeper understanding of the interplay between hydrostatic pressure, electronic structure, and magnetic properties in FM $MnBi_{2-x}Sb_xTe_4$.

Chapter 7

SUMMARY AND OUTLOOK

It is widely acknowledged that the study of topological materials is of great significance as it offers a platform to explore exotic quantum phenomena, gain insights into fundamental properties of matter, and potentially revolutionize various applications, including electronics and quantum computing. The emergence of magnetic topological materials has provided a remarkable opportunity to realize topological materials and topological phase transitions with an easily tunable and versatile degree of freedom: magnetism. The major effort of this thesis is to obtain a comprehensive understanding of the electronic structures and their interplay with magnetism in the intrinsic magnetic topological material $MnBi_{2-x}Sb_xTe_4$.

The thesis employs a combination of techniques to investigate this material, starting with the use of quantum oscillations as a probe to study the electronic structure in the field-induced ferromagnetic state. By tuning the chemical potential through Sb substitution and combining it with high-field Hall measurements, we successfully identify the field-induced ferromagnetic $MnBi_{2-x}Sb_xTe_4$ as a long-sought ideal type-II Weyl semimetal. Remarkably, we observe a unique behavior in the anomalous Hall conductivity that exhibits a singular, heartbeat-like pattern as the Fermi level is tuned across the Weyl nodes, consistent with theoretical predictions for a type-II Weyl semimetal..

Additionally, in this study, an in-situ controlled Lifshitz transition from a type-II Weyl semimetal to a type-I Weyl semimetal is realized by rotating the magnetic field angle. This discovery highlights the versatility and tunability of $MnBi_{2-x}Sb_xTe_4$ and provides insights into the intricate interplay between magnetism and electronic structure.

Furthermore, the impact of external factors on the electronic structures and magnetic properties of $MnBi_{2-x}Sb_xTe_4$ is explored. Specifically, the effect of hydrostatic pressure is investigated, revealing extreme sensitivity and the potential creation of a new pair of Weyl nodes in response to external pressure. This finding underscores the remarkable tunability of

$MnBi_{2-x}Sb_xTe_4$ and broadens our understanding of its electronic and topological properties.

Overall, the research conducted in this thesis deepens the understanding of Weyl semimetals through a comprehensive study of an ideal Weyl semimetal state in field-induced FM $MnBi_{2-x}Sb_xTe_4$ and its associated Lifshitz transitions under external fields. The findings offer valuable insights into the interplay between electronic structures and magnetism, highlighting the exceptional properties of $MnBi_{2-x}Sb_xTe_4$ as an invaluable platform for further investigations in Weyl physics. Furthermore, the research opens up exciting prospects for future studies on magnetic topological materials and external-field-controlled Lifshitz transitions. In particular, the realization of an ideal Weyl semimetal with a ferromagnetic ground state in a related materials system, such as Sb-doped $MnBi_{2n}Te_{3n+1}$, holds immense significance. This achievement will enable diverse studies on an ideal WSM without the need for an external field, making investigations into exotic properties associated with Fermi arcs and chiral anomalies more feasible. Furthermore, the combined experimental methods employed in this thesis, including high-field quantum oscillation measurements, high-field Hall measurements, and anomalous Hall analysis as a function of chemical doping under external fields, constitute a self-contained toolkit for exploring other Weyl candidates, such as half-Heusler compounds RBiPt (R = Gd, Yb, Nd) and Eu-based magnetic topological materials $Eu(Cd,In)_2(As,Sb)_2$.

BIBLIOGRAPHY

[1] 1967 Blundell, Stephen. *Magnetism in condensed matter*. Oxford ; New York : Oxford University Press, 2001., 2001. Includes bibliographical references and index.

[2] Di Xiao, Wang Yao, and Qian Niu. Valley-contrasting physics in graphene: Magnetic moment and topological transport. *Phys. Rev. Lett.*, 99:236809, Dec 2007.

[3] A. A. Burkov. Anomalous hall effect in weyl metals. *Phys. Rev. Lett.*, 113:187202, Oct 2014.

[4] K. v. Klitzing, G. Dorda, and M. Pepper. New method for high-accuracy determination of the fine-structure constant based on quantized hall resistance. *Phys. Rev. Lett.*, 45:494–497, Aug 1980.

[5] S.M. Girvin and K. Yang. *Modern Condensed Matter Physics*. Cambridge University Press, 2019.

[6] M. Z. Hasan and C. L. Kane. Colloquium: Topological insulators. *Rev. Mod. Phys.*, 82:3045–3067, Nov 2010.

[7] Yoshinori Tokura, Kenji Yasuda, and Atsushi Tsukazaki. Magnetic topological insulators. *Nature Reviews Physics*, 1(2):126–143, Feb 2019.

[8] Cui-Zu Chang, Jinsong Zhang, Xiao Feng, Jie Shen, Zuocheng Zhang, Minghua Guo, Kang Li, Yunbo Ou, Pang Wei, Li-Li Wang, Zhong-Qing Ji, Yang Feng, Shuaihua Ji, Xi Chen, Jinfeng Jia, Xi Dai, Zhong Fang, Shou-Cheng Zhang, Ke He, Yayu Wang, Li Lu, Xu-Cun Ma, and Qi-Kun Xue. Experimental observation of the quantum anomalous hall effect in a magnetic topological insulator. *Science*, 340(6129):167–170, 2013.

[9] Masataka Mogi, Minoru Kawamura, Atsushi Tsukazaki, Ryutaro Yoshimi, Kei S. Takahashi, Masashi Kawasaki, and Yoshinori Tokura. Tailoring tricolor structure of magnetic topological insulator for robust axion insulator. *Science Advances*, 3(10):eaao1669, 2017.

[10] N. P. Armitage, E. J. Mele, and Ashvin Vishwanath. Weyl and dirac semimetals in three-dimensional solids. *Rev. Mod. Phys.*, 90:015001, Jan 2018.

[11] Z. K. Liu, L. X. Yang, Y. Sun, T. Zhang, H. Peng, H. F. Yang, C. Chen, Y. Zhang, Y. F. Guo, D. Prabhakaran, M. Schmidt, Z. Hussain, S.-K. Mo, C. Felser, B. Yan,

and Y. L. Chen. Evolution of the fermi surface of weyl semimetals in the transition metal pnictide family. *Nature Materials*, 15(1):27–31, Jan 2016.

[12] Jun Xiong, Satya K. Kushwaha, Tian Liang, Jason W. Krizan, Max Hirschberger, Wudi Wang, R. J. Cava, and N. P. Ong. Evidence for the chiral anomaly in the dirac semimetal Na_3Bi. *Science*, 350(6259):413–416, 2015.

[13] A. A. Zyuzin and R. P. Tiwari. Intrinsic anomalous hall effect in type-ii weyl semimetals. *JETP Letters*, 103(11):717–722, Jun 2016.

[14] Jiaheng Li, Yang Li, Shiqiao Du, Zun Wang, Bing-Lin Gu, Shou-Cheng Zhang, Ke He, Wenhui Duan, and Yong Xu. Intrinsic magnetic topological insulators in van der waals layered $MnBi_2Te_4$-family materials. *Science Advances*, 5(6):eaaw5685, 2019.

[15] Yujun Deng, Yijun Yu, Meng Zhu Shi, Zhongxun Guo, Zihan Xu, Jing Wang, Xian Hui Chen, and Yuanbo Zhang. Quantum anomalous hall effect in intrinsic magnetic topological insulator $MnBi_2Te_4$. *Science*, 367(6480):895–900, 2020.

[16] Chang Liu, Yongchao Wang, Hao Li, Yang Wu, Yaoxin Li, Jiaheng Li, Ke He, Yong Xu, Jinsong Zhang, and Yayu Wang. Robust axion insulator and chern insulator phases in a two-dimensional antiferromagnetic topological insulator. *Nature Materials*, 19(5):522–527, May 2020.

[17] Dongqin Zhang, Minji Shi, Tongshuai Zhu, Dingyu Xing, Haijun Zhang, and Jing Wang. Topological axion states in the magnetic insulator $MnBi_2Te_4$ with the quantized magnetoelectric effect. *Phys. Rev. Lett.*, 122:206401, May 2019.

[18] Zhiming Xu, Meng Ye, Jiaheng Li, Wenhui Duan, and Yong Xu. Hydrostatic pressure-induced magnetic and topological phase transitions in the $MnBi_2Te_4$ family of materials. *Phys. Rev. B*, 105:085129, Feb 2022.

[19] Masatoshi Sato and Yoichi Ando. Topological superconductors: a review. *Reports on Progress in Physics*, 80(7):076501, may 2017.

[20] Di Xiao, Ming-Che Chang, and Qian Niu. Berry phase effects on electronic properties. *Rev. Mod. Phys.*, 82:1959–2007, Jul 2010.

[21] A. Bansil, Hsin Lin, and Tanmoy Das. Colloquium: Topological band theory. *Rev. Mod. Phys.*, 88:021004, Jun 2016.

[22] Michael Victor Berry. Quantal phase factors accompanying adiabatic changes. *Proceedings of the Royal Society of London. A. Mathematical and Physical Sciences*, 392(1802):45–57, 1984.

[23] K. v. Klitzing, G. Dorda, and M. Pepper. New method for high-accuracy determination of the fine-structure constant based on quantized hall resistance. *Phys. Rev. Lett.*, 45:494–497, Aug 1980.

[24] D. J. Thouless, M. Kohmoto, M. P. Nightingale, and M. den Nijs. Quantized hall conductance in a two-dimensional periodic potential. *Phys. Rev. Lett.*, 49:405–408, Aug 1982.

[25] C. L. Kane and E. J. Mele. Quantum spin hall effect in graphene. *Phys. Rev. Lett.*, 95:226801, Nov 2005.

[26] Liang Fu and C. L. Kane. Time reversal polarization and a Z_2 adiabatic spin pump. *Phys. Rev. B*, 74:195312, Nov 2006.

[27] B. Andrei Bernevig, Taylor L. Hughes, and Shou-Cheng Zhang. Quantum spin hall effect and topological phase transition in HgTe quantum wells. *Science*, 314(5806):1757–1761, 2006.

[28] Markus König, Steffen Wiedmann, Christoph Brüne, Andreas Roth, Hartmut Buhmann, Laurens W. Molenkamp, Xiao-Liang Qi, and Shou-Cheng Zhang. Quantum spin hall insulator state in HgTe quantum wells. *Science*, 318(5851):766–770, 2007.

[29] Xiaofeng Qian, Junwei Liu, Liang Fu, and Ju Li. Quantum spin hall effect in two-dimensional transition metal dichalcogenides. *Science*, 346(6215):1344–1347, 2014.

[30] Shujie Tang, Chaofan Zhang, Dillon Wong, Zahra Pedramrazi, Hsin-Zon Tsai, Chunjing Jia, Brian Moritz, Martin Claassen, Hyejin Ryu, Salman Kahn, Juan Jiang, Hao Yan, Makoto Hashimoto, Donghui Lu, Robert G. Moore, Chan-Cuk Hwang, Choongyu Hwang, Zahid Hussain, Yulin Chen, Miguel M. Ugeda, Zhi Liu, Xiaoming Xie, Thomas P. Devereaux, Michael F. Crommie, Sung-Kwan Mo, and Zhi-Xun Shen. Quantum spin hall state in monolayer 1T'-WTe_2. *Nature Physics*, 13(7):683–687, Jul 2017.

[31] Zaiyao Fei, Tauno Palomaki, Sanfeng Wu, Wenjin Zhao, Xinghan Cai, Bosong Sun, Paul Nguyen, Joseph Finney, Xiaodong Xu, and David H. Cobden. Edge conduction in monolayer WTe_2. *Nature Physics*, 13(7):677–682, Jul 2017.

[32] Sanfeng Wu, Valla Fatemi, Quinn D. Gibson, Kenji Watanabe, Takashi Taniguchi, Robert J. Cava, and Pablo Jarillo-Herrero. Observation of the quantum spin hall effect up to 100 kelvin in a monolayer crystal. *Science*, 359(6371):76–79, 2018.

[33] D. Hsieh, Y. Xia, D. Qian, L. Wray, J. H. Dil, F. Meier, J. Osterwalder, L. Patthey, J. G. Checkelsky, N. P. Ong, A. V. Fedorov, H. Lin, A. Bansil, D. Grauer, Y. S. Hor, R. J. Cava, and M. Z. Hasan. A tunable topological insulator in the spin helical dirac transport regime. *Nature*, 460(7259):1101–1105, Aug 2009.

[34] Y. Xia, D. Qian, D. Hsieh, L. Wray, A. Pal, H. Lin, A. Bansil, D. Grauer, Y. S. Hor, R. J. Cava, and M. Z. Hasan. Observation of a large-gap topological-insulator class with a single dirac cone on the surface. *Nature Physics*, 5(6):398–402, Jun 2009.

[35] Y. L. Chen, J. G. Analytis, J.-H. Chu, Z. K. Liu, S.-K. Mo, X. L. Qi, H. J. Zhang, D. H. Lu, X. Dai, Z. Fang, S. C. Zhang, I. R. Fisher, Z. Hussain, and Z.-X. Shen. Experimental realization of a three-dimensional topological insulator, Bi_2Te_3. *Science*, 325(5937):178–181, 2009.

[36] D. Hsieh, Y. Xia, D. Qian, L. Wray, F. Meier, J. H. Dil, J. Osterwalder, L. Patthey, A. V. Fedorov, H. Lin, A. Bansil, D. Grauer, Y. S. Hor, R. J. Cava, and M. Z. Hasan. Observation of time-reversal-protected single-dirac-cone topological-insulator states in Bi_2Te_3 and Sb_2Te_3. *Phys. Rev. Lett.*, 103:146401, Sep 2009.

[37] Haijun Zhang, Chao-Xing Liu, Xiao-Liang Qi, Xi Dai, Zhong Fang, and Shou-Cheng Zhang. Topological insulators in Bi_2Se_3, Bi_2Te_3 and Sb_2Te_3 with a single dirac cone on the surface. *Nature Physics*, 5(6):438–442, Jun 2009.

[38] Satoshi Sasaki, M. Kriener, Kouji Segawa, Keiji Yada, Yukio Tanaka, Masatoshi Sato, and Yoichi Ando. Topological superconductivity in $Cu_xBi_2Se_3$. *Phys. Rev. Lett.*, 107:217001, Nov 2011.

[39] Cui-Zu Chang, Chao-Xing Liu, and Allan H. MacDonald. Colloquium: Quantum anomalous hall effect. *Rev. Mod. Phys.*, 95:011002, Jan 2023.

[40] Cui-Zu Chang, Weiwei Zhao, Duk Y. Kim, Haijun Zhang, Badih A. Assaf, Don Heiman, Shou-Cheng Zhang, Chaoxing Liu, Moses H. W. Chan, and Jagadeesh S. Moodera. High-precision realization of robust quantum anomalous hall state in a hard ferromagnetic topological insulator. *Nature Materials*, 14(5):473–477, May 2015.

[41] Dennis M. Nenno, Christina A. C. Garcia, Johannes Gooth, Claudia Felser, and Prineha Narang. Axion physics in condensed-matter systems. *Nature Reviews Physics*, 2(12):682–696, Dec 2020.

[42] Shuichi Murakami. Phase transition between the quantum spin hall and insulator phases in 3d: emergence of a topological gapless phase. *New Journal of Physics*, 9(9):356, sep 2007.

[43] P. A. M. Dirac. The quantum theory of the electron. *Proceedings of the Royal Society of London. Series A, Containing Papers of a Mathematical and Physical Character*, 117(778):610–624, 2023/05/29/ 1928. Full publication date: Feb. 1, 1928.

[44] D. T. Son and B. Z. Spivak. Chiral anomaly and classical negative magnetoresistance of weyl metals. *Phys. Rev. B*, 88:104412, Sep 2013.

[45] Dmitry Ovchinnikov, Xiong Huang, Zhong Lin, Zaiyao Fei, Jiaqi Cai, Tiancheng Song, Minhao He, Qianni Jiang, Chong Wang, Hao Li, Yayu Wang, Yang Wu, Di Xiao, Jiun-Haw Chu, Jiaqiang Yan, Cui-Zu Chang, Yong-Tao Cui, and Xiaodong Xu. Intertwined topological and magnetic orders in atomically thin chern insulator $MnBi_2Te_4$.

[46] Jiaheng Li Hao Li Tianchuang Luo Yang Wu Yong Xu Jian Wang Jun Ge, Yanzhao Liu. High-chern-number and high-temperature quantum hall effect without landau levels. *National Science Review*, 7(8):1280–1287, 2020.

[47] Jiaqi Cai, Dmitry Ovchinnikov, Zaiyao Fei, Minhao He, Tiancheng Song, Zhong Lin, Chong Wang, David Cobden, Jiun-Haw Chu, Yong-Tao Cui, Cui-Zu Chang, Di Xiao, Jiaqiang Yan, and Xiaodong Xu. Electric control of a canted-antiferromagnetic chern insulator. *Nature Communications*, 13(1):1668, Mar 2022.

[48] Yang Peng and Yong Xu. Proximity-induced majorana hinge modes in antiferromagnetic topological insulators. *Phys. Rev. B*, 99:195431, May 2019.

[49] Rui-Xing Zhang, Fengcheng Wu, and S. Das Sarma. Möbius insulator and higher-order topology in $MnBi_{2n}Te_{3n+1}$. *Phys. Rev. Lett.*, 124:136407, Apr 2020.

[50] J.-Q. Yan, S. Okamoto, M. A. McGuire, A. F. May, R. J. McQueeney, and B. C. Sales. Evolution of structural, magnetic, and transport properties in $MnBi_{2-x}Sb_xTe_4$. *Phys. Rev. B*, 100:104409, Sep 2019.

[51] M. M. Otrokov, I. I. Klimovskikh, H. Bentmann, D. Estyunin, A. Zeugner, Z. S. Aliev, S. Gaß, A. U. B. Wolter, A. V. Koroleva, A. M. Shikin, M. Blanco-Rey, M. Hoffmann, I. P. Rusinov, A. Yu. Vyazovskaya, S. V. Eremeev, Yu. M. Koroteev, V. M. Kuznetsov, F. Freyse, J. Sánchez-Barriga, I. R. Amiraslanov, M. B. Babanly, N. T. Mamedov, N. A. Abdullayev, V. N. Zverev, A. Alfonsov, V. Kataev, B. Büchner, E. F. Schwier, S. Kumar, A. Kimura, L. Petaccia, G. Di Santo, R. C. Vidal, S. Schatz, K. Kißner, M. Ünzelmann, C. H. Min, Simon Moser, T. R. F. Peixoto, F. Reinert, A. Ernst, P. M. Echenique, A. Isaeva, and E. V. Chulkov. Prediction and observation of an antiferromagnetic topological insulator. *Nature*, 576(7787):416–422, Dec 2019.

[52] Yan Gong, Jingwen Guo, Jiaheng Li, Kejing Zhu, Menghan Liao, Xiaozhi Liu, Qinghua Zhang, Lin Gu, Lin Tang, Xiao Feng, Ding Zhang, Wei Li, Canli Song, Lili Wang, Pu Yu, Xi Chen, Yayu Wang, Hong Yao, Wenhui Duan, Yong Xu, Shou-Cheng Zhang, Xucun Ma, Qi-Kun Xue, and Ke He. Experimental realization of an intrinsic magnetic topological insulator. *Chinese Physics Letters*, 36(7):076801, jun 2019.

[53] Jun Ge, Yanzhao Liu, Jiaheng Li, Hao Li, Tianchuang Luo, Yang Wu, Yong Xu, and Jian Wang. High-Chern-number and high-temperature quantum Hall effect without Landau levels. *National Science Review*, 7(8):1280–1287, 04 2020.

[54] Hang Li, Shun-Ye Gao, Shao-Feng Duan, Yuan-Feng Xu, Ke-Jia Zhu, Shang-Jie Tian, Jia-Cheng Gao, Wen-Hui Fan, Zhi-Cheng Rao, Jie-Rui Huang, Jia-Jun Li, Da-Yu Yan, Zheng-Tai Liu, Wan-Ling Liu, Yao-Bo Huang, Yu-Liang Li, Yi Liu, Guo-Bin Zhang, Peng Zhang, Takeshi Kondo, Shik Shin, He-Chang Lei, You-Guo Shi, Wen-Tao Zhang, Hong-Ming Weng, Tian Qian, and Hong Ding. Dirac surface states in intrinsic magnetic topological insulators $EuSn_2As_2$ and $MnBi_{2n}Te_{3n+1}$. *Phys. Rev. X*, 9:041039, Nov 2019.

[55] Y. J. Chen, L. X. Xu, J. H. Li, Y. W. Li, H. Y. Wang, C. F. Zhang, H. Li, Y. Wu, A. J. Liang, C. Chen, S. W. Jung, C. Cacho, Y. H. Mao, S. Liu, M. X. Wang, Y. F. Guo, Y. Xu, Z. K. Liu, L. X. Yang, and Y. L. Chen. Topological electronic structure and its temperature evolution in antiferromagnetic topological insulator $MnBi_2Te_4$. *Phys. Rev. X*, 9:041040, Nov 2019.

[56] Yu-Jie Hao, Pengfei Liu, Yue Feng, Xiao-Ming Ma, Eike F. Schwier, Masashi Arita, Shiv Kumar, Chaowei Hu, Rui'e Lu, Meng Zeng, Yuan Wang, Zhanyang Hao, Hong-Yi Sun, Ke Zhang, Jiawei Mei, Ni Ni, Liusuo Wu, Kenya Shimada, Chaoyu Chen, Qihang Liu, and Chang Liu. Gapless surface dirac cone in antiferromagnetic topological insulator $MnBi_2Te_4$. *Phys. Rev. X*, 9:041038, Nov 2019.

[57] Przemyslaw Swatek, Yun Wu, Lin-Lin Wang, Kyungchan Lee, Benjamin Schrunk, Jiaqiang Yan, and Adam Kaminski. Gapless dirac surface states in the antiferromagnetic topological insulator $MnBi_2Te_4$. *Phys. Rev. B*, 101:161109, Apr 2020.

[58] Bo Chen, Fucong Fei, Dongqin Zhang, Bo Zhang, Wanling Liu, Shuai Zhang, Pengdong Wang, Boyuan Wei, Yong Zhang, Zewen Zuo, Jingwen Guo, Qianqian Liu, Zilu Wang, Xuchuan Wu, Junyu Zong, Xuedong Xie, Wang Chen, Zhe Sun, Shancai Wang, Yi Zhang, Minhao Zhang, Xuefeng Wang, Fengqi Song, Haijun Zhang, Dawei Shen, and Baigeng Wang. Intrinsic magnetic topological insulator phases in the Sb doped $MnBi_2Te_4$ bulks and thin flakes. *Nature Communications*, 10(1):4469, Oct 2019.

[59] Xiao-Ming Ma, Yufei Zhao, Ke Zhang, Shiv Kumar, Ruie Lu, Jiayu Li, Qiushi Yao, Jifeng Shao, Fuchen Hou, Xuefeng Wu, Meng Zeng, Yu-Jie Hao, Zhanyang Hao, Yuan Wang, Xiang-Rui Liu, Huiwen Shen, Hongyi Sun, Jiawei Mei, Koji Miyamoto, Taichi Okuda, Masashi Arita, Eike F. Schwier, Kenya Shimada, Ke Deng, Cai Liu, Junhao Lin, Yue Zhao, Chaoyu Chen, Qihang Liu, and Chang Liu. Realization of a tunable surface dirac gap in Sb-doped $MnBi_2Te_4$. *Phys. Rev. B*, 103:L121112, Mar 2021.

[60] D. Nevola, H. X. Li, J.-Q. Yan, R. G. Moore, H.-N. Lee, H. Miao, and P. D. Johnson. Coexistence of surface ferromagnetism and a gapless topological state in $MnBi_2Te_4$. *Phys. Rev. Lett.*, 125:117205, Sep 2020.

[61] Yonghao Yuan, Xintong Wang, Hao Li, Jiaheng Li, Yu Ji, Zhenqi Hao, Yang Wu, Ke He, Yayu Wang, Yong Xu, Wenhui Duan, Wei Li, and Qi-Kun Xue. Electronic states and magnetic response of $MnBi_2Te_4$ by scanning tunneling microscopy and spectroscopy. *Nano Letters*, 20(5):3271–3277, May 2020.

[62] Wonhee Ko, Marek Kolmer, Jiaqiang Yan, Anh D. Pham, Mingming Fu, Felix Lüpke, Satoshi Okamoto, Zheng Gai, P. Ganesh, and An-Ping Li. Realizing gapped surface states in the magnetic topological insulator $MnBi_{2-x}Sb_xTe_4$. *Phys. Rev. B*, 102:115402, Sep 2020.

[63] Seng Huat Lee, David Graf, Lujin Min, Yanglin Zhu, Hemian Yi, Samuel Ciocys, Yuanxi Wang, Eun Sang Choi, Rabindra Basnet, Arash Fereidouni, Aaron Wegner, Yi-Fan Zhao, Katrina Verlinde, Jingyang He, Ronald Redwing, V. Gopalan, Hugh O. H. Churchill, Alessandra Lanzara, Nitin Samarth, Cui-Zu Chang, Jin Hu, and Z. Q. Mao. Evidence for a magnetic-field-induced ideal type-ii weyl state in antiferromagnetic topological insulator $Mn(Bi_{1-x}Sb_x)_2te_4$. *Phys. Rev. X*, 11:031032, Aug 2021.

[64] Jiaheng Li, Chong Wang, Zetao Zhang, Bing-Lin Gu, Wenhui Duan, and Yong Xu. Magnetically controllable topological quantum phase transitions in the antiferromagnetic topological insulator $MnBi_2Te_4$. *Phys. Rev. B*, 100:121103, Sep 2019.

[65] Mao-Hua Du, Jiaqiang Yan, Valentino R. Cooper, and Markus Eisenbach. Tuning fermi levels in intrinsic antiferromagnetic topological insulators mnbi2te4 and mnbi4te7 by defect engineering and chemical doping. *Advanced Functional Materials*, 31(3):2006516, 2021.

[66] Binghai Yan and Claudia Felser. Topological materials: Weyl semimetals. *Annual Review of Condensed Matter Physics*, 8(1):337–354, 2017.

[67] Andrei Bernevig, Hongming Weng, Zhong Fang, and Xi Dai. Recent progress in the study of topological semimetals. *Journal of the Physical Society of Japan*, 87(4):041001, 2018.

[68] Alexey A. Soluyanov, Dominik Gresch, Zhijun Wang, QuanSheng Wu, Matthias Troyer, Xi Dai, and B. Andrei Bernevig. Type-II weyl semimetals. *Nature*, 527(7579):495–498, Nov 2015.

[69] G E Volovik. Exotic lifshitz transitions in topological materials. *Physics-Uspekhi*, 61(1):89, jan 2018.

[70] Jin Hu, Su-Yang Xu, Ni Ni, and Zhiqiang Mao. Transport of topological semimetals. *Annual Review of Materials Research*, 49(1):207–252, 2019.

[71] Qiunan Xu, Enke Liu, Wujun Shi, Lukas Muechler, Jacob Gayles, Claudia Felser, and Yan Sun. Topological surface fermi arcs in the magnetic weyl semimetal $Co_3Sn_2S_2$. *Phys. Rev. B*, 97:235416, Jun 2018.

[72] Linchao Ding, Jahyun Koo, Changjiang Yi, Liangcai Xu, Huakun Zuo, Meng Yang, Youguo Shi, Binghai Yan, Kamran Behnia, and Zengwei Zhu. Quantum oscillations,

magnetic breakdown and thermal hall effect in $Co_3Sn_2S_2$. *Journal of Physics D: Applied Physics*, 54(45):454003, aug 2021.

[73] Enke Liu, Yan Sun, Nitesh Kumar, Lukas Muechler, Aili Sun, Lin Jiao, Shuo-Ying Yang, Defa Liu, Aiji Liang, Qiunan Xu, Johannes Kroder, Vicky Süß, Horst Borrmann, Chandra Shekhar, Zhaosheng Wang, Chuanying Xi, Wenhong Wang, Walter Schnelle, Steffen Wirth, Yulin Chen, Sebastian T. B. Goennenwein, and Claudia Felser. Giant anomalous hall effect in a ferromagnetic kagome-lattice semimetal. *Nature Physics*, 14(11):1125–1131, Nov 2018.

[74] D. F. Liu, A. J. Liang, E. K. Liu, Q. N. Xu, Y. W. Li, C. Chen, D. Pei, W. J. Shi, S. K. Mo, P. Dudin, T. Kim, C. Cacho, G. Li, Y. Sun, L. X. Yang, Z. K. Liu, S. S. P. Parkin, C. Felser, and Y. L. Chen. Magnetic weyl semimetal phase in a kagome; crystal. *Science*, 365(6459):1282–1285, 2019.

[75] Yuanxi Wang. Chemical requirements for stabilizing type-ii weyl points in $MnBi_{2-x}Sb_xTe_4$, 2021.

[76] Dongqin Zhang, Minji Shi, Tongshuai Zhu, Dingyu Xing, Haijun Zhang, and Jing Wang. Topological axion states in the magnetic insulator $MnBi_2T_4$ with the quantized magnetoelectric effect. *Phys. Rev. Lett.*, 122:206401, May 2019.

[77] Qianni Jiang, Chong Wang, Paul Malinowski, Zhaoyu Liu, Yue Shi, Zhong Lin, Zaiyao Fei, Tiancheng Song, David Graf, Shalinee Chikara, Xiaodong Xu, Jiaqiang Yan, Di Xiao, and Jiun-Haw Chu. Quantum oscillations in the field-induced ferromagnetic state of $MnBi_{2-x}Sb_xTe_4$. *Phys. Rev. B*, 103:205111, May 2021.

[78] Seng Huat Lee, David Graf, Lujin Min, Yanglin Zhu, Hemian Yi, Samuel Ciocys, Yuanxi Wang, Eun Sang Choi, Rabindra Basnet, Arash Fereidouni, Aaron Wegner, Yi-Fan Zhao, Katrina Verlinde, Jingyang He, Ronald Redwing, V. Gopalan, Hugh O. H. Churchill, Alessandra Lanzara, Nitin Samarth, Cui-Zu Chang, Jin Hu, and Z. Q. Mao. Evidence for a magnetic-field-induced ideal type-ii weyl state in antiferromagnetic topological insulator $Mn(Bi_{1-x}Sb_x)_2Te_4$. *Phys. Rev. X*, 11:031032, Aug 2021.

[79] J. F. Steiner, A. V. Andreev, and D. A. Pesin. Anomalous hall effect in type-I weyl metals. *Phys. Rev. Lett.*, 119:036601, Jul 2017.

[80] Naoto Nagaosa, Jairo Sinova, Shigeki Onoda, A. H. MacDonald, and N. P. Ong. Anomalous hall effect. *Rev. Mod. Phys.*, 82:1539–1592, May 2010.

[81] Jiaheng Li, Chong Wang, Zetao Zhang, Bing-Lin Gu, Wenhui Duan, and Yong Xu. Magnetically controllable topological quantum phase transitions in the antiferromagnetic topological insulator $MnBi_2Te_4$. *Phys. Rev. B*, 100:121103, Sep 2019.

[82] Zhiming Xu, Meng Ye, Jiaheng Li, Wenhui Duan, and Yong Xu. Hydrostatic pressure-induced magnetic and topological phase transitions in the $MnBi_2Te_4$ family of materials. *Phys. Rev. B*, 105:085129, Feb 2022.

[83] Liqin Zhou, Zhiyun Tan, Dayu Yan, Zhong Fang, Youguo Shi, and Hongming Weng. Topological phase transition in the layered magnetic compound $MnSb_2Te_4$: Spin-orbit coupling and interlayer coupling dependence. *Phys. Rev. B*, 102:085114, Aug 2020.

[84] You Lai, Liqin Ke, Jiaqiang Yan, Ross D. McDonald, and Robert J. McQueeney. Defect-driven ferrimagnetism and hidden magnetization in $MnBi_2Te_4$. *Phys. Rev. B*, 103:184429, May 2021.

[85] Cuiying Pei, Yunyouyou Xia, Jiazhen Wu, Yi Zhao, Lingling Gao, Tianping Ying, Bo Gao, Nana Li, Wenge Yang, Dongzhou Zhang, Huiyang Gou, Yulin Chen, Hideo Hosono, Gang Li, and Yanpeng Qi. Pressure-induced topological and structural phase transitions in an antiferromagnetic topological insulator. *Chinese Physics Letters*, 37(6):066401, jun 2020.

[86] K. Y. Chen, B. S. Wang, J.-Q. Yan, D. S. Parker, J.-S. Zhou, Y. Uwatoko, and J.-G. Cheng. Suppression of the antiferromagnetic metallic state in the pressurized $MnBi_2Te_4$ single crystal. *Phys. Rev. Mater.*, 3:094201, Sep 2019.

[87] David Shoenberg. Magnetic oscillations in metals. 1984.

Appendix A

ANALYTICAL FITTING TO THE LIFSHITZ KOSEVICH FORMULA

The multiple frequencies quantum oscillations present in $MnBi_{2-x}Sb_xTe_4$ are difficult to resolve. One reason is because the low oscillations frequency ($< 100T$) and the limited field range (the oscillation can only be seen above the spin-flip transition near 7T.) Another difficulty is that the magnetoresistance background is nontrivial and tends to mix in the strong oscillation signals at a high field.

To overcome these difficulties, we fit the oscillation signal analytically to the Lifshitz Kosevich (LK) formula assuming two frequencies and a polynomial background. The LK formula for the fundamental oscillations (without higher harmonics) of a single sheet of Fermi surface is given by [87]:

$$\frac{\Delta\rho_{xx}}{\rho_{xx}} \propto R_T R_D \times cos[2\pi(\frac{F_s}{B} + \Gamma)] \tag{A.1}$$

where F_s is the frequency of the oscillation, B is the magnetic field, Γ is the phase factor, R_T and R_D are the thermal damping factor and Dingle temperature factor, respectively. The thermal damping factor R_T is determined by temperature T and effective mass m^*.

$$R_T = \frac{\alpha T m^*}{B} / sinh(\frac{\alpha T m^*}{B}) \tag{A.2}$$

At based temp, the thermal damping factor R_T is very close to constant 1. The Dingle temperature factor R_D describes the reduction of the oscillation amplitude caused by electron scattering.

$$R_D = exp(-\alpha T_D m^*/B) \tag{A.3}$$

T_D is the Dingle temperature, given by $\hbar/2\pi k_B \tau_s$. τ_s is the scattering time and α is a constant $2\pi^2 k_B m_e/e\hbar \sim 14.69T/K$. The Dingle temperature factor is determined by both Dingle temperature T_D and effective mass m^*. The higher the dingle temperature, and the

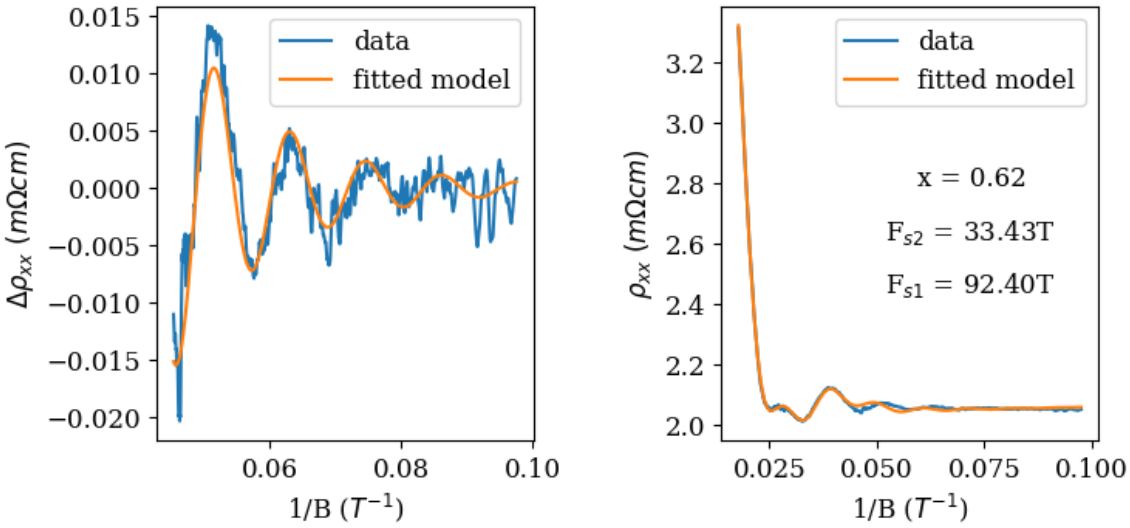

Figure A.1: **Analytical fitting of SdH oscillations to the Lifshitz Kosevich formula** (a) analytical fitting to the single frequency LK formula (Eq. A.1) at low field (< 22T) (b) analytical fitting to the LK formula with two oscillations frequencies and magnetoresistance background (Eq. A.4).

larger the m^*, the faster the oscillation amplitude will damp as a function of 1/B.

In the case of two different sheets of Fermi surfaces coexisting, we have two copies of Eq. A.1, plus a polynomial background. The equation becomes:

$$\rho_{xx} = a \times exp(-\frac{b}{B}) \times cos(\frac{F_{s1}}{B} + \Gamma_1) + c \times exp(-\frac{d}{B}) \times cos(\frac{F_{s2}}{B} + \Gamma_2) + \rho_{xx,bg}(B) \quad \text{(A.4)}$$

where a, b, c, d, F_{s1}, F_{s2}, Γ_1 and Γ_2 are fitting parameters, and $\rho_{xx,bg}(B)$ is the polynomial background. By simultaneously fitting the oscillatory signals and magnetoresistance background, it enables the background to be modulated by the oscillation amplitude when needed, and vice versa.

However, such a fitting has a large parameter space. Therefore, it is important to find a good starting point for each parameter to make the fit converge to the best solution. In the specific case of the quantum oscillations of FM $MnBi_{2-x}Sb_xTe_4$, we find that one oscillation signal associated with a lower frequency always damps faster than the other, which might be the reason that only one frequency of the SdH oscillations was observed under a low magnetic field in chapter 3. Given this knowledge, We subtract a polynomial background

at a low field and fit the major frequency with single-frequency LK formula to obtain the initial parameters. We then conduct a grid search over decades of different F_{s2} and damping factor d to search for the best fit with lowest residual sum of squares.

Fig. A.1(a) shows the analytical fitting to the single-frequency LK formula at low field (< 22 T), while Fig. A.1(b) shows the fitting to the LK formula with two oscillation frequencies and magnetoresistance background. The beating effect and the large turn-up in the oscillatory signals at high magnetic field are well captured by the analytical fit. However, a small deviation from the data was observed in the fitting at a lower magnetic field, which might be related to the anomalous oscillation shift caused by magnetization softening as discussed in section 3.4.1.